POLITECNICO
MILANO 1863

SCUOLA DI INGEGNERIA INDUSTRIALE
E DELL'INFORMAZIONE

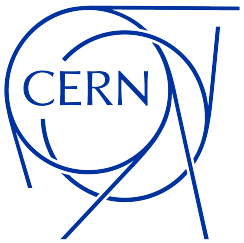

Istituto Nazionale di Fisica Nucleare

Preliminary Mechanical Design of a Superconducting Magnet "Canted-Cosine-Theta (CCT)" for a New Gantry for Hadron Therapy

Tesi di Laurea Magistrale in
Mechanical Engineering - Ingegneria Meccanica

Author: **Gabriele Ceruti**

Student ID: 927893
Advisor: Prof. Marco Giglio
Co-advisors: Lucio Rossi, Diego Perini
Academic Year: 2020-2021

Abstract

Hadron therapy is a medical treatment that uses carbon ions and protons to cure cancer. Carbon ions are really promising for radioresistant tumours, but their use is limited by the size and cost of the necessary infrastructure. An essential element of the infrastructure is the gantry, which significantly improves treatment effectiveness but can weigh hundreds of tons and cost around 25% of the total cost of the facility. A huge contribution to the weight of the gantry is due to the dipole magnets. This thesis reports a complete preliminary mechanical design based on a new superconducting magnet layout, which may drastically reduce the gantry's weight and cost: the Canted-Cosine-Theta (CCT). The thesis starts by explaining why hadron therapy is more effective than traditional treatments, the European collaborations providing the frame of this thesis activity, their scope and why the CCT magnet can help make the gantry cheaper and lighter. The thesis continues by showing the methods that permit an efficient generation of the magnet's geometry by CAD software. The work continues exposing the first mechanical design evaluated, how it was improved and the obtained results. The thesis concludes by explaining how to machine and assemble the magnet and its mechanical structure.

Keywords: Hadron therapy, gantry, superconductivity, CCT magnets, mechanical design, FEM.

Abstract in lingua italiana

L'adroterapia è un trattamento medico che usa ioni carbonio e protoni per curare il tumore. Gli ioni carbonio sono molto promettenti in caso di tumori radioresistenti, ma il loro uso è limitato dalle dimensioni e costo dell'infrastruttura richiesta. Un elemento importante dell'infrastruttura è il gantry che può migliorare molto l'efficacia del trattamento, ma arrivare a pesare centinaia di tonnellate e costare attorno al 25% del costo totale dell'infrastruttura. Molto del peso del gantry è dovuto ai magneti dipolari. Questa tesi descrive un completo studio meccanico preliminare di un nuovo magnete superconduttore volto a rendere il gantry molto più leggero ed economico: il Canted-Cosine-Theta (CCT). La tesi inizia spiegando perché l'adroterapia è più efficacie dei trattamenti tradizionali, i progetti europei in cui è coinvolta la tesi, i loro scopi, perché il magnete CCT può aiutare a ridurre il peso ed il costo del gantry. La tesi prosegue mostrando come creare la geometria del magnete in modo efficacie mediante software CAD. Il lavoro continua illustrando la prima struttura meccanica che circonda il CCT, come è stata migliorata ed i risultati ottenuti. La tesi si conclude spiegando come produrre ed assemblare il magnete CCT con la struttura meccanica che lo circonda.

Parole chiave: Adroterapia, gantry, superconduttività, magneti CCT, progettazione meccanica, FEM.

Acknowledgments

From the bottom of my heart, I would like to thank all my amazing supervisors from INFN – LASA, CERN - MME and PoliMi whose support was fundamental. I will never thank them enough:

Prof. Lucio Rossi believed in me and gave me the unique opportunity to work in the extraordinary world of scientific research. You gave me possibilities that I was dreaming of but I would never have thought of achieving. Moreover, despite your infinite responsibilities, you were always present for me.

Diego Perini was always present for me. Your wisdom, priceless advice and teaching about mechanical engineering were fundamental for my thesis and growing up as an engineer.

Prof. Marco Giglio helped me whenever was necessary and answered all my requests quickly and clearly.

Samuele Mariotto and Ernesto De Matteis supervised my work from the very beginning with patience, introduced me to the world of superconducting magnets, taught me a lot and were always present for my questions.

Stefano Sorti, you joined us late, but your support was priceless as one of all the others. You were always available to give precious advice and help, which were essential for the thesis.

Marco Masci taught me almost everything I know about ANSYS. You were always ready and extremely quick to answer all my questions patiently, help me, and give wise suggestions.

Jorge Guardia Valenzuela supervised me in the most critical moment of the thesis with exceptional patience. You help all of us without hesitating and you are always patient, polite and helpful. I wish you and Marta a very long and happy life together.

Federico Carra who introduced me to CERN, gave really useful advice and answered all my questions clearly and quickly.

Moreover, I would like to thank Prof. Carlo Colombini who has a lot of merit for making me interested in scientific research.

I am very grateful also to God for protecting me over all these years.

Gabriele Ceruti

Contents

1 | Introduction and Motivation

This chapter aims to explain the topics of the thesis and its motivations.

1.1. Hadron Theraphy

'Hadron therapy (often written as "hadron therapy" and also known as "particle therapy" or "ion beam therapy") is a specific type of oncological radiotherapy, which makes use of fast hadrons (non-elementary particles made of quarks and antiquarks) to obtain better dose depositions when compared with the ones of X-rays used in conventional radiotherapy.' [18].

This therapy is based on the Bragg peak phenomenon, which consists in a peak of energy loss (in all three dimensions) of an ion travelling through matter just before it stops [9] (Fig. 1.1). Because of the Bragg peak, which can be very sharp, the energy deposition of hadrons in human tissue is very localized at a penetration depth that depends on the ion energy. Therefore, an ion beam can be tuned to transfer almost all of its energy where the tumour is located, killing tumour cells and minimizing damage to neighbouring healthy tissues (strongly reducing the phenomenon called 'toxicity' [32]). After the pioneering treatment done by the inventor of the cyclotron, E.O. Lawrence in Berkeley, the use of protons in medicine was proposed in a structured way for the first time by Robert R. Wilson in 1946 [36] and executed in 1954 at the Lawrence Berkeley National Laboratory in California (LBNL, US). Nowadays, the only two kinds of hadrons used to cure solid tumours are protons and carbon ions, but other hadrons (e.g. helium ions) have been employed or planned to be employed for tumour treatment [18]. The biological effect of ionizing radiations on cells can be evaluated by the Relative Biological Effectiveness (RBE) which is defined as *'the ratio between the cobalt-60 gamma absorbed dose, which is needed to produce the wanted effect, and the dose of the radiation under study'* [3]. Higher RBE means higher effectiveness of radiation. Protons have an RBE close to X-rays but can reduce side effects a lot due to Bragg peak while carbon ions have a RBE between 3 and 4 times higher than photons, so they are really promising for radioresistant tumours [19].

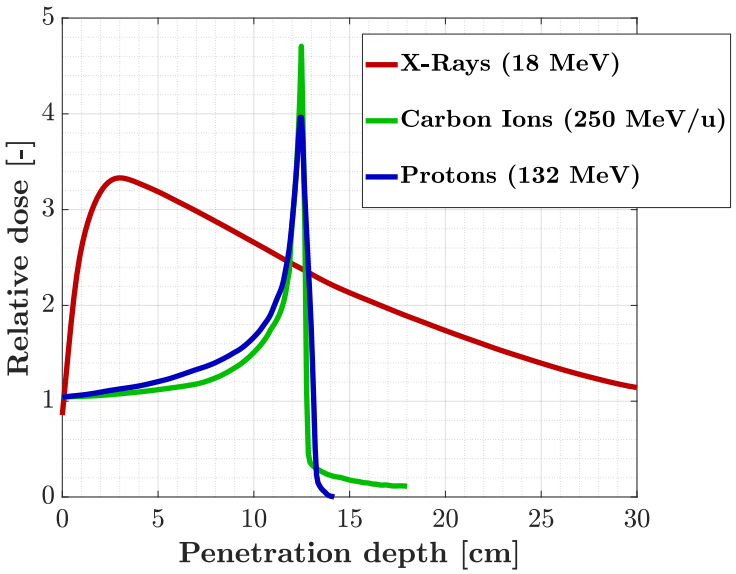

Figure 1.1: Comparison among depth dose profiles of X-rays, protons and carbon ions (Fig. adapted from [32]).

The goal of hadron therapy is not to substitute traditional X-ray radiotherapy (which requires smaller and much cheaper machines), but to provide an alternative treatment for tumours not curable with conventional X-rays [28]. A class of tumour treatment shows higher survival rates or lower recurrences when cured with particle beams. Carbon ions are more effective than protons and for some tumours resistant to X-rays. The use of ions is limited by the size and cost of the needed infrastructure, which is three to four times higher for a therapy centre using both protons and ions than only proton centres (which in turn is probably one order of magnitude higher than a conventional X-ray treatment centre). Only 4 out of 24 particle therapy centres in Europe employ carbon ions currently, while all the other centres only use protons. In the world, just 12 out 105 particle centres use ions. Moreover, a typical particle centre consists of a particle accelerator which gives the required energy to hadrons and provides particles to more treatment rooms. One of the rooms might comprise a gantry (Fig. 1.2) which is the system that enables multiple directions of beam delivering [9]. This improves the treatment effectiveness significantly, since it allows to spare the nearby healthy tissues. Almost all proton centres are equipped with a gantry, but just few ion centres have this system since it can weigh many hundreds tons and it costs around 25% of the total cost of the facility [9]. The first gantry built in Europe is at HIT (Heidelberg Ion Therapy centre) and uses normal conductive (resistive) magnets, has a length of 26 m, a weight of 600 tons and started working in 2012. For this reason, it is necessary to make the gantry lighter and cheaper to allow a wide diffusion of ion gantries. In this context, numerous European Institutes are working in several collaborations and this thesis is involved in two of these collaborations: HITRI*plus* and IFAST [28].

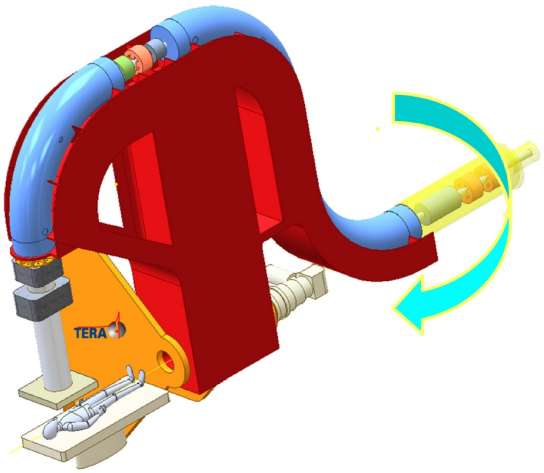

Figure 1.2: Drawing of compact ion gantry with three Canted-Cosine-Theta magnets (blue). Fig. from [28].

1.2. HITRI*plus*

The Heavy Ion Therapy Research Integration plus (HITRI*plus*) groups 22 Institutes coordinated by CNAO (the National Centre for Oncological Hadron Therapy in Pavia, Italy). Among the objectives of the collaboration, there is improving the position of Europe in cancer treatment with ion beams ranging from helium to carbon and heavier ions. To achieve this goal, it is necessary to design new technologies to improve the accelerators and their auxiliary systems that provide particle beams for clinical therapy. These technologies will improve the existing infrastructures and will be the foundation for the new generation of European design for hadron therapy facilities. For this reason, the HITRI*plus* collaboration comprises a work package (WP) dedicated to superconducting magnets: WP8 – Superconducting Magnet Design. Hadrons need to be guided inside the accelerator and then towards the patient. Since hadrons are charged particles, their guiding and focusing are performed through a magnetic field. Therefore, magnets are essential inside treatment facilities. The term 'Superconducting' refers to the material used for the conductor cable whose resistivity is null under certain conditions of temperature (close to 0 K), magnetic field and current density. In a 3D reference system, these three parameters determine the critical surface below which the conductor is in its superconducting state. The main goal of WP8 is exploring new, solid, effective and cheaper magnet design for a novel and light rotatable gantry. The WP8 is constituted by seven research Institutes and one SME (Small Medium Enterprise):

- INFN – Istituto Nazionale di Fisica Nucleare (sections of Genova and Milano - LASA, It).
- CEA - Commissariat à l'Énergie Atomique et aux Énergies Alternatives (Saclay, Fr).
- CERN – European Organization for Nuclear Research (Geneva, Ch).
- CIEMAT - Centro de Investigaciones Energéticas, Medioambientales y Tecnológicas (Madrid, Es).
- PSI - Paul Scherrer Institute (Villigen, Ch).

- Uppsala University-Freia laboratory (Uppsala, Se).
- Wigner Research Centre for Physics (Budapest, Hu).
- Sentronis, a Serbian company associated via SEEIIST (South East European International Institute for Sustainable Technologies).

Specifically, this thesis was carried out with INFN – LASA (Laboratori Acceleratori e Superconduttività Applicata) and the CERN's group MME (Mechanical and Materials Engineering).

1.2.1. Objectives of HITRI*plus* - WP8

The main goal of HITRI*plus* WP8 is performing a wide examination of the possible solutions for the gantry and synchrotron, evaluating the use of different superconductor types and magnet designs. Furthermore, the collaboration must project, produce and test one magnet demonstrator. Different superconductors will be studied: MgB_2, Low Temperature Superconductors (LTS) such as Nb-Ti and Nb_3Ti, High Temperature Superconductors (HTS) such as REBCO (Rare Earth Barium Copper Oxide) and Bi-2212 ($Bi_2Sr_2CaCu_2O_8$). Moreover, the following coil layouts will be evaluated: Cosine-Theta (CT), Canted-Cosine-Theta (CCT) or racetrack (RT). The collaboration has chosen as a temporary baseline the use of niobium-titanium (Nb-Ti) superconductor wound as CCT, conduction cooled and impregnated coils.
The main features of the demonstrators are central field B_0 between 4 and 5 T and free aperture (where the particle beam travels) ranging from 60 mm to 90 mm. The demonstrator will have a length of about 500 mm of uniform field and proper field quality (FQ) for accelerators (Appendix A explains the meaning of field quality). The most difficult task is designing a curved magnet with really small bending radius, imposed by the energy (430 MeV/nucleon) of the carbon ions which requires a beam rigidity (the product between magnetic field B and bending radius ρ) of $B\rho$ = 6.6 Tm. Thus, the bending radius varies from 1.3 m to 1.6 m depending on the selected field level. The WP8 program is organized into 5 tasks. This thesis is mainly involved in Task 8.2 whose goal is performing a comparative study among different designs and types of superconductors and coil layouts. This work will assess the initial choice of Nb-Ti and CCT for the parameters chosen inside the collaboration: B_0 = 4.5 T (pure dipolar field) at 80% of the critical surface on the load line, aperture of 75 mm, magnetic length of 800 mm and operative temperature of about 5 K, 10 K and 20 K.

1.3. IFAST

IFAST (Innovation Fostering in Accelerator Science and Technology) is a wide collaboration grouping 48 members. As HITRI*plus*, IFAST contains a work package on magnets: WP8 - Innovative Superconducting Magnets (the same WP number as HITRI*plus* is a coincidence). The WP8 was proposed by the same members as HITRI*plus* WP8 and aims at studying straight CCT magnet design in HTS (High Temperature Superconductors) with industry for particle accelerators and for hadron therapy. There are similarities with HITRI*plus* WP8 objectives, such as the magnet size and field magnitude, but IFAST focuses on HTS. HTS have great potential to become the workhorse for magnets for hadron therapy gantry and synchrotron. The critical temperature (the temperature above which the conductor loses the superconducting

state) is much higher for HTS than for classical superconductors like Nb-Ti. This characteristic translates into much larger stability margins. Nevertheless, the HTS technology is not ready yet to be engineered in an operating magnet to be successfully integrated into a gantry or a synchrotron in the next years. Therefore, IFAST-WP8 aims at developing and proving the HTS CCT technology to enable a design of a full HTS system. The collaboration of WP8 counts on eight academic Institutes and three companies:

- INFN (divisions of Genova and Milano-LASA, It).
- CEA (Saclay, Fr).
- CERN, (Geneva, Ch, international organization).
- CIEMAT (Madrid, Es).
- PSI (Villigen, Ch).
- University of Geneva.
- Uppsala University-Freia laboratory (Uppsala, Se).
- Wigner Research Centre for Physics (Budapest, Hu).
- BNG - Bilfinger Noell Gmbh (Wurzburg, De).
- Elytt Energy SL (Artea, Es).
- Scanditronix Magnet AG (Vislanda, Se)

1.3.1. Objectives of IFAST - WP8

As said before, the main goal of WP8 is developing HTS technology with CCT straight layout. The final objective is to manufacture an HTS CCT demonstrator of about 4-5 T. Before making the final demonstrator, a simpler combined function magnet in Low Temperature Superconductor (Nb-Ti) will be manufactured to learn. Combined function means that the coils provide a quadrupole component superimposed to the main dipolar field (Appendix A explains the meaning of combined function magnet and magnetic field harmonics). This straight combined function magnet will have a main dipolar field of 4-5 T and a gradient (for quadrupolar field) of 5-10 T/m. This thesis in mainly involved in the Task 8.2 of the collaboration, which studies the preliminary engineering design of the first combined function demonstrator in Nb-Ti.

1.4. Conductor and Magnet Design

The conductor selected for HITRI*plus* and IFAST demonstrators is Nb-Ti. Two preliminary designs of the conductor will be evaluated (Fig. 1.3):

- A "high current" solution where the conductor is made by two insulated rectangular Rutherford cables, each made by 40 wires. If cables are connected in series it is possible to have a high field limiting the current to about 12.3 kA.
- A "low current" version, where the conductor is made by twenty round ropes of classical

6+1 (Fig. 1.3) topology. Ropes are insulated and connected in series to keep current low. This reduces current to 1.5 kA per rope, but it requires many electrical joints to be integrated into the design.

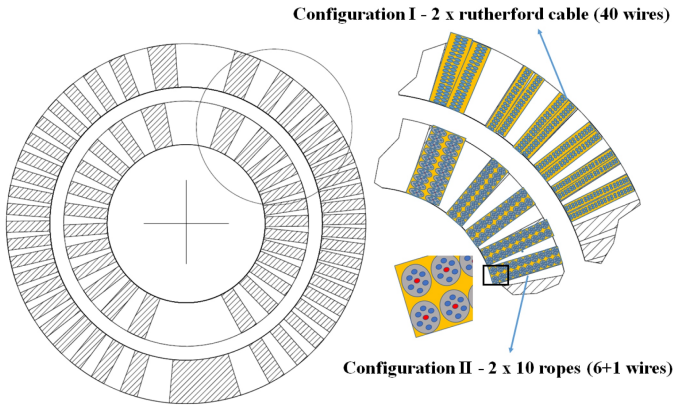

Figure 1.3: Cross-section of the conductor for a CCT combined function magnet with a depiction of the two preliminary conductor designs. In each rope, it is possible to see 6 superconducting wires (blue circle) and the single resistive wire (red). Fig. from [28].

1.5. CCT Magnet

As mentioned before, the rotating beamline called gantry is extremely important for treating the patient, and it is necessary to make this system lighter and cheaper. In traditional design, a huge part of the weight is due to the last bending dipoles magnet, which have challenging requirements: being curved over a wide angle, having huge aperture, producing combined function fields and changing field rapidly according to the beam energy. Moreover, the design and winding of the coil are more difficult due to the strongly curved shape. In the end, the large aperture and bending angle increase Lorentz forces which can deform the magnet and affect the field quality [9]. The CCT design matches these requirements, so it is under investigation in the HITRI*plus* and IFAST collaborations. Furthermore, the superconducting technology can give two relevant advantages to a gantry magnet system. The weight can be drastically reduced since the magnetic field generated by superconducting magnets is coil-dominated, so that iron can be considered just for magnetic shielding. Compared to resistive magnets (which use a big iron yoke for field generation), superconducting gantry magnets can be up to an order of magnitude lighter. The other advantage consists in the ability to generate much higher fields, opening the chance for novel and better beam optics solutions [9]. The superconducting technology allowed the HIMAC (Heavy Ion Medical Accelerator in Chiba, Japan) to decrease the size and weight of the gantry by about a factor of 2 with respect to the HIT gantry. A new gantry design based on fixed aperture magnets and a new concept of mechanics [4] have the potential of reducing the weight by a factor from 3 to 5 with respect to the HIMAC gantry. At the same time, a Cos-Theta magnet design is being considered in CERN-CNAO-INFN-MedAustron collaboration [29]. If the program HITRI*plus* and IFAST are successful, CCT could constitute a simpler and cheaper alternative to the more consolidated Cos-Theta magnet design. This thesis aims to perform a preliminary mechanical design of both straight and curved CCT.

The concept of Canted-Cosine-Theta (CCT) magnet was proposed for the first time in 1970 [23]. The terms Cosine-Theta refer to the current component normal to the cross-section of the magnet that follows the function $\cos(n\theta)$: it is maximum for $\theta = 0$, equal to 0 for $\theta = \pi/(2n)$, maximum but with opposite sign for $\theta = \pi/n$ and again equal to 0 for $\theta = 3\pi/(2n)$. The word canted refers to the inclination of the conductors (Fig. 1.4).
The CCT design is based on pairs of conductor layers (Fig. 1.4 and Fig. 1.5) wound around mandrels (also called formers) nested one inside the other. Current flows in the two conductor layers so that, when the magnet is powered, the transverse magnetic field components (vertical lines in Fig. 1.6) sum and axial field components (horizontal lines in Fig. 1.6) cancel each other.

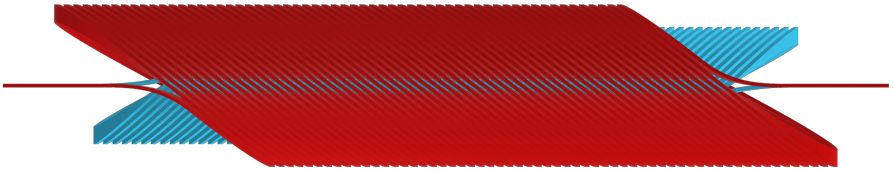

Figure 1.4: Side view of the CCT's conductor layers. The blue part is the conductor of the inner layer, while the red part is the conductor of the external layer.

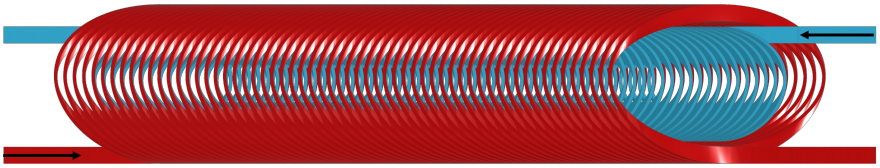

Figure 1.5: Top view of the CCT's conductor layers. The black arrows indicate the current.

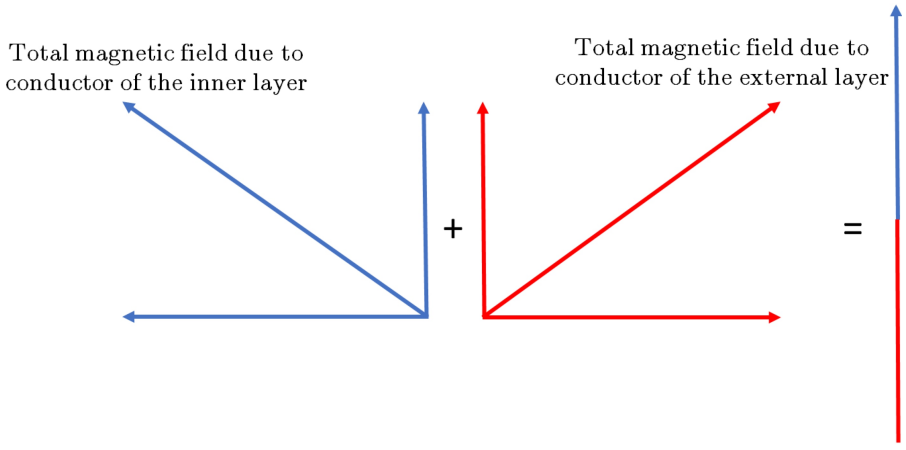

Figure 1.6: Sum of the magnetic fields generated by two conductor layers.

The former is a hollow cylinder (or toroid in case of curved CCT) that contains a groove, obtained by machining, where the conductor is placed. Ribs and spar characterize the former: ribs are thin walls between two consecutive turns of the groove, while the spar is a thick wall between the hollow of the cylinder and the ribs (Fig. 1.7, 1.8, 1.9 and 1.10).

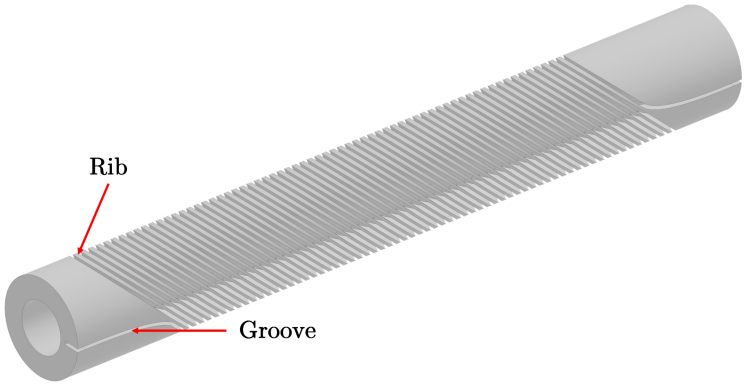

Figure 1.7: Picture of a straight CCT former. The groove (obtained by machining) generates the ribs and spar. The cross-section of the groove is rectangular.

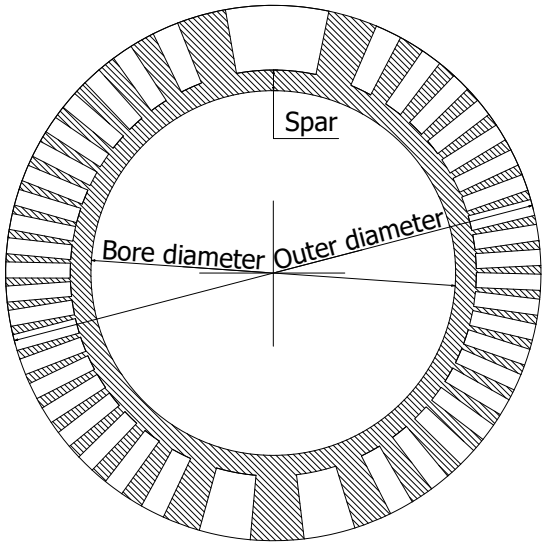

Figure 1.8: Cross-section and some parameters of a single former (pure dipole case).

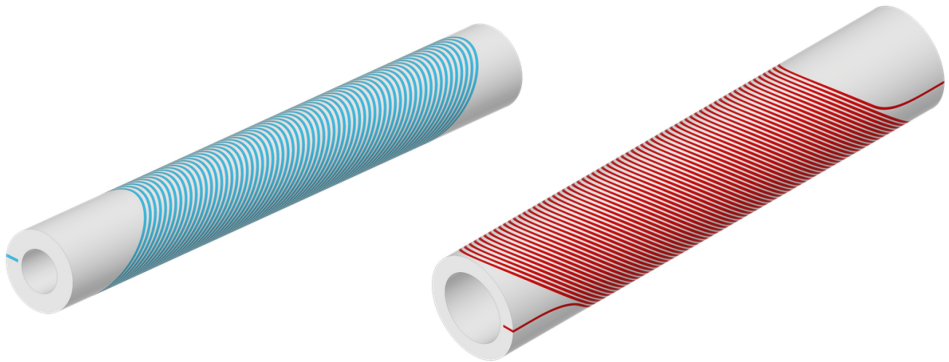

Figure 1.9: Assembly of the single conductor layers with their formers.

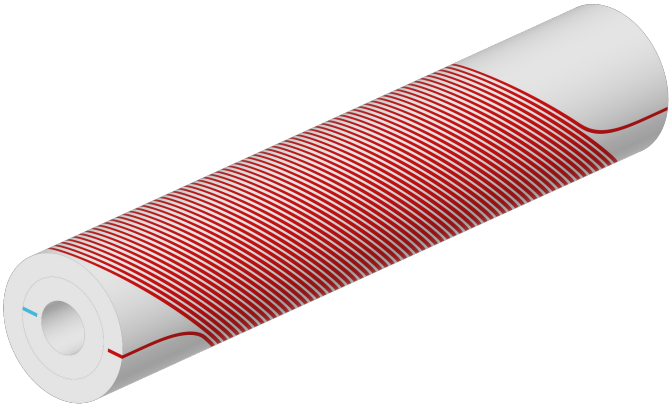

Figure 1.10: Assembly of the two layers which gives the final CCT magnet.

The coil of the magnet experiences Lorentz force density $\vec{f} = \vec{j} \times \vec{B}$ whose main effect in dipole magnets (one of the cases of this thesis) is compressing the coil from the pole down towards the midplane (Fig. 1.11):

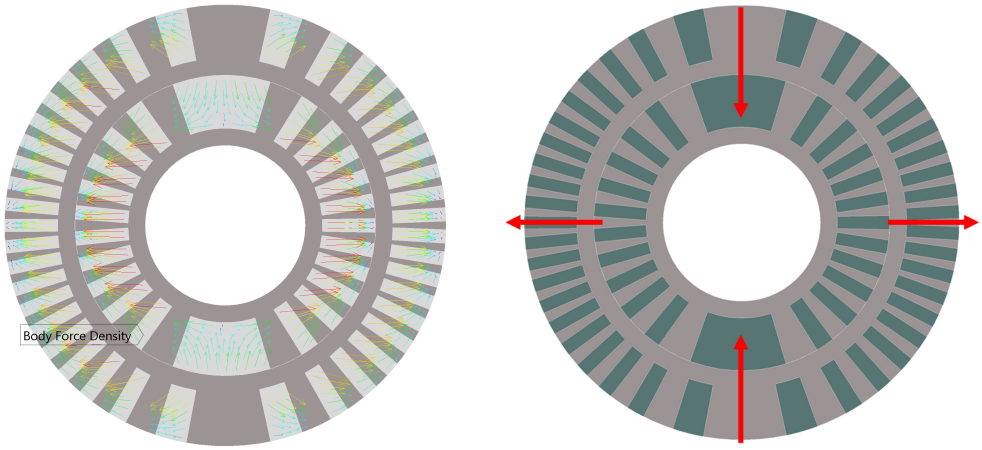

Figure 1.11: Lorentz forces (a) and their resultants (b) indicated by the red arrows.

In this way, an ovalization of the former (race track deformation) is induced, affecting the field quality. Moreover, Lorentz forces can make the conductor move causing friction, cracking and energy release, which can increase the temperature above the critical temperature (where the coils lose their superconducting state). For all these reasons, Lorentz forces must be counteracted. Traditional superconducting magnets (Fig. 1.12a) use an external structure to compress (pre-stress) the conductor during the magnet assembly. If the applied pre-stress is large enough, the Lorentz forces are taken up by the pre-stress preventing the conductor movement when the magnet is energized. Pre-stress is applied employing large presses and a system of austenitic steel collars (Fig. 1.12a). In the CCT layout ribs between individual conductors provide structural support at the single conductor turn level (Fig. 1.12b), intercepting the Lorentz forces and transferring them to the mandrel preventing the accumulation of forces themselves. So, the need for pre-stress is minimal and only for radial containment. Moreover, this can reduce the peak

of stresses in the conductor up to an order of magnitude with respect to traditional Cos-Theta magnet design [9] (Fig. 1.12a).

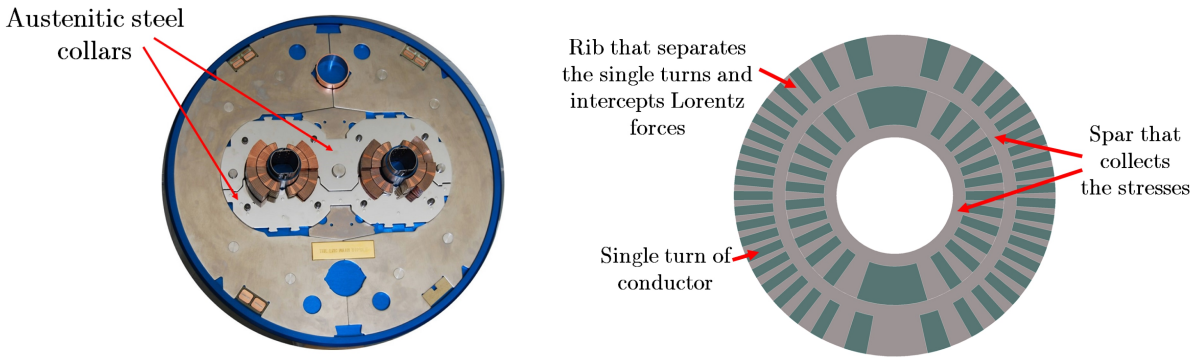

Figure 1.12: Lorentz forces support in case of traditional Cos-Theta design (a) and CCT (b). Courtesy of Lucio Rossi.

The value of the main design parameters decided for the straight CCT are in Table 1.1:

Parameter	Ropes configuration	Rutherford configuration
Bore diameter inner former	75 mm	75 mm
Spar	8 mm	8 mm
Groove height	25 mm	20 mm
Groove width	5 mm	4 mm
Outer diameter external layer	207 mm	187 mm
Minimun ribs thickness	1.25 mm	1.25 mm
Axial pitch	12.5 mm	10.5 mm
Number of turns	66	78
Central magnetic field	4.5 T	4.5 T
Gradient for quadrupolar field	5 T/m	5 T/m
Current per cable	1.536 kA	12.3 kA
Groove current	30,720 A	24,960 A

Table 1.1: Main straight CCT design parameters.

The parameters of the curved CCT (1.5 m of bending radius) are the same as straight CCT except for the magnetic field (the gradient is null since only the dipolar field is present) and the pitch, which is equal to 0.00895 rad. A detailed explanation of the straight and curved CCT geometry is in Chapter 2.

1.6. Introduction to CERN

1.6.1. History

The *Conseil Européen pour la Recherche Nucléaire* (CERN) was established in 1954 thank to the agreement among 12 founding Member States: Belgium, Denmark, France, the Federal Republic of Germany, Greece, Italy, the Netherlands, Norway, Sweden, Switzerland, the United Kingdom and Yugoslavia.

Figure 1.13: First CERN's Council Session in 1955 (Photo credits: CERN).

Since then, CERN has given a masterful contribute to scientific research by its discoveries and developing new technologies. It is worth remembering the discovery of particles W and Z in 1983, that brought the CERN first Nobel Prize in 1984 [15], and the Higgs boson in 2012 which gave the Nobel Prize to Peter Higgs in 2013.
Today CERN is constituted by 23 Member States and collaborates with "Observer states", institutes, universities and non-member states from all over the world. Moreover, the lab groups thousands of people worldwide, thus favouring cooperation between nations, universities, and scientists [21]. In 2020 about 17,000 people [13] (not just scientists) worked at CERN, including students, trainees, physicists, engineers, technicians, administrative and lawyers, including 13,000 users.

1.6.2. Research at CERN

Physics research at CERN aims at investigating the ultimate structure of matter. To achieve this goal, CERN uses the biggest particle accelerator in the world: the Large Hadron Collider (LHC), which can be considered as an extremely powerful microscope that gives details at the scale length of $\lambda = h/p$ (p is the particle momentum and h is the Planck's constant). LHC can accelerate particles up to the energy of ∼10 TeV, so it allows to explore the matter with detail of $\sim 10^{-19}$ m. The accelerated particles collide among them, and their kinetic energy is transformed into very massive particles which were only present up to a few picoseconds after the Big Bang. So, accelerators allow us to explore our origin by permitting us to see into the infinitely small and taking us back in time just some instants after the Big Bang [26]. Particles (protons in case of LHC) are extracted from hydrogen gas molecules ionized and accelerated gradually by all the particle accelerators built in the history of CERN: LINAC4, BOOSTER, PS, SPS and LHC (Fig. 1.14).

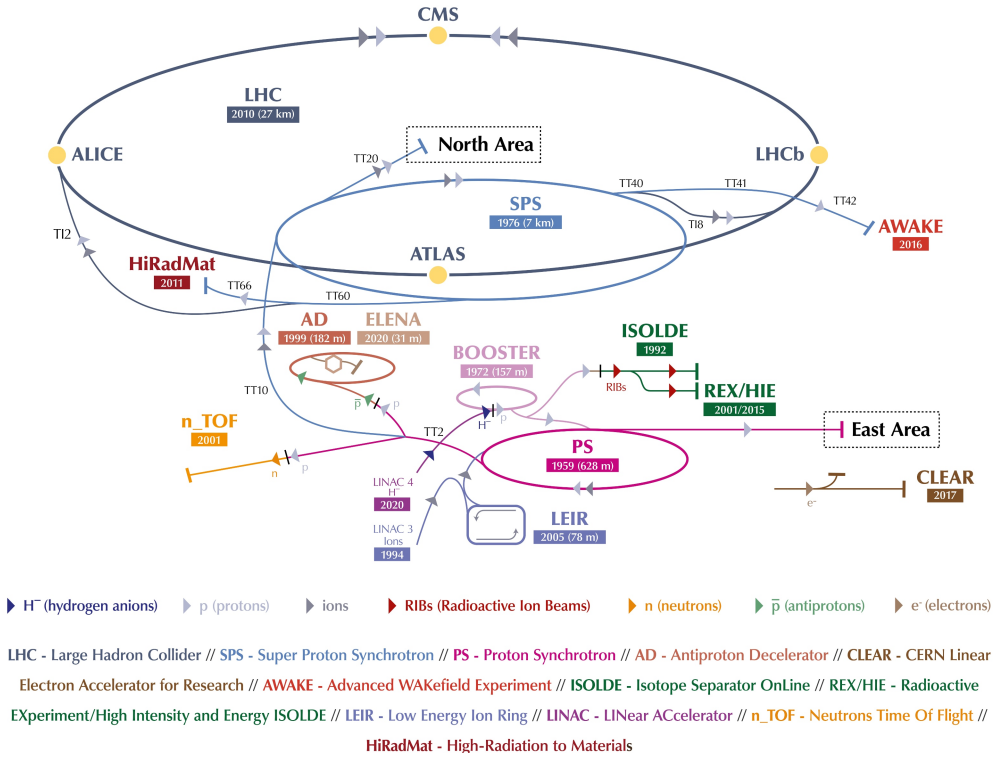

Figure 1.14: The CERN's accelerator complex (Photo credits: CERN).

Since the particles are charged, they are accelerated using resonant radio-frequency (RF) cavities (Fig. 1.15a), which could be placed straight. However, accelerating protons up to the necessary energy would require a too long line of RF cavities. For this reason, all the accelerators mentioned before (except for LINAC 4) are circular because this allows particles to pass many times through RF cavities and gain energy at each passage. Moreover, magnets are required to guide the trajectory of the proton beam. Most of the LHC ring is filled with superconducting dipole magnets (Fig. 1.15b), which can achieve magnetic fields of 8.3 T to bend the trajectory of the beam travelling at almost the speed of light (protons travel the 27 km length of LHC more than 10,000 times per second) [21].

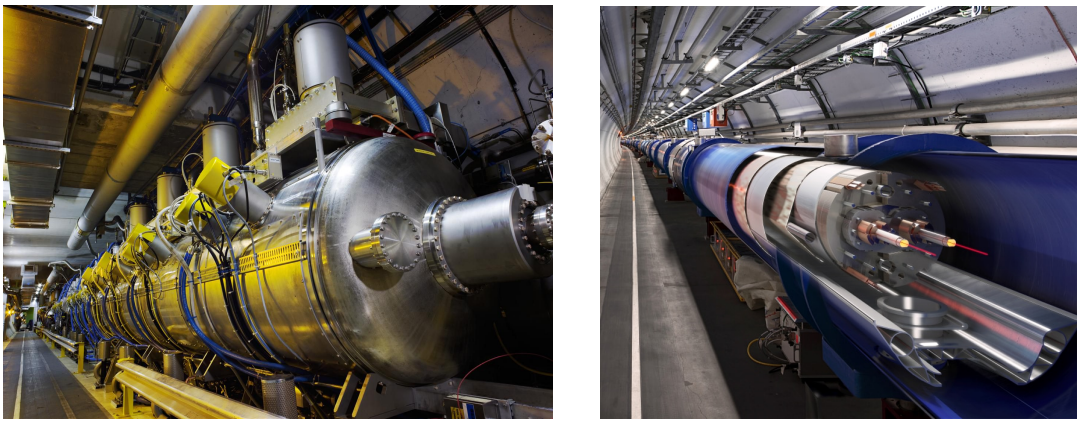

(a) (b)

Figure 1.15: RF cavities (a) and 3D section of the LHC dipole in the tunnel (b) (Photo credits: CERN).

There are not just dipoles in LHC. Quadrupole magnets are required to focus and avoid excessive beam size increase, while higher order magnets (such as sextupoles, octupoles and decapoles) are needed for beam stability and to correct field errors in the main magnets. It is worth noticing that LHC counts 1600 main magnets (dipoles and arc quadrupoles) and about 8000 superconducting magnets required for correction and beam control. The main magnets fill 2/3 of the ring and generate about 80% of the cost of the magnet system, which is about half of the cost of the entire LHC Project [26].
CERN shares the knowledge generated for particle physics with society. HITRI*plus* and IFAST are just two examples of this sharing. In fact, research done at CERN can be applied to many different fields: medical technologies, aerospace, safety, environment, industry 4.0, cultural heritage, safety and emerging technologies (more details can be found in Appendix B).

1.7. Take Home Message

This chapter explained the advantages of hadron therapy, the difficulties of favouring its wide diffusion and why the CCT magnet can help.

2 | CAD Modelling

This chapter describes the geometry of the CCT magnets and how to generate it by CAD software in a parametric way.

The first step of the thesis was generating the geometry of the CCT since it is necessary to carry out Finite Element Method (FEM) simulations. The geometry was developed using the CAD (Computer-Aided Design) software Autodesk Inventor since it allows easy generation of a parametric model. This chapter shows the equations of the curves involved, the model's main steps, and how it was possible to obtain an utterly parametric model that updates automatically.

2.1. Winding Path of Straight CCT Magnet

In the case of a straight CCT, the path of the grooves (winding path) obtained by machining lies on a cylindrical surface. In general, the path can be described in cylindrical coordinates (Fig. 2.1) as follows [9]:

$$\vec{p}(\theta) = R\hat{r} + p_z(\theta)\,\hat{z} \tag{2.1}$$

where R is the radius of the cylindrical surface, θ is the azimuthal (circumferential) angle and $p_z(\theta)$ is a function that describes the axial development of the path along the z-axis. Moreover, for the next steps, it is necessary to define the local reference system of $\vec{p}(\theta)$: $\hat{t}$ is the versor tangent to the path, $\hat{r} = (1,\ 0,\ 0)$ is the versor normal to the cylindrical surface pointing outward and $\hat{b}$ is the binormal versor (Fig. 2.2). The vectors $\vec{t}$ and $\vec{b}$ are expressed in the following way:

$$\vec{t} = \frac{d\vec{p}(\theta)}{d\theta} = R\hat{\theta} + p_z'(\theta)\,\hat{z} \tag{2.2}$$

$$\vec{b} = \vec{t} \times \hat{r} = \ p_z'(\theta)\,\hat{\theta} - R\hat{z} \tag{2.3}$$

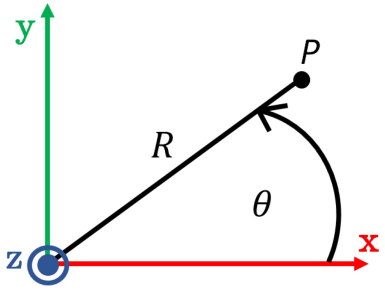

Figure 2.1: Cylindrical reference system.

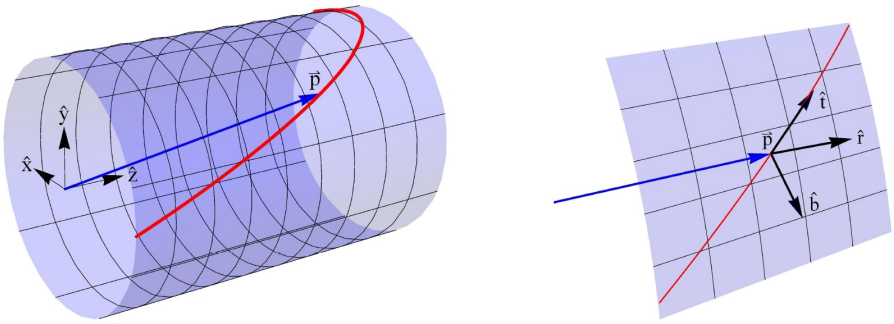

Figure 2.2: Beginning of the winding path and local reference system at a generic point of the path (Fig. from [9]). Courtesy of Lucas Nathan Brouwer.

To generate a uniform magnetic field region far from the extremities of the magnet, the winding path must be axially periodic. For this reason, the following condition is imposed:

$$|p_z(\theta + 2\pi) - p_z(\theta)| = w \tag{2.4}$$

Where w is the pitch: the constant axial distance between consecutive turns (Fig. 2.3).

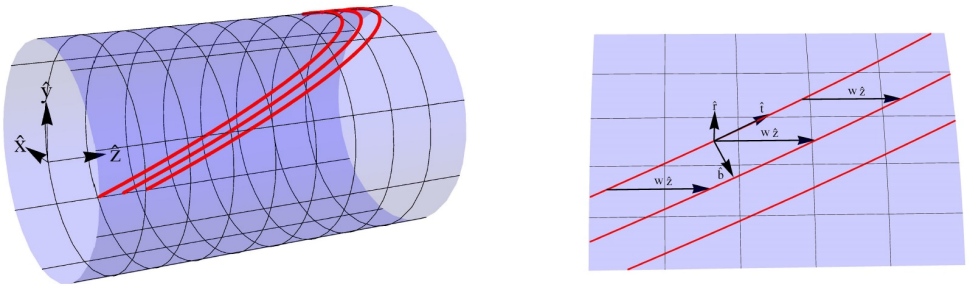

Figure 2.3: Periodic winding path and axial pitch w (Fig. from [9]). Courtesy of Lucas Nathan Brouwer.

The pitch must be higher than a minimum value defined by the groove width and minimum ribs thickness (which is usually on the midplane of magnet that is XZ in this description) as shown in Fig. 2.4:

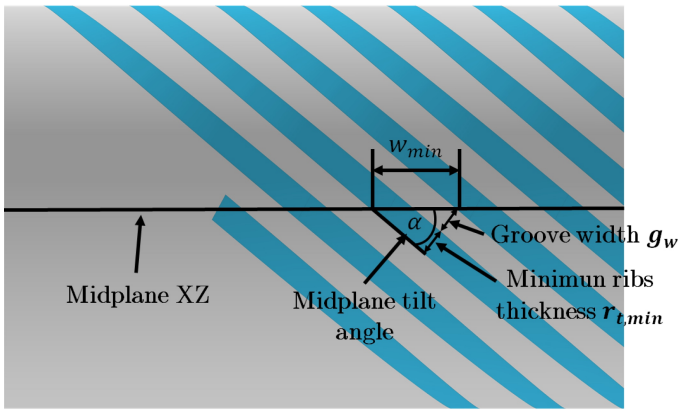

Figure 2.4: Definition of the minimum value of axial pitch w_{min}.

Under the hypothesis $R \gg w$, which allows approximating the cylindrical surface as planar close to the midplane, it is possible to define w_{min} (Fig. 2.4):

$$w_{min} = \frac{g_w + r_{t,min}}{\sin(\alpha)} \tag{2.5}$$

The thickness of the ribs is not constant. In the case of a single harmonic (see Appendix A for magnetic field harmonics explanation), the thickness is minimum on the midplane XZ and maximum for $\theta = \pi/(2n)$.
Furthermore, the perpendicular distance between consecutive turns $\delta(\theta)$ (in the direction of $\vec{b}$) can be approximated by (Fig. 2.3):

$$\delta(\theta) = w\hat{z} \cdot \hat{b} = w(0,0,1) \cdot \frac{(0, p'_z(\theta), -R)}{\sqrt{[p'_z(\theta)]^2 + R^2}} = \frac{wR}{|\vec{t}|} \tag{2.6}$$

Since $\delta(\theta)$ is a distance, the negative sign of $-wR$ is neglected.
$\vec{p}(\theta)$ describes a continuous current line of magnitude I_0, so $\delta(\theta)$ can be used to average the line currents into a 2D cylindrical current sheet with current density [9]:

$$\vec{j}(\theta) = \frac{I_0 \hat{t}}{\delta(\theta)} = I_0 \frac{\vec{t}}{|\vec{t}|} \frac{|\vec{t}|}{wR} = \frac{I_0}{wR}\vec{t} = \frac{I_0}{w}\left(\hat{\theta} + \frac{p'_z(\theta)}{R}\hat{z}\right) \tag{2.7}$$

The averaged current density is made by two components: a constant azimuthal component dependent on w and an axial component that varies with θ. The azimuthal component generates the solenoidal field while the axial component generates the transverse magnetic field dependent on $p'_z(\theta)$. Eq. 2.7 can be used to determine the expression of $p'_z(\theta)$. In the case of a cylindrical sheet with axial current $j_z(\theta) = j_{0nz}\cos(n\theta)$ at a fixed radius, it is possible to produce a pure n-th order magnetic field harmonic within the aperture [35] (see Appendix A for the magnetic field harmonic explanation). To generate the desired field harmonic in a CCT, the axial component of $\vec{j}(\theta)$ must be equal to the ideal $\cos(n\theta)$ current density distribution:

$$\frac{I_0}{wR} p'_z(\theta) = j_{0nz}\cos(n\theta) \tag{2.8}$$

So, $p_z(\theta)$ can be obtained integrating the previous expression:

$$p_z(\theta) = \int \frac{wR}{I_0} j_{0nz}\cos(n\theta)d\theta = \frac{wR}{I_0}\frac{j_{0nz}}{n}\sin(n\theta) \tag{2.9}$$

Now, the equation of the winding path (Eq. 2.1) can be written as:

$$\vec{p}(\theta) = R\hat{r} + \frac{wR}{I_0}\frac{j_{0nz}}{n}\sin(n\theta)\hat{z} \tag{2.10}$$

Eq. 2.10 describes a tilted $\sin(n\theta)$ function that lays on the cylindrical surface. To make the path advance along the longitudinal direction with a pitch equal to w, it is necessary to add $p_z(\theta)$ the term $\frac{w}{2\pi}\theta$:

$$p_z(\theta) = \frac{wR}{I_0}\frac{j_{0nz}}{n}\sin(n\theta) + \frac{w}{2\pi}\theta \tag{2.11}$$

So, Eq. 2.10 becomes:

$$\vec{p}(\theta) = R\hat{r} + \left[\frac{wR}{I_0}\frac{j_{0nz}}{n}\sin(n\theta) + \frac{w}{2\pi}\theta\right]\hat{z} \tag{2.12}$$

Where $0 \leq \theta \leq 2\pi n_t$ and n_t represents the number of turns.
Three parameters define a CCT layer with a fixed radius: I_0, j_{0nz} and w. These parameters can be related to the geometrical dimensions of the path defining a midplane tilt angle α (see Fig. 2.5):

$$\tan(\alpha) \equiv \left.\frac{\vec{t}\cdot\hat{\theta}}{\vec{t}\cdot\hat{z}}\right|_{\theta=0} = \frac{R}{\frac{wR}{I_0}j_{0nz}} = \frac{I_0}{wj_{0nz}} \tag{2.13}$$

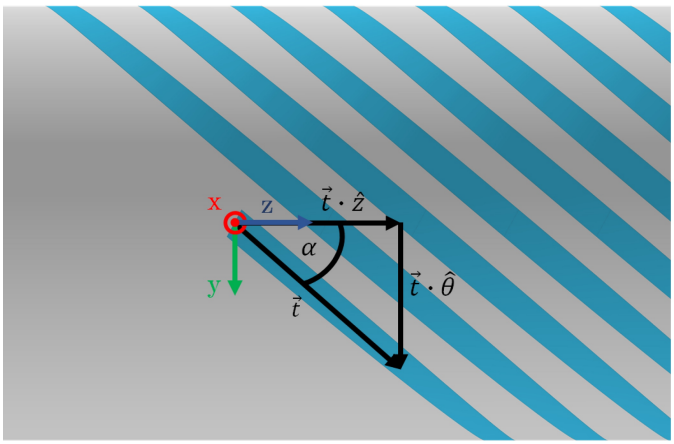

Figure 2.5: Definition of the midplane tilt angle α.

The previous relationship is valid under the assumption $R \gg w$ which allows approximating the cylindrical surface as planar close to the position $\theta = 0$. So, the winding path can be written in terms of the two free geometrical parameters α and w:

$$\vec{p}(\theta) = R\hat{r} + \left[\frac{R}{n\tan(\alpha)}\sin(n\theta) + \frac{w}{2\pi}\theta\right]\hat{z} \tag{2.14}$$

If the magnetic field is a pure dipole ($n = 1$) the winding path is given by:

$$\vec{p}(\theta) = R\hat{r} + \left[\frac{R}{\tan(\alpha)}\sin(\theta) + \frac{w}{2\pi}\theta\right]\hat{z} \tag{2.15}$$

If the magnetic field is a pure quadrupole ($n = 2$):

$$\vec{p}(\theta) = R\hat{r} + \left[\frac{R}{2\tan(\alpha)}\sin(2\theta) + \frac{w}{2\pi}\theta\right]\hat{z} \tag{2.16}$$

In the case of more field harmonics (combined function), it is sufficient to sum the terms related to the different harmonics. In case of the presence of both dipolar and quadrupolar fields:

$$\vec{p}(\theta) = R\hat{r} + \left[\frac{R}{\tan(\alpha_1)}\sin(\theta) + \frac{R}{2\tan(\alpha_2)}\sin(2\theta) + \frac{w}{2\pi}\theta\right]\hat{z} \tag{2.17}$$

If dipolar, quadrupolar and sextupolar fields are present:

$$\vec{p}(\theta) = R\hat{r} + \left[\frac{R}{\tan(\alpha_1)}\sin(\theta) + \frac{R}{2\tan(\alpha_2)}\sin(2\theta) + \frac{R}{3\tan(\alpha_3)}\sin(3\theta) + \frac{w}{2\pi}\theta\right]\hat{z} \tag{2.18}$$

In the combined function magnet, the physical meaning of the midplane tilt angle (Fig. 2.5) is still valid for the single harmonic components, but since they sum the overall result loses the geometrical meaning of the midplane tilt angle.
Moreover, it is possible to add a contribution to Eq. 2.14, which allows centring the path with respect to the XY plane, and the winding path equation becomes:

$$\vec{p}(\theta) = R\hat{r} + \left[\frac{R}{n\tan(\alpha)}\sin(n\theta) + \frac{w}{2\pi}\theta - \frac{n_t w}{2}\right]\hat{z} \tag{2.19}$$

The previous equation can be written in case of the presence of several magnetic field harmonics:

$$\vec{p}(\theta) = R\hat{r} + \left[\frac{w}{2\pi}\theta - \frac{n_t w}{2} + \sum_{n=1} a_n \sin(n\theta)\right]\hat{z} \tag{2.20}$$

Where $a_n = \frac{R}{n\tan(a_n)}$. The expression of a_n can be related to the magnetic field obtained for the case of a single current sheet [9]. Considering a real superconducting cable with finite transverse dimensions, electromagnetic simulations must be carried out to evaluate the values of the coefficients a_n that generate the desired magnetic field quality (see Appendix A for the explanation of magnetic field quality). For the cases of the thesis, the following values for a_n were obtained (Table 2.1):

Coefficient	Ropes Configuration	Rutherford Configuration
a_1	78.808 mm	78.808 mm
a_2	3.821 mm	3.661 mm

Table 2.1: Coefficients for combined function straight CCT.

2.2. Winding Path of Curved CCT

The winding path of the curved CCT can be determined in the same way as in the straight configuration using a cylindrical coordinate system (Fig. 2.6), but this time the path will lie on a toroidal surface. The winding path can be expressed in cylindrical coordinates as follows:

$$\vec{p}(\theta) = [\rho - R\cos(\theta)]\hat{r} + p_\phi(\theta)\hat{\phi} + [R\sin(\theta)]\hat{z} \tag{2.21}$$

Where R is the radius of the cross-section section of the toroid, θ is the azimuthal (circumferential) angle, ρ is the bending radius of the toroid and $p_\phi(\theta)$ describes the angular development of the path. The vectors of the local reference systems (Fig. 2.7) are the following ones:

$$\vec{t} = \frac{d\vec{p}(\theta)}{d\theta} = R\sin(\theta)\hat{r} + [\rho - R\cos(\theta)]p'_\phi(\theta)\hat{\phi} + R\cos(\theta)\hat{z} \tag{2.22}$$

$$\hat{\eta} = (-\cos(\theta), 0, \sin(\theta)) \tag{2.23}$$

$$\vec{b} = \vec{t} \times \hat{\eta} = [\rho - R\cos(\theta)]p'_\phi(\theta)\sin(\theta)\hat{r} - R\hat{\phi} + [\rho - R\cos(\theta)]p'_\phi(\theta)\cos(\theta)\hat{z} \tag{2.24}$$

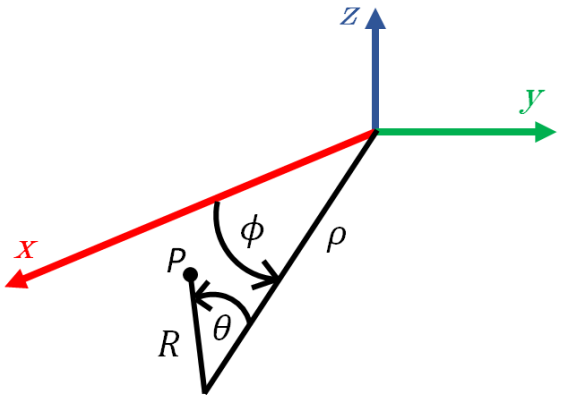

Figure 2.6: Cylindrical reference system for curved CCT.

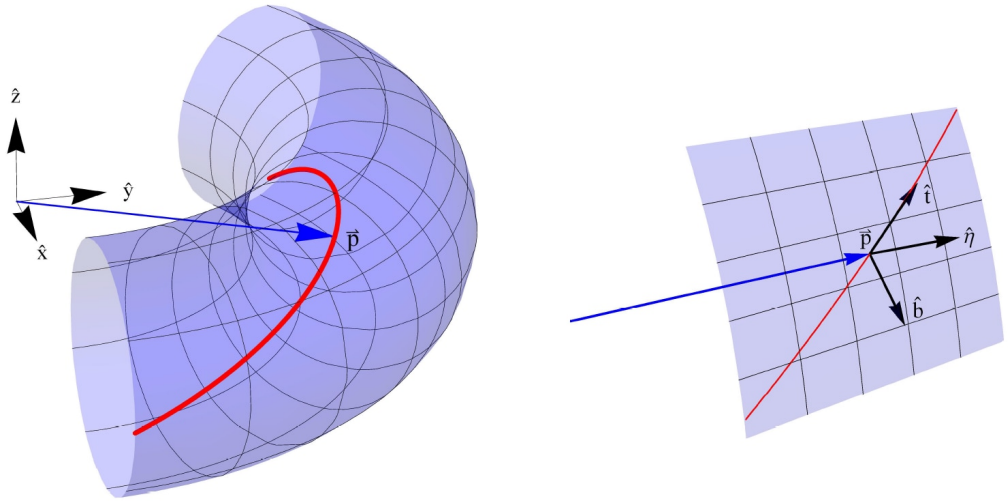

Figure 2.7: Beginning of the curved winding path and local reference system at a generic point of the path (Fig. from [9]). Courtesy of Lucas Nathan Brouwer.

As in the straight case, $p_\phi(\theta)$ needs to be periodic to generate a uniform region far from the extremities of the magnet:

$$|p_\phi(\theta + 2\pi) - p_\phi(\theta)| = \phi_0 \tag{2.25}$$

Where ϕ_0 is the pitch: the constant angular distance between consecutive turns (Fig. 2.8).

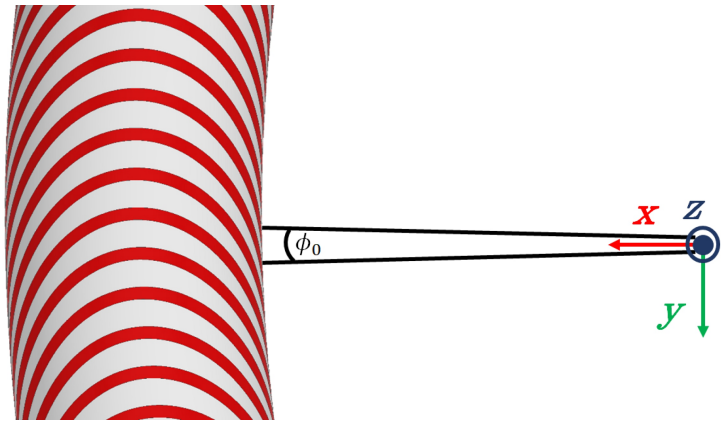

Figure 2.8: Angular pitch ϕ_0.

The angular pitch ϕ_0 still has to be higher than a minimun value. The situation is the same shown in Fig. 2.4, but this time, due to the circular geometry, w is replaced by $(\rho - R)\,\phi_0$ (Fig. 2.9):

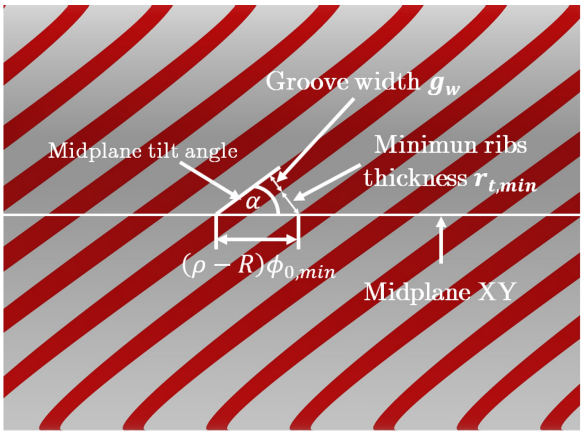

Figure 2.9: Definition of the minimum value of angular pitch $\phi_{0,min}$.

Under the hypothesis $R \gg (\rho - R)\phi_0$, which allows approximating the toroidal surface as planar close to the torus midplane, it is possible to define $\phi_{0,min}$ (Fig. 2.9):

$$\phi_{0,min} = \frac{g_w + r_{t,min}}{(\rho - R)\sin(\alpha)} \tag{2.26}$$

The ribs thickness is minimum on the torus midplane XY (Fig. 2.8) on the inner part of the toroid ($r = \rho - R$ and $z = 0$).
The perpendicular distance between two turns along the binormal vector is:

$$\delta(\theta) = [\rho - R\cos(\theta)]\,\phi_0\hat{\phi}\cdot\hat{b} \tag{2.27}$$

$$\delta(\theta) = [\rho - R\cos(\theta)]\phi_0\hat{\phi}\cdot\frac{[\rho - R\cos(\theta)]p'_\phi(\theta)\sin(\theta)\hat{r} - R\hat{\phi} + [\rho - R\cos(\theta)]p'_\phi(\theta)\cos(\theta)\hat{z}}{\sqrt{[\rho - R\cos(\theta)]^2 p'_\phi(\theta)^2 + R^2}} \tag{2.28}$$

$$\delta(\theta) = \frac{[\rho - R\cos(\theta)]\phi_0 R}{\sqrt{[\rho - R\cos(\theta)]^2 p'_\phi(\theta)^2 + R^2}} = \frac{[\rho - R\cos(\theta)]\phi_0 R}{|\vec{t}|} \tag{2.29}$$

Since $\delta(\theta)$ is a distance, the negative sign of $[\rho - R\cos(\theta)]\phi_0 R$ is neglected as in Section 2.1. The 2D cylindrical current sheet has an averaged current density:

$$\vec{j}(\theta) = \frac{I_0 \hat{t}}{\delta(\theta)} = \frac{I_0}{\delta(\theta)} \frac{\vec{t}}{|\vec{t}|} = \frac{I_0 |\vec{t}|}{[\rho - R\cos(\theta)]\phi_0 R} \frac{\vec{t}}{|\vec{t}|} \tag{2.30}$$

$$\vec{j}(\theta) = \frac{I_0 \left\{ R\sin(\theta)\hat{r} + [\rho - R\cos(\theta)]p'_\phi(\theta)\hat{\phi} + R\cos(\theta)\hat{z} \right\}}{[\rho - R\cos(\theta)]\phi_0 R} \tag{2.31}$$

Imposing that the azimuthal component of $j_\phi(\theta)$ is equal to $j_{0n\phi}\cos(n\theta)$:

$$\frac{I_0 p'_\phi(\theta)}{\phi_0 R} = j_{0n\phi}\cos(n\theta) \tag{2.32}$$

$$p'_\phi(\theta) = \frac{\phi_0 R j_{0n\phi}}{I_0}\cos(n\theta) \tag{2.33}$$

$$p_\phi(\theta) = \int \frac{\phi_0 R j_{0n\phi}}{I_0}\cos(n\theta)d\theta = \frac{\phi_0 R j_{0n\phi}}{I_0 n}\sin(n\theta) \tag{2.34}$$

To make the path the path advance along the longitudinal direction with a pitch equal to ϕ_0, it is necessary to add the term $\phi_0/(2\pi)$ to previous equation:

$$p_\phi(\theta) = \frac{\phi_0 R j_{0n\phi}}{I_0 n}\sin(n\theta) + \frac{\phi_0}{2\pi} \tag{2.35}$$

It is still possible to relate the winding path with free geometrical parameters under the assumption that $R \gg [\rho - R\cos(0)]\phi_0$ (Fig. 2.10):

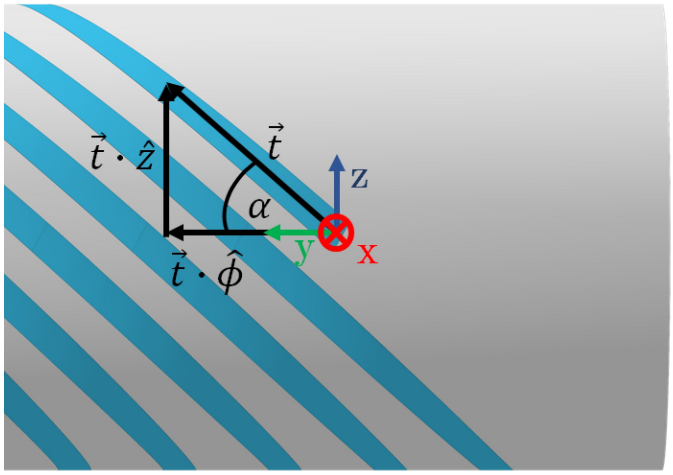

Figure 2.10: Definition of the midplane tilt angle for curved CCT.

$$\tan(\alpha) \equiv \left.\frac{\vec{t}\cdot\hat{z}}{\vec{t}\cdot\hat{\phi}}\right|_{\theta=0} = \left.\frac{\left\{R\sin(\theta)\hat{r} + [\rho - R\cos(\theta)]p'_{\phi}(\theta)\hat{\phi} + R\cos(\theta)\hat{z}\right\}\cdot(0,0,1)}{\left\{R\sin(\theta)\hat{r} + [\rho - R\cos(\theta)]p'_{\phi}(\theta)\hat{\phi} + R\cos(\theta)\hat{z}\right\}\cdot(0,1,0)}\right|_{\theta=0} \tag{2.36}$$

$$\tan(\alpha) = \frac{R}{(\rho - R)\left[\frac{\phi_0 R j_{0n\phi}}{I_0}\right]} \tag{2.37}$$

The function $p_{\phi}(\theta)$ of Eq. 2.35 can be rewritten as:

$$p_{\phi}(\theta) = \frac{R}{n(\rho - R)\tan(\alpha)}\sin(n\theta) + \frac{\phi_0}{2\pi} \tag{2.38}$$

In the end, Eq. 2.21 becomes:

$$\vec{p}(\theta) = [\rho - R\cos(\theta)]\hat{r} + \left[\frac{R}{n(\rho - R)\tan(\alpha)}\sin(n\theta) + \frac{\phi_0}{2\pi}\right]\hat{\phi} + [R\sin(\theta)]\hat{z} \tag{2.39}$$

As in the straight case, it is possible to add a term that centres the magnet (this time with respect to the XZ plane) and rewrite Eq. 2.39 considering the presence of several magnetic field harmonics:

$$\vec{p}(\theta) = [\rho - R\cos(\theta)]\hat{r} + \left[\frac{\phi_0}{2\pi}\theta - \frac{n_t\phi_0}{2} + \sum_{n=1} a_n\sin(n\theta)\right]\hat{\phi} + [R\sin(\theta)]\hat{z} \tag{2.40}$$

Electromagnetic simulations gave the following results for a_n (Table 2.2):

Coefficient	Ropes Configuration	Rutherford Configuration
a_1	0.525 rad	0.525 rad

Table 2.2: Coefficient for the dipolar curved CCT.

2.3. Current Leads and Layer Jump

Eq. 2.20 and Eq. 2.40 describe the sinusoidal part (wound on cylindrical and toroidal surface) of the winding path, but other two components need to be modelled: the current leads and the layer jump (Fig. 2.11).

The current leads (Fig. 2.11a) are the part of the conductor which connects to the power converter, which provides current. They are composed of a first straight portion and a second one that connects to the sinusoidal path.

The layer jump (Fig. 2.11b) is the part of the conductor that connects the inner and external layers with a smooth junction between two curves: the sinusoids of the inner and external layers. The layer jump is not always present. In this case there are two separated conductors (one for each layer). If the layer jump is present there is one single conductor.

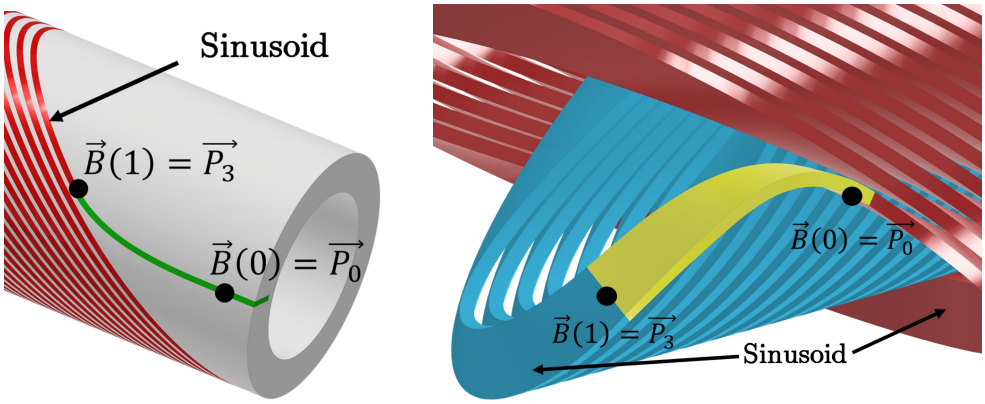

(a) (b)

Figure 2.11: Picture of the current lead (green) in (a) and layer jump (yellow) in (b).

Both current leads and layer jump must be modelled with an equation that matches the continuity and derivability of the two curves linked in the connection points. Moreover, the equation must be continuous and derivable along its whole path. For these reasons, the two components were modelled with cubic Bézier curves [2]:

$$\vec{B}(t) = (1-t)^3\overrightarrow{P_0} + 3t(1-t)^2\overrightarrow{P_1} + 3t^2(1-t)\overrightarrow{P_2} + t^3\overrightarrow{P_3}, \quad t \in [0,1] \tag{2.41}$$

$$\dot{\vec{B}}(t) = 3(1-t)^2\left(\overrightarrow{P_1} - \overrightarrow{P_0}\right) + 6(1-t)t\left(\overrightarrow{P_2} - \overrightarrow{P_1}\right) + 3t^2\left(\overrightarrow{P_3} - \overrightarrow{P_2}\right), \quad t \in [0,1] \tag{2.42}$$

A Beziér curve guarantees continuity and derivability along all its path. In particular, a cubic Beziér curve as Eq. 2.41 is made by four points: the first point $\vec{P_0}$ and the last point $\vec{P_3}$ are fixed because they are the extremities of the two curves which must be joint. The intermediate points $\vec{P_1}$ and $\vec{P_2}$ can be determined by imposing the equality of the derivatives in the connection points:

$$\dot{\vec{B}}(0) = 3\left(\overrightarrow{P_1} - \overrightarrow{P_0}\right) \tag{2.43}$$

$$\dot{\vec{B}}(1) = 3\left(\overrightarrow{P_3} - \overrightarrow{P_2}\right) \tag{2.44}$$

Higher order Bézier curves were evaluated since this gives a smoother connection thanks to the imposition of higher order derivatives. However, it was observed that this can lead to many concavity changes along the Bézier curve, which imposes higher values of strain to the conductor losing efficiency in the winding process.

There is one more constraint in the case of current leads: the curve must lay on a cylindrical surface. For this reason, the winding path was unwound on a plane where the points of the Bézier curve were calculated (Fig. 2.12). After this step, the obtained curve was winded on the cylindrical surface using the Autodesk Inventor options “Project curve to surface” and “Wrap to surface”.

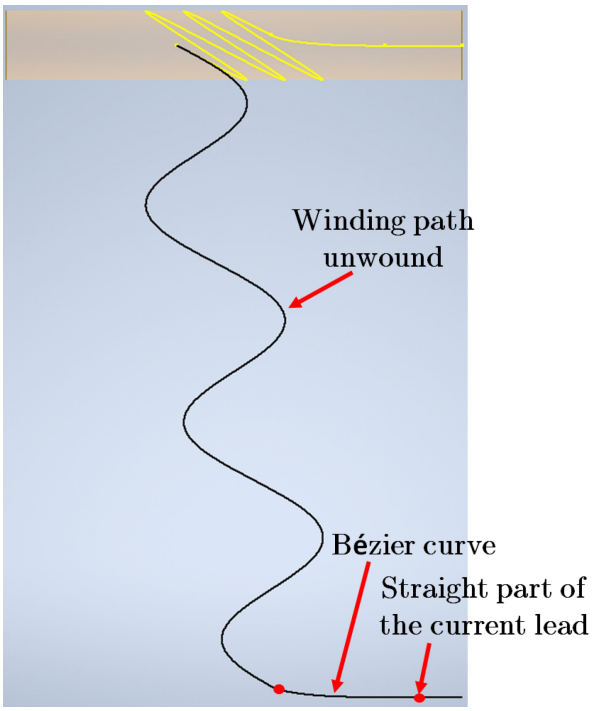

Figure 2.12: Unwound winding path.

2.4. CAD Model Steps

The CAD model was made to obtain a completely parametric model, which updates automatically in case of change of parameters' values and can contain up to 8 different harmonics with both normal and skew coefficients (Appendix A explains normal and skew coefficients).
The geometry of the CCT is complex, especially in case of high order harmonics, so Autodesk Inventor has difficulties to update correctly in case of huge variations of the overall shape. The problems encountered were solved by dividing the CAD model into more elementary steps:

1. Generation of the first turn of the conductor (Fig. 2.13):

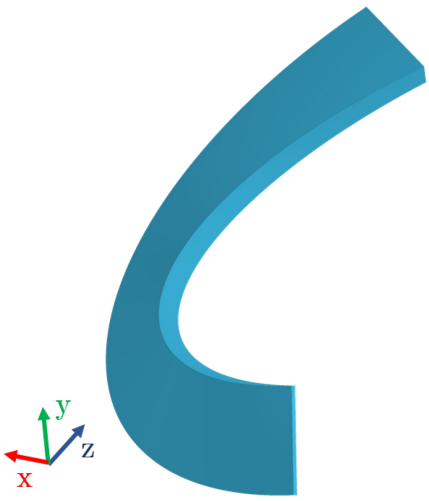

Figure 2.13: First turn.

2. Generation of the second turn (Fig. 2.14):

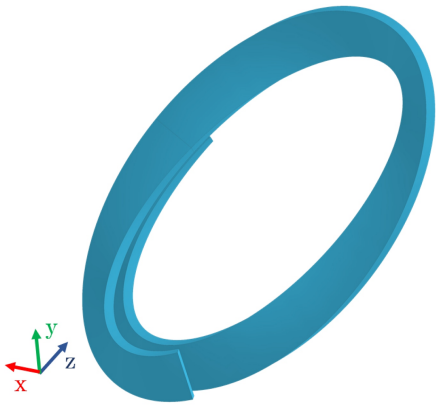

Figure 2.14: Addition of the second turn.

3. Repetition of the second turn $n_t - 2$ (n_t is the number of turns) times using the pattern command. The first and last turns are slightly different from the others due to their connections with the layer jump and the current leads. So, they are built separately because the pattern command repeats an object perfectly equal (Fig. 2.15):

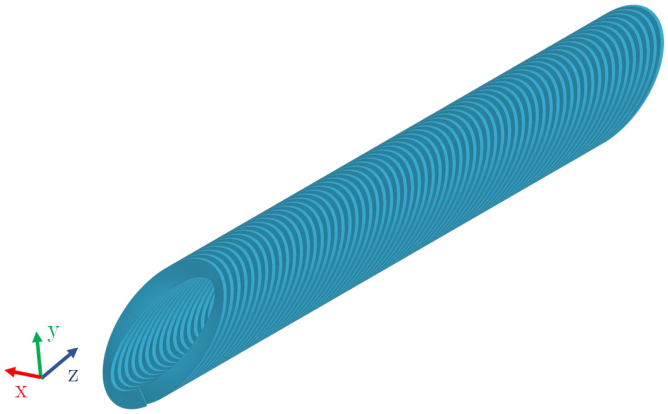

Figure 2.15: Repetition of the second turn.

4. Addition of the last turn (Fig. 2.16):

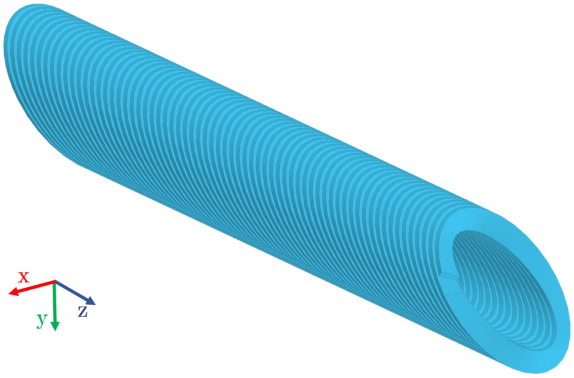

Figure 2.16: Last turn addition.

5. Inclusion of the current lead (Fig. 2.17):

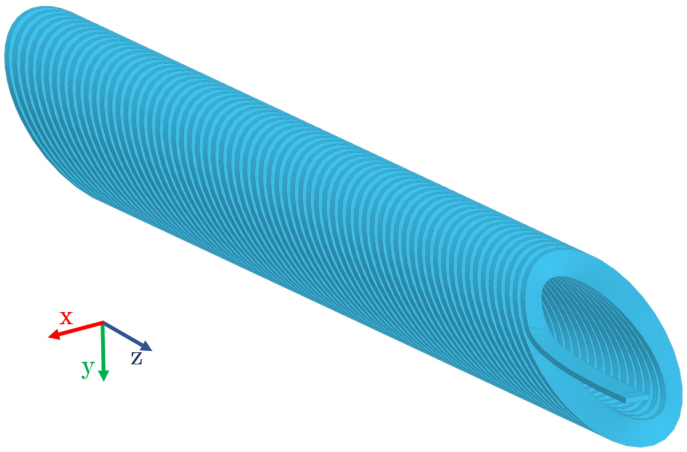

Figure 2.17: Generation of the current lead for the inner layer.

6. Repetition of the previous steps for the external layer (Fig. 2.18):

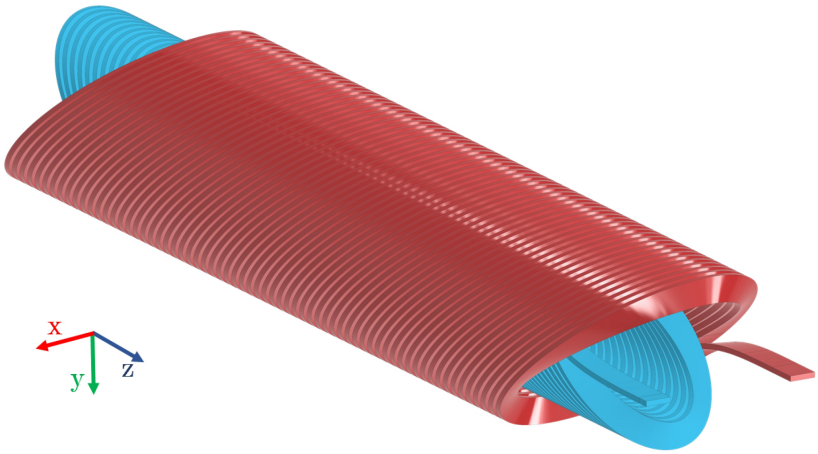

Figure 2.18: Generation of the external layer.

7. Insertion of the layer jump (Fig. 2.19):

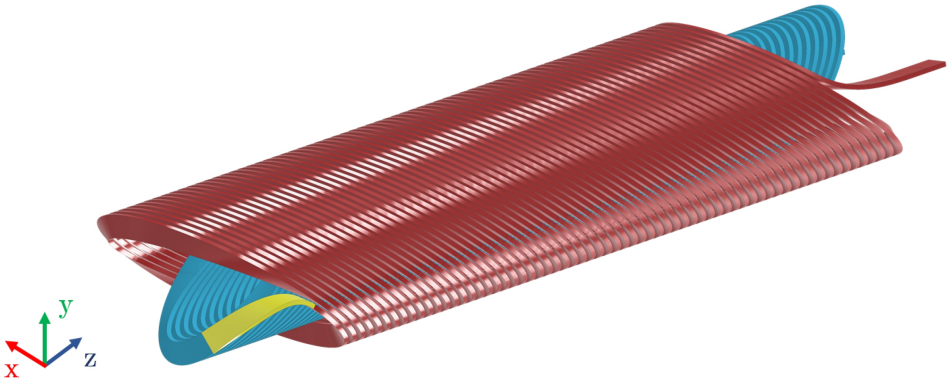

Figure 2.19: Addition of the layer jump (yellow).

8. Use of the conductor to cut the cylinder to obtain the formers. The conductor is made first because the software has more difficulty cutting than building a solid body (Fig. 2.20):

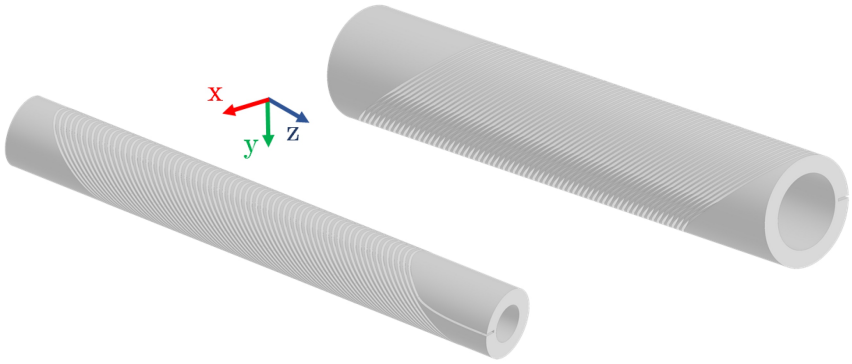

Figure 2.20: Final formers.

The same procedure applies to both straight and curved CCT magnets.
The steps from 1 to 7 were performed using the method shown in Fig. 2.21 (case of step 2). The winding path is generated using a Sweep function, which requires as input the cross-section of the conductor and two curves: a guide and a path). The path curve has Eq. 2.20 (straight CCT) or Eq. 2.40 (curved CCT) for $2\pi \leq \theta \leq 4\pi$ and the guide curve is equal to the path curve displaced by the groove height along the normal direction to the cylindrical or toroidal surface pointing outward.

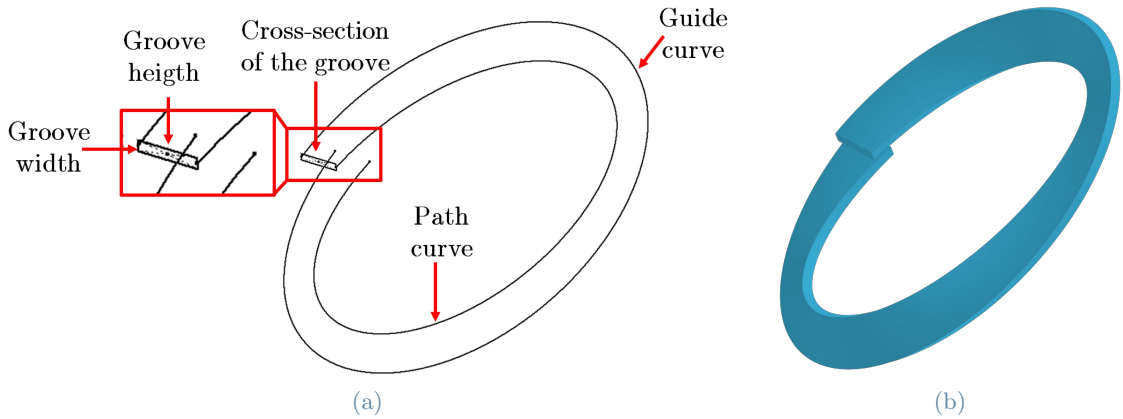

Figure 2.21: Input (a) and output (b) of the Sweep function.

2.5. Parametric Model

The Inventor CAD model is completely parametric and controlled by an external Excel sheet containing all the model's parameters and values. To obtain the new model in case of change of the parameters' values, it is sufficient to modify the values in Excel and the CAD model updates automatically. This gives enormous advantages:

- The user does not have to remake the whole or part of the model each time the parameters must be modified.

- The user does not need to know how to use the CAD software.
- The risk of making mistakes is minimized, and the magnet development process speeds up. In this way, the new geometry is obtained extremely quickly and in a reliable manner which is fundamental during the design phase to study the behaviour of all the different components.

To conclude this chapter, the pictures of the final CAD models used for FEM simulations are shown (Fig. 2.22). Moreover, some pictures of other CCT magnets with combined function layouts are shown as an example of the potentiality of CAD the model (Fig. 2.23 and Fig. 2.24).

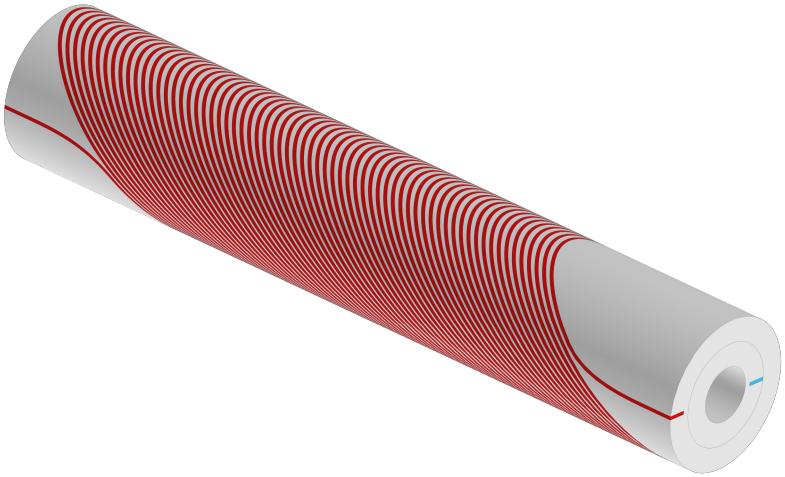

(a)

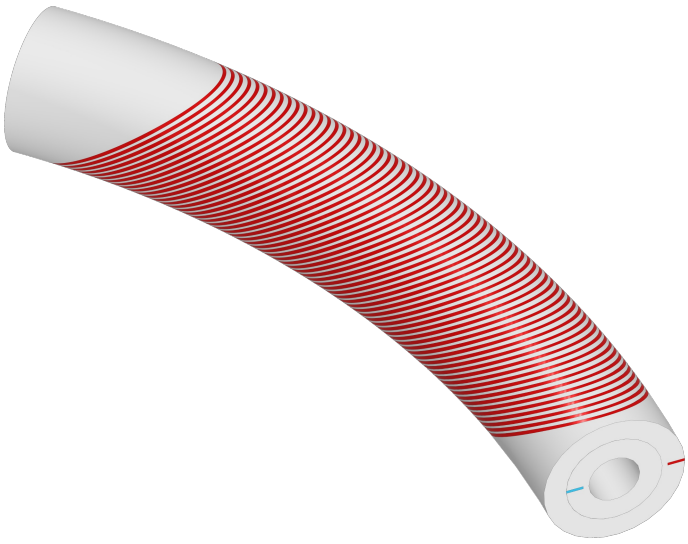

(b)

Figure 2.22: Models of straight and curved CCT magnets used for FEM simulations.

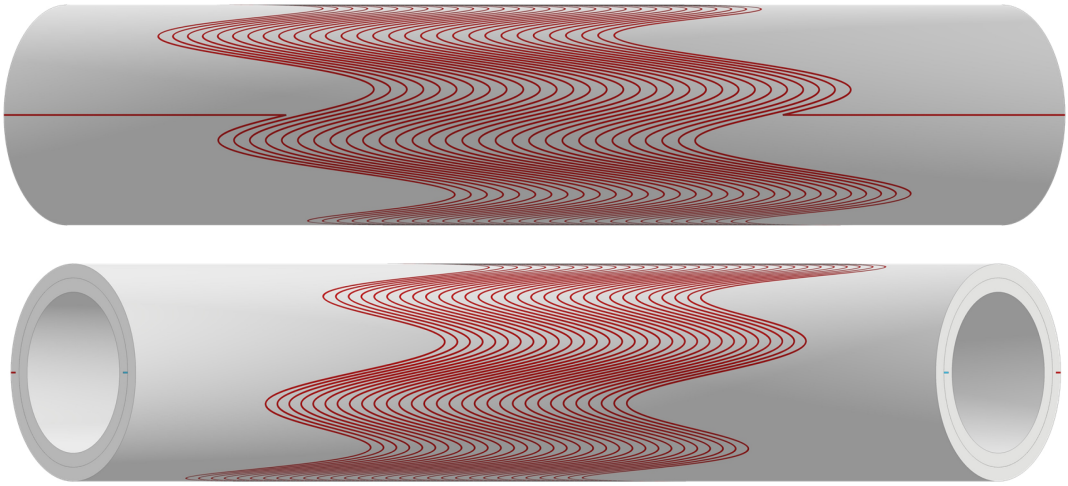

Figure 2.23: Combined function (dipole, dodecapole) curved CCT.

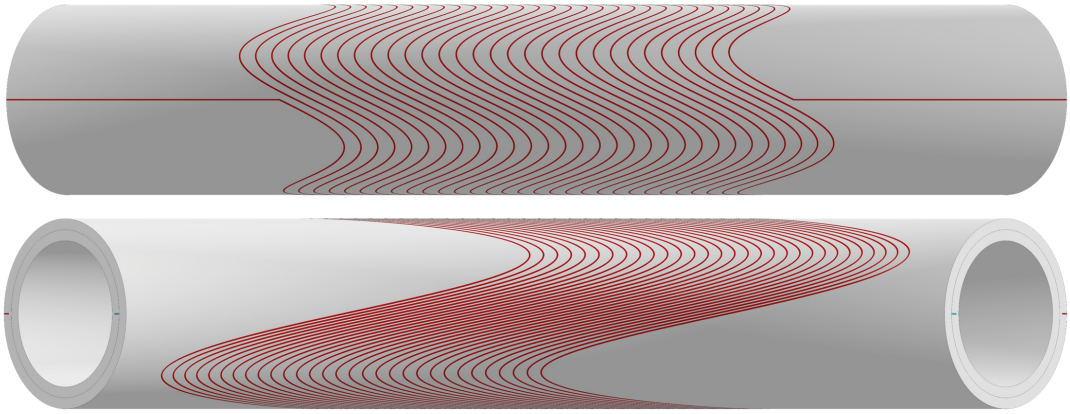

Figure 2.24: Combined function (dipole, quadrupole, sextupole) curved CCT. Here is possible to see the variation of the ribs thickness between the inner part and the external part of the toroid.

3 | First FEM Simulations

This chapter describes the FEM simulations carried out to have a first evaluation of the CCT's mechanical behaviour.

The second step of the thesis was to carry out Finite Element Method (FEM) simulations to have a preliminary evaluation of the magnet's behaviour. The simulations considered the ropes configuration magnet (whose parameters are reported in Table 1.1) since it is the most probable configuration which will be used for the magnet demonstrators. Simulations started with the case of straight CCT since it is easier to model in FEM software than the curved one. Furthermore, with respect to the mechanical behaviour, minor differences are expected in the centre of the magnet (where results are evaluated) between the straight and curved case. In this stage, the iron yoke around the CCT is not included in FEM simulations for two main reasons. The first one is that electromagnetic simulations without iron yoke require much less computational time. So, it is possible to find the geometrical parameters which give the needed magnetic field speeding up the design process (the addition of iron yoke changes mainly the magnitude of the field, while the effect on field harmonics is much lower). The second reason for excluding iron yoke is that this is the most severe case for mechanics. The iron yoke permits obtaining the same magnetic field with a lower current, thus reducing the magnitude of Lorentz forces.

3.1. Electromagnetic Simulations

The first stage of the FEM modelling was to carry out electromagnetic simulations since they are necessary to check the generated magnetic field and obtain the Lorentz force densities for mechanical simulations. The electromagnetic forces were extracted from COMSOL simulations (which imported the CAD model described in Chapter 2) made by other researchers involved in HITRI*plus* and IFAST. The magnetic field magnitude obtained from the electromagnetic simulations is reported in Fig. 3.1.

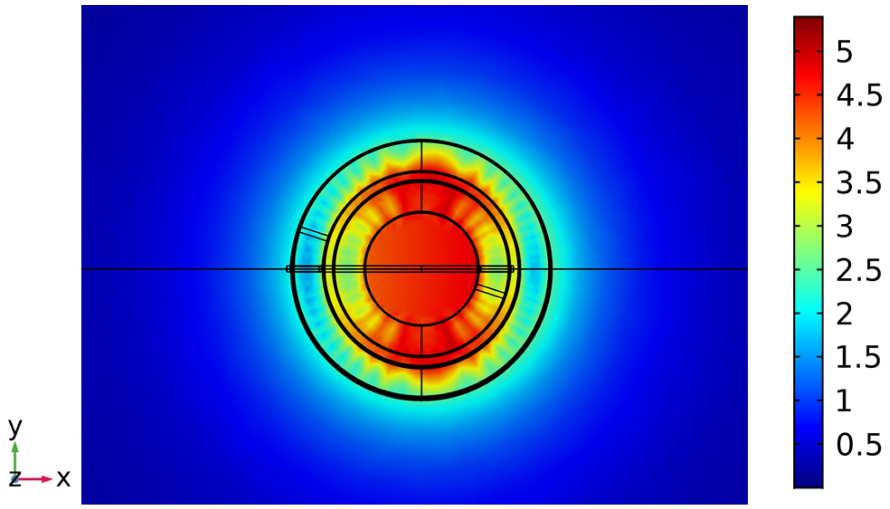

Figure 3.1: Magnitude of the magnetic field at the centre of the magnet (XY plane). Courtesy of Ernesto De Matteis.

Fig. 3.1 shows that the magnetic field at the centre of the the bore area is of 4.5 T, while the peak field in the conductors is 5.5 T. The shape of the field is the one of a dipolar field with a slight asymmetry (with respect YZ plane) due to the quadrupolar harmonic. To validate the COMSOL model, the results were compared with another software (OPERA3D) whose model is completely independent on the COMSOL model. The comparison was done along the axis of the CCT (z-axis) where the quadrupolar component is null, and just the dipolar field is present ($\vec{B} = B_y\hat{y}$). The agreement of the results is really good (Fig. 3.2), since the difference is just 0.15%. Higher differences are obtained in the magnet extremities due to the absence of current leads in OPERA3D simulations.

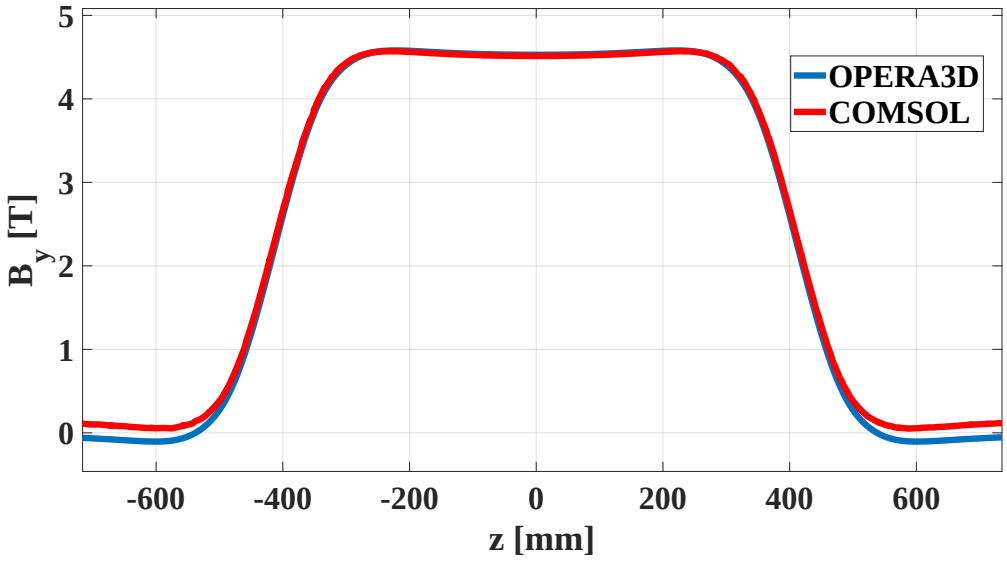

Figure 3.2: Comparison of OPERA3D and COMSOL results for the magnetic field along the magnet's axis (Courtesy of Ernesto De Matteis and Samuele Mariotto).

3.2. Mechanical Simulations

The magnet was divide into four quadrants (Fig. 3.3) along the longitudinal direction. This allows for calculating Lorentz force densities in the single quadrants and evaluating their symmetries with respect to the XZ and YZ planes (Table 3.1).

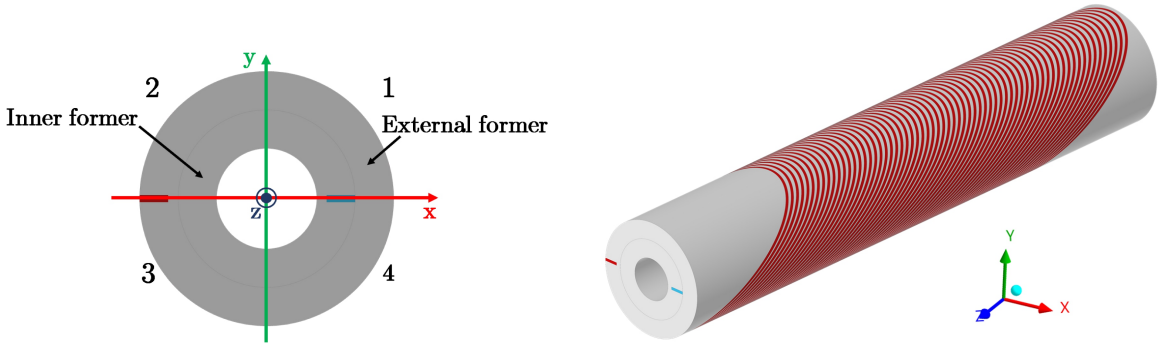

(a) (b)

Figure 3.3: CCT quadrant division.

Forces	Quadrant 1	Quadrant 2	Quadrant 3	Quadrant 4
F_x [N]	6.65e5	-6.65e5	-6.65e5	6.65e5
F_y [N]	-4.05e5	-2.91e5	2.91e5	4.05e5
F_z [N]	-46,224	-32,532	32,534	46,215

Table 3.1: Lorentz forces in the four quadrants of Fig. 3.3.

The forces are well symmetric with respect to the XZ and YZ planes. So, to reduce the computational cost, just one quarter of the CCT (Fig. 3.4) was simulated imposing proper boundary conditions on the XZ and YZ planes: the displacement along x-axis of the faces on YZ plane is null (Fig. 3.5), while the faces on XZ plane cannot move along y-axis (Fig. 3.6).

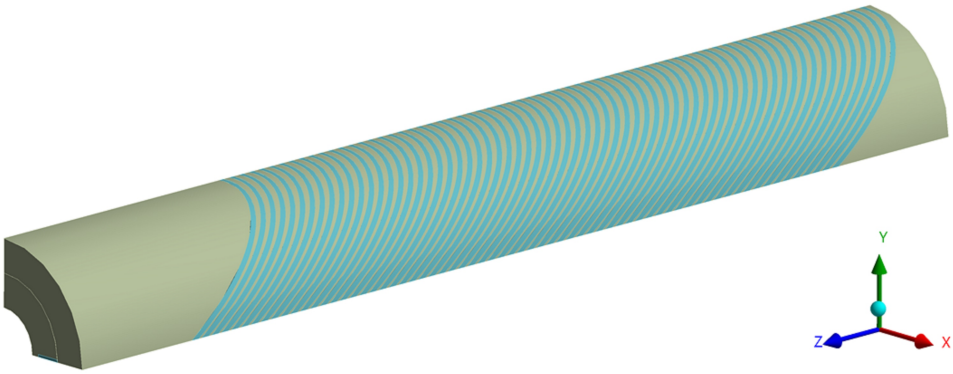

Figure 3.4: One quarter of the CCT magnet.

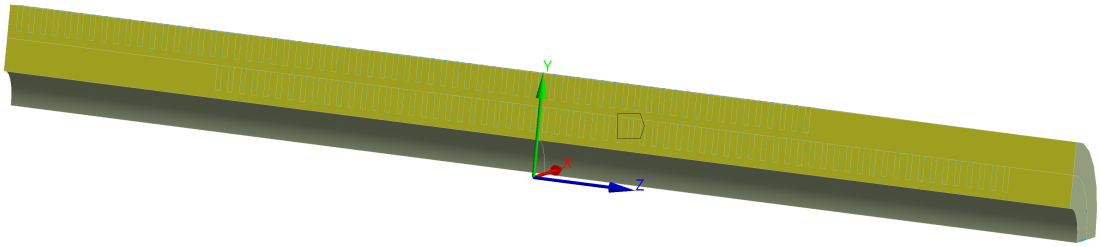

Figure 3.5: The yellow faces lay on the YZ plane and cannot move along x-axis.

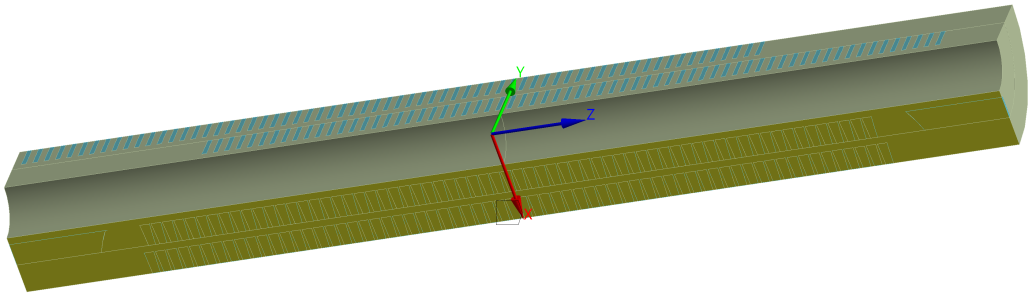

Figure 3.6: The yellow faces lay on the XZ plane and cannot move along y-axis.

The following design (Fig. 3.7) was used as reference for the other constraints and components used in the simulation:

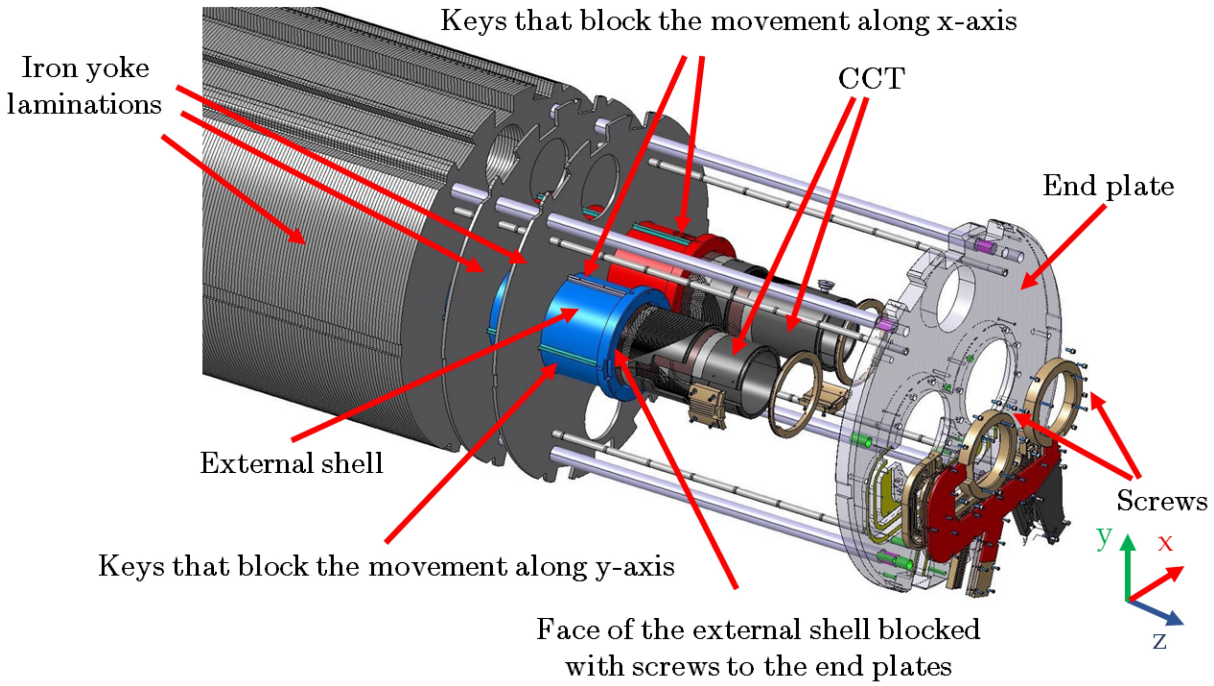

Figure 3.7: Exploded view of the drawing LHCMCBRD0050 (Courtesy of Glyn Kirby).

It is important to keep in mind that the design of Fig. 3.7 is just a reference for the constraints needed to carry out the very first simulations. In fact, the magnetic field of the reference is 2.65

T, while the CCT of the thesis generates 4.5 T.
In Fig. 3.7 there are two CCTs for two particle beams, but in the case of the thesis there is just one particle beam and one CCT.
In the assembly of Fig. 3.7 the magnet is surrounded by an external shell (connected to the CCT by epoxy resin) which must contain the CCT deformation (race track deformation) due to Lorentz forces. One end of the shell is connected to the end plate through screws that block all the movements, while the other end of the shell is free to move longitudinally to allow thermal contraction. Moreover, four keys are present on each magnet: two block the movement along the x-axis and the other two along the y-axis. In this way also the rotation around the z-axis is blocked.
The shell and the described constraints were added to the single quarter of the CCT in Fig. 3.4 to obtain the final ANSYS model (Fig. 3.8). The role of the keys is represented by boundary conditions shown in Fig. 3.5 and Fig. 3.6, which are applied to both CCT and shell. The block caused by screws on one extremity of the shell is modelled by blocking the displacements of the shell's face along x, y, and z axes (Fig. 3.8).
In Fig. 3.7 iron yoke is present, but, as mentioned at the beginning of this chapter, iron was not considered in electromagnetic simulations since this is the most severe case for mechanics. Moreover, the structural role of the iron yoke for the CCT is to keep the keys needed for the magnet's alignment in the correct position. Since the iron yoke has high stiffness, it can be modelled with rigid supports to the keys. In the ANSYS model, this corresponds to the boundary conditions of Fig. 3.5 and Fig. 3.6, so the iron yoke is not present in the ANSYS model (Fig. 3.8).

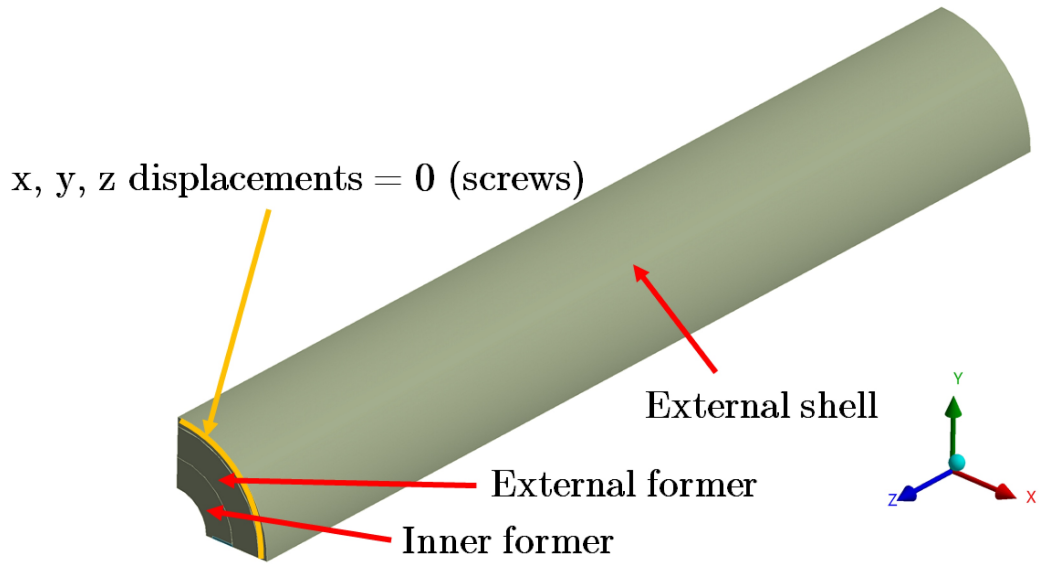

Figure 3.8: ANSYS mechanical model. The boundary conditions of Fig. 3.5 and Fig. 3.6 are applied to both CCT and shell. The contacts among the formers, conductors and shell are bonded because the two layers of CCT are impregnated with resin (needed to insulate the conductors and block their movement) which prevents the relative movement among the parts in contact.

3.2.1. Materials

The first materials considered for the CCT formers and the external shell were aluminium 6082-T6, aluminium bronze 954, titanium alloy (Ti 6Al 4V) and AISI 316L. The main candidate is aluminium bronze 954 since it has high rigidity and is easier to machine than titanium and AISI 316L. The properties of the materials are reported in Table 3.2.

Material	**Temperature T [K]**	**Young's Modulus E [GPa]**	**Poisson Ratio ν [-]**	**Tensile Yield Strength Y_s [MPa]**	**Coefficient of Thermal Contraction $\alpha_{293K-4.2K}$ [1/K]**	**Reference**
Aluminium 6082-T6	293	70.1	0.338	450 (110 K)	14.2e-6	[24]
	4.2	77.7	0.327			
Aluminium Bronze 954	293	110	0.316	640 (4 K)	10.8e-6	[24]
	4.2	114.4	0.316			
Titanium Alloy	293	115	0.3	1700 (20 K)	5.8e-6	[22] [10]
	4.2	125	0.3			
AISI 316L	293	195	0.3	610 (4 K)	9.9e-6	[22] [20]
	4.2	215	0.3			

Table 3.2: Formers' material properties.

The same material was used for the two formers and the external shell in each simulation.
The conductor cable of Nb-Ti and the surrounding resin were modelled as a single homogenized orthotropic material [24] whose properties (Table 3.3 and Table 3.4) are referred to the local reference system of the winding path (Fig. 3.9 and Fig. 3.10). A homogenization technique was used to obtain realistic coil properties to account for the Nb-Ti strands and the cured resin [24].

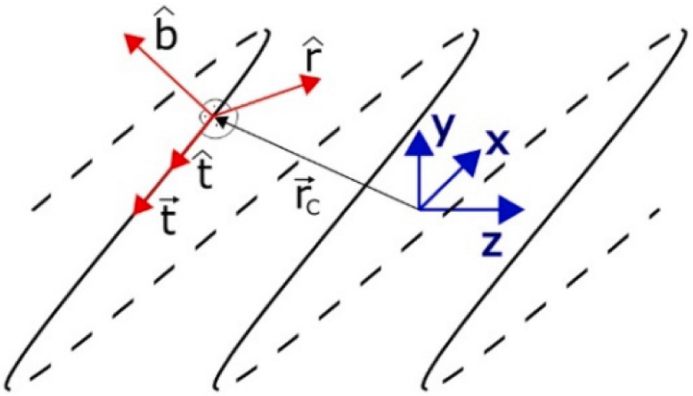

Figure 3.9: Local reference system of the winding path (Fig. from [24]). Courtesy of Glyn Kirby.

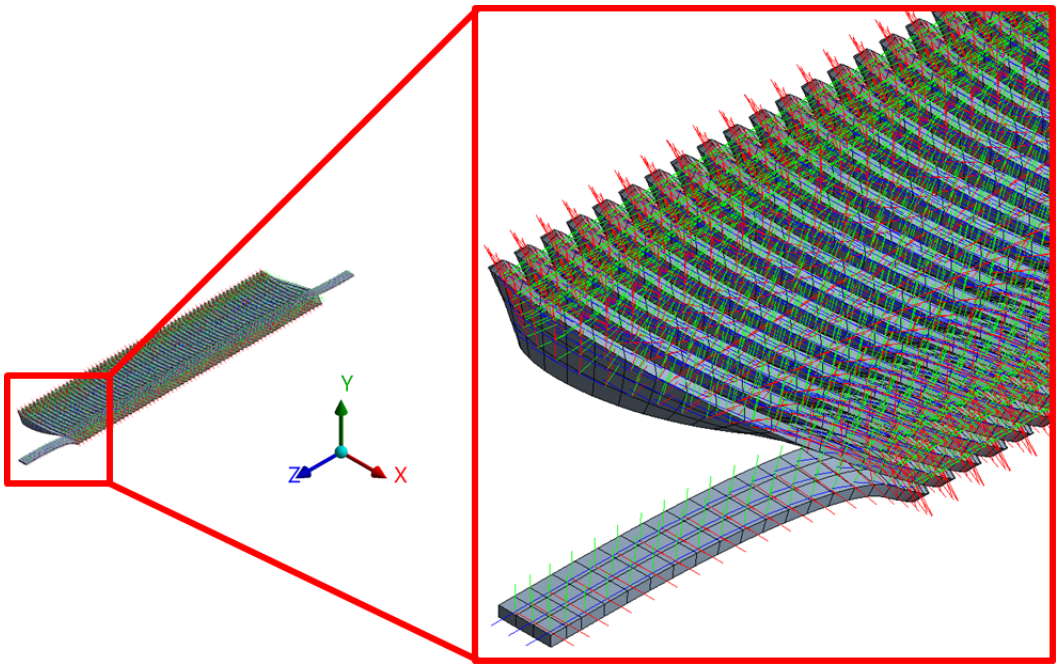

Figure 3.10: Local reference system of the mesh's elements of the conductor.

T [K]	E_r [GPa]	E_b [GPa]	E_t [GPa]	ν_{rb} [-]	ν_{bt} [-]	ν_{rt} [-]	G_{rb} [GPa]	G_{bt} [GPa]	G_{rt} [GPa]	Y_s [MPa]
293	11.9	11.9	59.0	0.36	0.07	0.07	2.57	3.45	3.45	300
4.2	25.8	25.8	61.2	0.38	0.16	0.17	5.7	7.27	7.27	

Table 3.3: Mechanical properties of the homogenized orthotropic material [24] along the radial r, binormal b and tangential t directions. T is the temperature, E is the Young's modulus, ν is the Poisson's ratio, G is the shear modulus and Y_s is the tensile yield strength.

$\alpha_{r,293K-4.2K}$ [1/K]	$\alpha_{b,293K-4.2K}$ [1/K]	$\alpha_{t,293K-4.2K}$ [1/K]
23.9e-6	23.9e-6	9.85e-6

Table 3.4: Coefficients of thermal contraction [24] of the homogenized orthotropic material along the radial r, binormal b and tangential t directions.

3.2.2. Loads

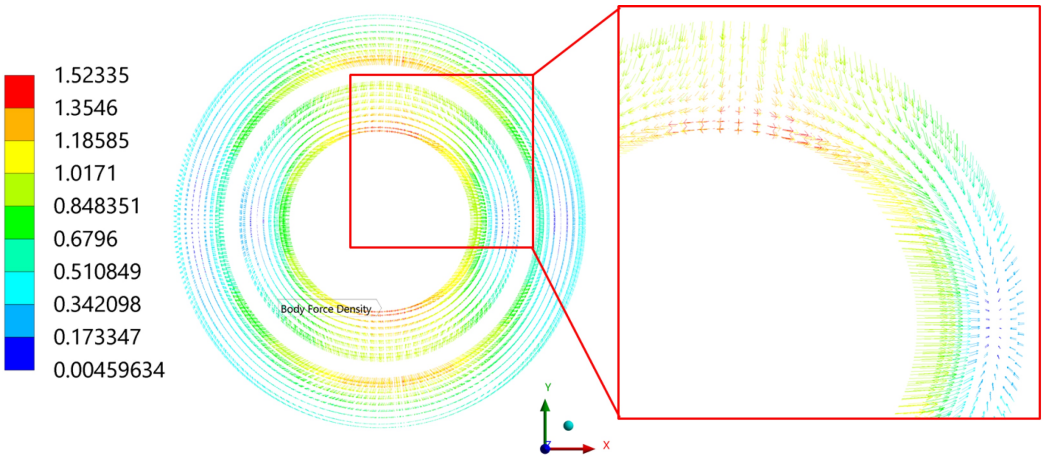

Figure 3.11: Lorentz forces densities (expressed in N/mm^3) applied to the conductors.

The simulations were carried out in two subsequent steps. During the first one, the cool down from 293 K to 4.2 K (required to achieve the superconducting state of Nb-Ti conductors) was applied. In the second step, Lorentz forces (Fig. 3.11) were applied to simulate the energization of the magnet once at cold.

3.2.3. Submodelling technique

The submodelling [5] technique was applied to see the results of the simulations more in detail. This method consists in carrying out a first 3D simulation of the whole assembly with a relatively coarse mesh (Fig. 3.12). Then, a second simulation of just the part of interest in the assembly is performed. In the second simulation, the displacements (which have lower dependence on mesh density than stresses and strains) are imported and mapped at the cut boundaries from the first simulation. Since just the part of interest is simulated, it is possible to use a finer mesh and evaluate stresses and strains with higher accuracy. The straight CCT is axially periodic (Fig. 2.3): far from the magnet's extremities, the formers can be built by many slices (as the one shown in Fig. 3.12) with axial length equal to the winding path's pitch w (Fig. 2.3, Eq. 2.20) placed in series along z-axis. Also the loads applied are axially periodic, therefore stresses and strains are periodic too. So, it is interesting to see the results in a single periodic slice using the submodelling method (Fig. 3.12). The slice selected is at the centre of the magnet (z = 0) since it is the most distant one from the CCT extremities. The axial extension of this slice is $-w/2 \leq z \leq w/2$. To apply submodelling and avoid boundary effects in the region of interest, it is necessary to cut the full 3D model distant from the region of interest. For this reason the submodel is made by 7 slices ($-7w/2 \leq z \leq 7w/2$). The axial length of the submodel was varied to see the effect on the results in the slice of interest and it was noticed that with 7 slices or more, results do not change.

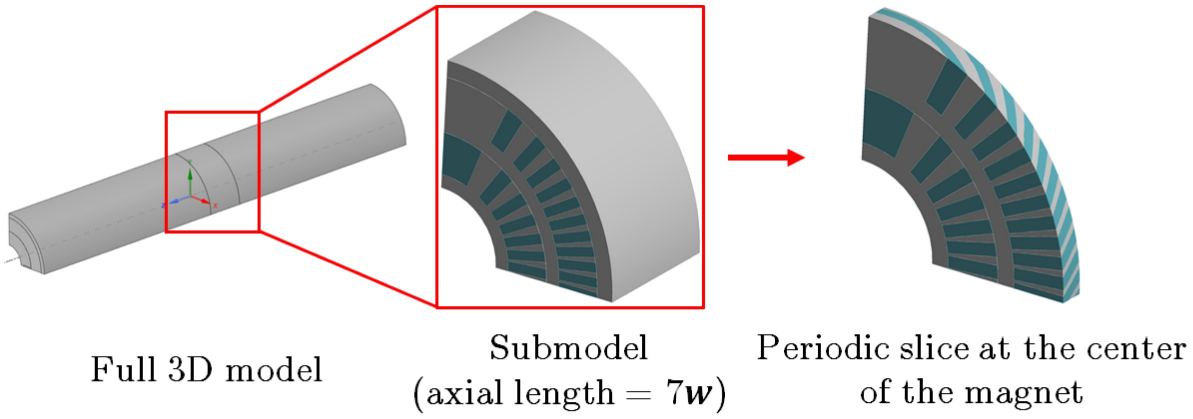

Figure 3.12: Full 3D model, submodel and periodic slice at magnet's centre. In the slice, the blue bodies are the conductors, while the grey bodies are the two formers. w indicates the pitch of the CCT's winding path (see Fig. 2.3).

3.2.4. Formers' Displacements

The displacements of the former with respect to the magnets' axis are fundamental because they change the magnet's initial shape and determine the conductor's position (current lines), affecting the magnetic field and its quality. Thermal contraction makes the CCT smaller but keeps the original magnet's shape, thus maintaining high field quality. Instead, Lorentz forces ovalize the magnet and change its shape and field quality. So, in this preliminary design, it is essential only to evaluate the displacements given by the electromagnetic forces. For this reason, it is necessary to subtract from the final results shown by ANSYS (step 2 of the simulation) the intermediate results of the cool down step (step 1 of the simulation). The result of this subtraction is shown in Fig. 3.13. Additionally, despite the intrinsic 3D nature of the CCT, the distribution of the displacements is uniform through the 3D CCT's periodic slice (Fig. 3.13a and Fig. 3.13b), so it is possible to evaluate the displacements just on the XY plane which is at the mid of the periodic slice (Fig. 3.13c and Fig. 3.13d).

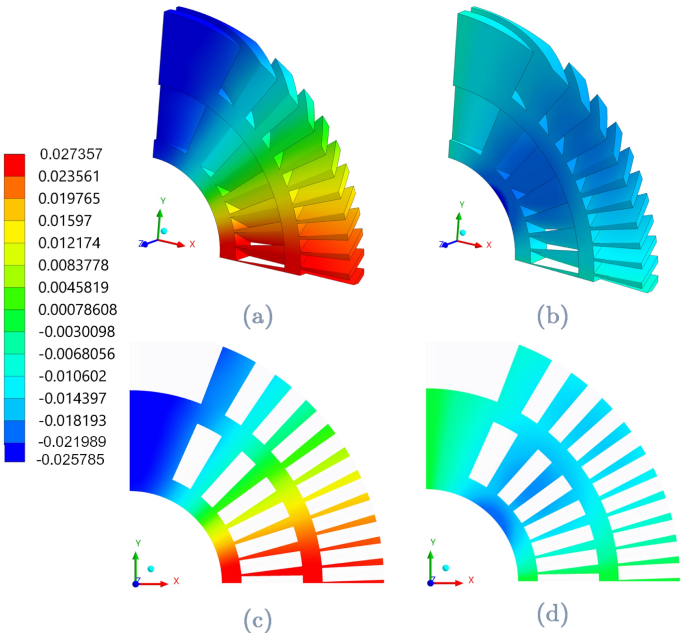

Figure 3.13: Displacements of the formers due to electromagnetic forces, expressed in mm, in the case of formers made of aluminium bronze 954. Pictures (a) and (c) show the radial displacements, while (b) and (d) show the azimuthal (circumferential) displacements.

The radial displacements u_ρ were evaluated to check if the CCT keeps its original circular shape. To keep the magnet circular, the difference of radial displacement (due to Lorentz forces) for points that lay on the same radius (Fig. 3.14 and Fig. 3.15) must remain within a certain limit. The determination of this limit requires further studies beyond this thesis's scope, which consists in a preliminary design. For this reason, the magnitude of this limit is assumed to be equal to 0.1 mm. The same limit was assumed for all the other quantities of interest related to the formers' displacements.

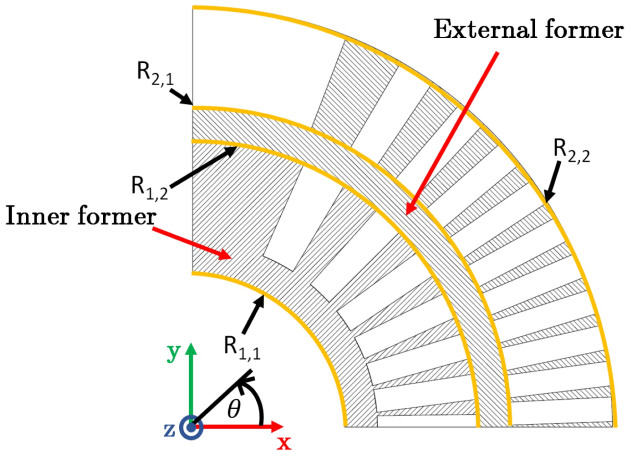

Figure 3.14: Radii where the difference of radial displacement was evaluated.

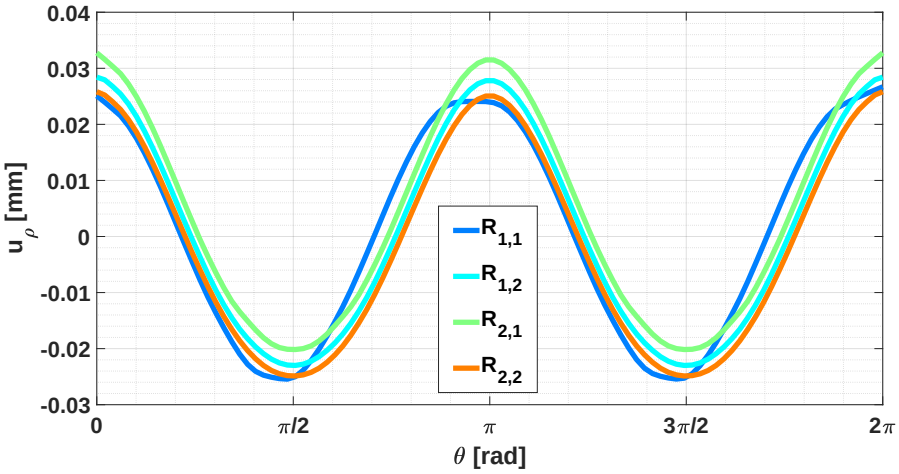

Figure 3.15: Radial displacements (due to Lorentz forces) at the radii of Fig. 3.14 in the case of formers made of aluminium bronze 954.

Formers' material	$\Delta u_\rho^{R1,1}$ [mm]	$\Delta u_\rho^{R1,2}$ [mm]	$\Delta u_\rho^{R2,1}$ [mm]	$\Delta u_\rho^{R2,2}$ [mm]
Aluminium 6082-T6	0.063	0.066	0.067	0.065
Aluminium Bronze 954	0.050	0.052	0.052	0.051
Titanium Alloy	0.047	0.049	0.049	0.048
AISI 316L	0.035	0.036	0.037	0.035

Table 3.5: Maximum difference of radial displacement Δu_ρ for the points which lay on the same radius $R_{i,j}$ of Fig. 3.14.

The results of Table 3.5 show that all quantities remain below the limit of 0.1 mm in each case. Another evaluation to check the circularity of the magnet is assessing the radial displacements $u_{\rho,i}$ of some significant points (Fig. 3.16). The subscript i indicates the point to which u_ρ refers.

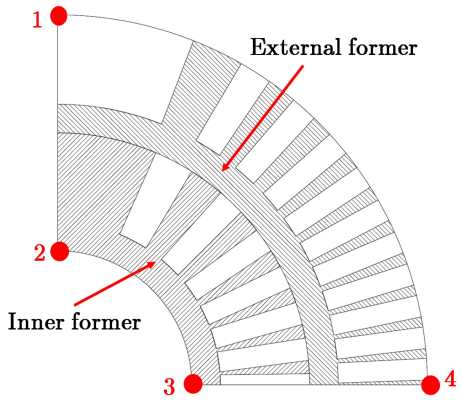

Figure 3.16: Significant points of the formers to evaluate the circularity of the magnet.

It is necessary to check the following quantities related to the significant points of Fig. 3.16:

- The magnitude of the displacements u_ρ of the points (Table 3.6), since the position of the current lines must not be too different from the initial one.

- The difference between $u_{\rho,2}$ and $u_{\rho,3}$ (Table 3.7) must be low. If $u_{\rho,2}$ and $u_{\rho,3}$ are too different, the shape of the magnet is no more circular but elliptical thus affecting field quality.
- The last quantities to check are $(u_{\rho,1} - u_{\rho,2})$ and $(u_{\rho,3} - u_{\rho,4})$, shown in Table 3.7, to evaluate the change of thickness of the magnet.

All the quantities which must be checked remain below the limit of 0.1 mm.

Formers' material	$u_{\rho,1}$ **[mm]**	$u_{\rho,2}$ **[mm]**	$u_{\rho,3}$ **[mm]**	$u_{\rho,4}$ **[mm]**
Aluminium 6082-T6	-0.035	-0.030	0.033	0.031
Aluminium Bronze 954	-0.026	-0.023	0.027	0.025
Titanium Alloy	-0.024	-0.022	0.026	0.024
AISI 316L	-0.017	-0.016	0.019	0.018

Table 3.6: Radial displacements $u_{\rho,i}$ of the significant points of Fig. 3.16.

Formers' material	$u_{\rho,2} - u_{\rho,3}$ **[mm]**	$u_{\rho,1} - u_{\rho,2}$ **[mm]**	$u_{\rho,3} - u_{\rho,4}$ **[mm]**
Aluminium 6082-T6	-0.063	-0.005	0.002
Aluminium Bronze 954	-0.050	-0.003	0.002
Titanium Alloy	-0.048	-0.002	0.002
AISI 316L	-0.035	-0.001	0.001

Table 3.7: Other quantities related to the points of Fig. 3.16 needed to check the circularity.

The azimuthal (circumferential) displacements u_θ consist in a rotation of the magnet around its axis. This rotation introduces skew dipole components, i.e unwanted field components (Appendix A explains the magnetic field components), so it is important to keep azimuthal deformations low to avoid rotations much bigger than 1 mrad. Approximately, this figure translates into requiring azimuthal displacements below 0.1 mm.
The results of Table 3.8 show that azimuthal displacements are well below the limit of 0.1 mm for all the cases.

Formers' material	**Maximum magnitude of azimuthal displacements u_θ [mm]**
Aluminium 6082-T6	0.028
Aluminium Bronze 954	0.022
Titanium Alloy	0.021
AISI 316L	0.015

Table 3.8: Maximum magnitude of azimuthal displacement in case of different formers materials.

3.2.5. Stresses

The stresses in the former show extremely high peaks (mainly in the Von Mises and minimum principal stresses), but these peaks are highly localized and positioned on the XZ plane where

the mesh's nodes are constrained not to move along the y-axis. Moreover, the peaks become higher and higher refining the mesh, but increasing the number of nodes in the two formers of the periodic slice (Fig. 3.12) of factors 2 and 7 gives a small change in the average Von Mises stress of the formers (Table 3.9). For these reasons, the stress peaks are not real but consist in numerical singularities.

Sum of the nodes in the two formers	**Ratio between the number of nodes of the current row and the previous row [-]**	**Average Von Mises stress of the two formers [MPa]**	**Difference of average Von Mises stress of the two formers respect previous row [%]**
3892	-	141.89	-
8017	2.05	145.27	+2.4
57525	7.17	156.03	+7.4

Table 3.9: Mesh sensitivity analysis for the two formers made of aluminium bronze 954 (the main candidate for the formers' material).

For the evaluation of the safety factor (Table 3.10) the behaviour of the materials was assumed symmetric with respect to traction and compression. The stress compared to the yield limit was the maximum stress in magnitude among Von Mises, maximum principal and minimum principal stresses. The minimum required safety factor is 2 since this is a preliminary design. Additionally, the numerical singularities were neglected to give a more realistic evaluation of the safety factor.

Formers' Material	**Highest Von Mises Stress [MPa]**	**Highest Maximum Principal Stress [MPa]**	**Lowest Minimum Principal Stress [MPa]**	**Safety Factor [-]**
Aluminium 6082-T6	283	118	-275	1.59
Aluminium Bronze 954	475	192	-440	1.34
Titanium Alloy	758	293	-800	2.13
AISI 316L	700	342	-720	0.84

Table 3.10: Maximum stresses and safety factors of the formers for the different formers' materials.

The values of Table 3.10 show that the peaks of stresses are mainly due to compression. Moreover, just AISI 316L achieves yielding, but the safety factor remains below 2 for all the materials except for titanium. So, stresses are critical using the first evaluated design. It was observed that AISI 316L is less stressed than titanium despite its higher Young's modulus, but this is due to the interaction with the coil modelled as a homogenized orthotropic material. In fact, repeating the simulations modelling the coil as dummy isotropic material with extremely low

Young's modulus (1 MPa), AISI 316L results more stressed than titanium.

The stresses in the conductors show localized peaks of stress, still caused by numerical singularities. In fact, the peaks are in the same position as in the formers. Moreover, performing a mesh sensitivity study (Table 3.11), the average Von Mises stress in the conductors changes by just 2% increasing the number of nodes of factor 7.

Sum of the nodes in the conductors	**Ratio between the number of nodes of the current row and the previous row [-]**	**Average Von Mises stress in the conductors [MPa]**	**Difference of average Von Mises stress in the conductors respect previous row [%]**
2666	-	49.52	-
6627	2.48	50.84	+2.7
47907	7.22	51.95	+2.2

Table 3.11: Mesh sensitivity study for the conductors in case of formers made of aluminium bronze 954 (the main candidate for the formers' material).

The behaviour of the conductors is assumed symmetric with respect to traction and compression. The stress compared with the yield limit remains the maximum stress in magnitude among Von Mises, maximum principal and minimum principal stresses. The numerical singularities are neglected to give a more realistic evaluation of the safety factor (Table 3.12).

Formers' Material	**Highest Von Mises Stress [MPa]**	**Highest Maximum Principal Stress [MPa]**	**Lowest Minimum Principal Stress [MPa]**	**Safety Factor [-]**
Aluminium 6082-T6	114	107	-70	2.63
Aluminium Bronze 954	97	160	-15	1.88
Titanium Alloy	100	230	32	1.30
AISI 316L	101	194	10	1.54

Table 3.12: Maximum stresses and safety factors of the conductors in the case of different formers' materials.

Table 3.12 indicates that yielding is not achieved, and the peak of stresses is mainly due to traction. Just one case (formers made of aluminium 6082-T6) reaches a safety factor higher than 2 (the minimum required safety factor), and high traction is shown in the case of titanium former. So, stresses are critical also in the conductors. It is important to remember the conductor of Nb-Ti is modelled as a homogenised orthotropic material. For this reason, the stresses in the conductor are just an indication.

Fig. 3.17 and Fig. 3.18 show some significant pictures of the stresses of the formers and the conductors.

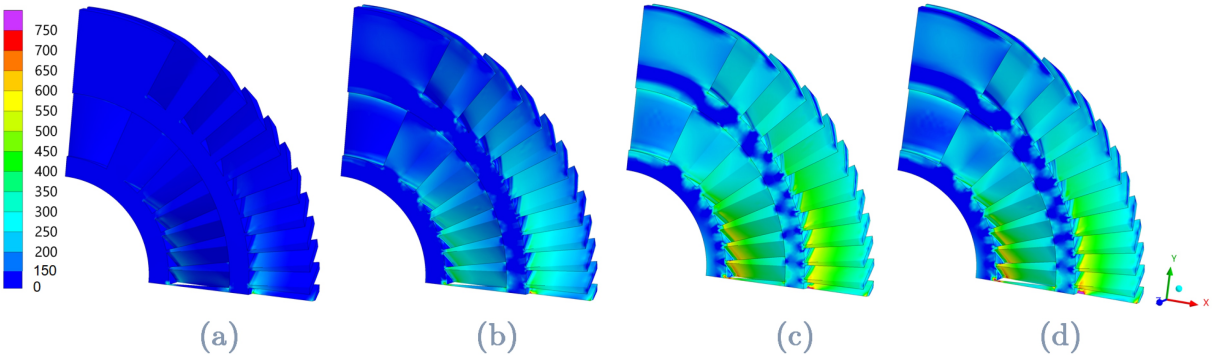

Figure 3.17: Von Mises stresses of the two formers, after the cool down and the energization of the CCT, expressed in MPa for aluminium 6082-T6 (a), aluminium bronze 954 (b), titanium (c) and AISI 316L (d). The highest stresses are where there is electromagnetic forces accumulation. Numerical singularities were removed from the stress scale.

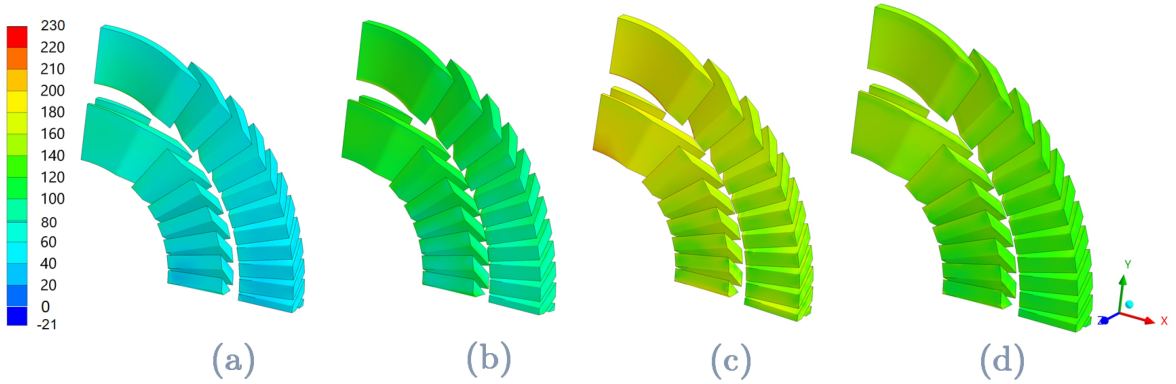

Figure 3.18: Maximum principal stresses of the conductors, after the cool down and the energization of the CCT, expressed in MPa in case of formers made of aluminium 6082-T6 (a), aluminium bronze 954 (b), titanium (c) and AISI 316L (d).

3.3. Take Home Message

This chapter evaluated a first design for the CCT magnet that turned out to be unsuitable. The stresses are too high. Displacements respect the assumed limit, but this may not happen for formers made of plastic materials (much less stiff than metals), which will be introduced in the following chapters due to new calculations on eddy currents, which showed that metals give high losses (Section 4.2). Plastic materials can solve this problem due to their high resistivity. For all these reasons, it is necessary to improve the first evaluated design to reduce stresses and limit the deformations of the CCT.

4 | FEM Simulations of Curved CCT with Iron Yoke

This chapter explains the new mechanical design evaluated for the curved CCT and demonstrates it is much better than the initial one shown in the previous chapter.

Chapter 3 showed that the initial design is unsuitable due to high stresses. Moreover, the initial mechanical structure uses a shell to contain the race track deformation (ovalization of the CCT). The shell requires presses and welding to be assembled, thus increasing the cost of the mechanical structure surrounding the CCT magnet. Additionally, the curvature needed in the case of curved CCT would further increase the cost of the shell. For these reasons, a new mechanical structure was designed for the curved CCT, also considering the presence of iron yoke since the beginning. In the new design, the iron yoke does not simply reduce the magnitude of Lorentz forces. The iron yoke also has a structural role in containing the race track deformation and stresses. For this reason, the iron yoke must be included in the FEM model. Moreover, since the iron yoke limits stresses and deformations, the expensive shell is not needed. It is important to remember that, for mechanical behaviour, small differences are expected in the centre of the magnet (where results are evaluated) between the straight and curved case. The curved CCT analyzed in this chapter has the same geometrical parameters as the straight CCT of Chapter 3. The only difference is the presence of bending radius (1.5 m) in the case of the curved magnet.

4.1. Mechanical Structure

The main components of the mechanical structure surrounding the CCT are shown in Fig. 4.1, Fig. 4.2 and Fig. 4.3. The components that appear in Fig. 4.1, Fig. 4.2 and Fig. 4.3 are just a representation of the assembly's parts. So, some construction details, such as rounds and chamfers, are not present.

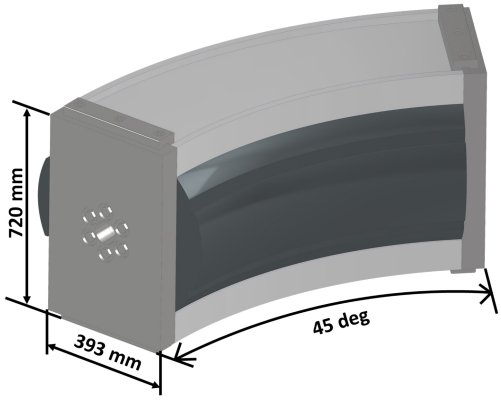

Figure 4.1: Mechanical structure which surrounds the curved CCT magnet.

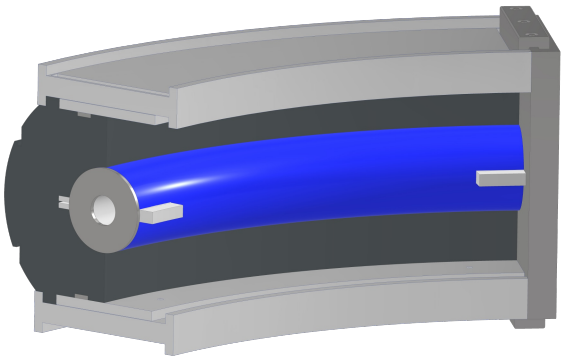

Figure 4.2: Internal view of the mechanical structure.

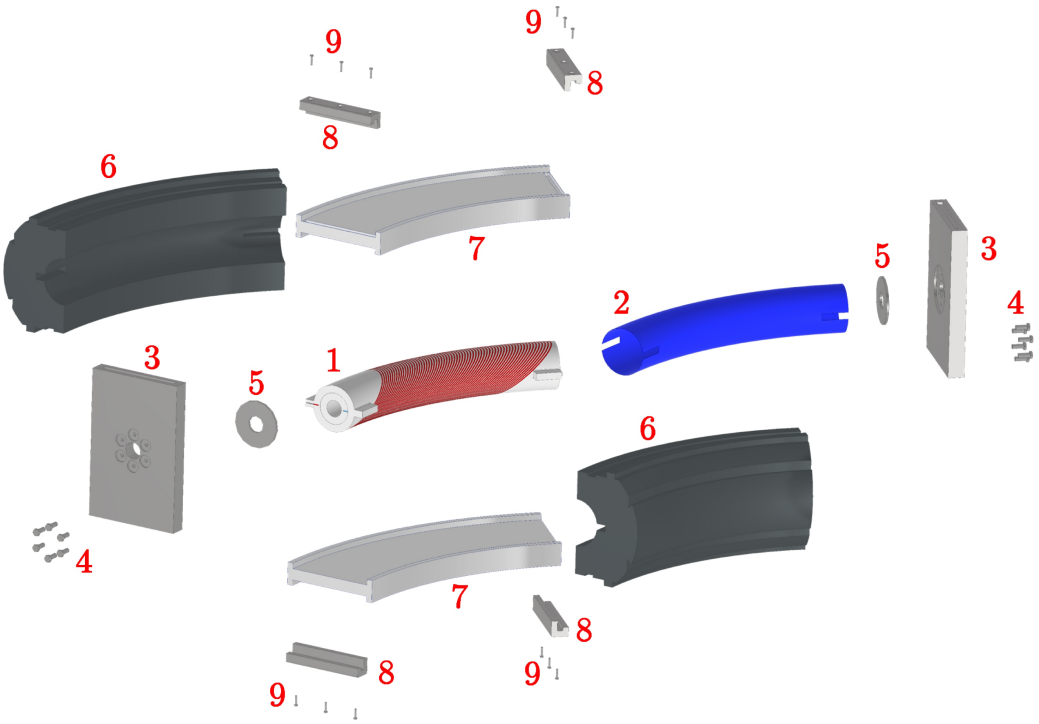

Figure 4.3: Main of components of the mechanical structure which surrounds the CCT.

The components of the mechanical structure (Fig. 4.3) are:

1. CCT magnet. It is possible to see some attachments which are needed to keep the alignment of the magnet.
2. Protection material (0.5 mm thick) made of NEMA (National Electrical Manufacturers Association) G10 which covers the CCT. This thin layer must insulate and protect the conductor.
3. At the extremities of the assembly, there are two end plates (made of AISI 316L) which give rigidity to the structure and contain six screws that press on the CCT extremities.
4. Screws that contrast Lorentz forces in the magnet extremities, which tend to make the curved CCT straight (Appendix C gives a first estimation of this effect).
5. Two small plates, placed at the extremities of the magnet and made of AISI 316L, which must distribute the action of screws uniformly on the CCT. The small plates are attached to the magnet with glue that can fill possible empty spaces between the magnet and the small plates, thus maximizing the distribution of screws forces on the CCT.
6. Iron yoke is divided into two halves that must remain attached to the CCT on the magnet midplane to contain the race track deformation (ovalization of the CCT) given by Lorentz forces (Fig. 4.4) and stresses of the magnet. The two halves are separated by a gap (not constant, opened at room temperature and closed at cold temperature) whose value was optimized to satisfy two ideal conditions:
   (a) At the end of the cool down, the gap must be completely closed, while the CCT and iron yoke must have a distance lower than 0.05 mm on the magnet midplane (Fig. 4.4). This constraint is necessary to maintain a good field quality during the energization of the magnet.
   (b) When the magnet is energized, the Lorentz forces ovalize the CCT and the iron yoke must contain this effect. For this reason, the magnet and iron yoke must be well in touch on the magnet midplane (Fig. 4.4) and the gap between the halves of iron yoke must remain closed. If the gap opens, it means that iron yoke is not containing the race track deformation of the CCT. Keeping the gap closed perfectly along the whole magnet is really difficult, so a small aperture is acceptable.

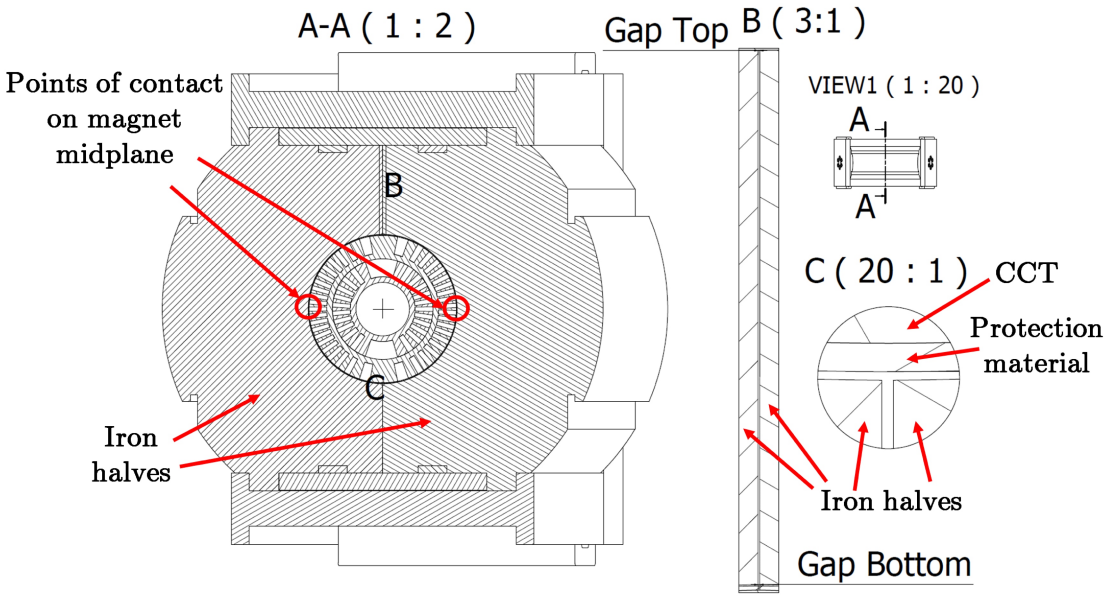

Figure 4.4: Cross-section of the mechanical structure which surrounds the CCT. In detail B it is possible to see the gap between the two parts of the iron yoke, which is not constant (at the bottom is smaller than at the top). In detail C is possible to see the small space between the iron yoke and the CCT due to 1 mm distance between the centres of iron yoke halves and CCT. This distance is needed to have contact between CCT and iron yoke just on the magnet midplane (red circles in the picture). The figure shows additional components with respect to Fig. 4.3, which are needed for the assembly process (Section 6.3).

The larger the gap between iron yoke halves at room temperature, the higher the contact force between the CCT and iron when the magnet is energized, but the risk of not closing the gap between the two parts of the iron yoke at cryogenic temperature is higher. So, the value of the gap between iron halves is a trade-off between the contact of the iron yoke and CCT on magnet midplane and the contact between iron yoke halves.
To find the optimal value of the gap between the iron yoke halves, different simulations were carried out. A full 3D simulation of the whole assembly has a high computational cost due to many components and nonlinear (frictional) contacts. For this reason, 2D simulations were done first to obtain a quick indication of the proper value of the gap. Then, full 3D simulations were carried out to obtain better precision. Table 4.1 shows the optimal values of the gap found for different formers materials: the higher the contraction of the material, the higher the gap.

Formers' material	Gap Top [mm]	Gap Bottom [mm]
PEEK GF 30	0.44	0.40
NEMA G11	0.40	0.36
Aluminium 6082-T6	0.54	0.50
Aluminium Bronze 954	0.48	0.44

Table 4.1: Gap between the halves of the iron yoke in case of the different formers' materials. Details on the materials are in Section 4.2.

7. Two clamps are present at the top and bottom of the structure. All the possible materials for the formers contract more than the iron yoke, leading to detachment between the iron yoke and CCT during cool down. If this happens, the iron yoke cannot contain the deformation of the CCT. So, to avoid this phenomenon, the material of the clamps must have thermal contraction higher or equal to the one of CCT formers. The material selected for the clamps is aluminium 6082-T6 due to its high thermal contraction.
8. Four joints with 'c' shape (made of AISI 316L) connect the endplates to the rest of the structure.
9. Screws which fix the 'c' joints to the end plates.

4.2. Materials

The investigated materials for the CCT's formers changed with respect to Chapter 3. Titanium alloy and AISI 316L were not considered for the moment, since aluminium 6082-T6 and aluminium bronze 954 are cheaper and easier to machine than titanium and AISI 316L. Moreover, the first calculations on eddy current losses in the former showed that metals give high losses. The magnetic field is not present just in the aperture of the CCT but also in the former. When the magnet is energized, the field varies in time and generates eddy currents in conductive former producing heat that can induce a transition of the superconductor or, at minimum, reduce the temperature margin. For this reason, two thermoplastic materials were simulated due to their high resistivity which eliminates the eddy current losses: NEMA (National Electrical Manufacture Association) G11 and PEEK GF 30 (polyether-ether-ketone reinforced with 30% of glass fibres), which is the main candidate material. The presence of glass fibres is mandatory since pure PEEK has such a high thermal contraction that keeping iron yoke attached to CCT would be extremely difficult [16]. The glass fibres of PEEK are short and oriented in all directions, so the behaviour of PEEK GF 30 is almost isotropic. NEMA G11 is anisotropic but was modelled as isotropic for simplicity. Table 4.2 shows the properties of NEMA G11 and PEEK GF 30. Properties of aluminium 6082-T6 and aluminium bronze 954 are in Table 3.2.

Material	**Temperature T [K]**	**Young's Modulus E [GPa]**	**Poisson's Ratio ν [-]**	**Ultimate Tensile Strength UTS [MPa]**	**Coefficient of Thermal Contraction $\alpha_{293K-4.2K}$ [1\K]**	**Reference**
PEEK GF 30	293	11.6	0.39	200 (20 K)	10.38e-6	[16] [33]
	4.2	18.1	0.39			
NEMA G11	293	14	0.3	553 (4 K)	8.65e-6	[22] [20]
	4.2	22	0.3			

Table 4.2: Mechanical properties of PEEK GF 30 and NEMA G11.

The conductor cable of Nb-Ti and the surrounding resin were modelled as a single homogenized orthotropic material [24] as in Section 3.2.1. The mechanical properties of the homogenized orthotropic material are in Table 3.3 and 3.4.

4.3. Constraints and Loads

The structure to suspend the magnet into its cryostat is still under design. For this reason, some constraints were applied to simulate the simple case where the magnet lays on the ground:

1. The faces at the bottom of the assembly (Fig. 4.5) cannot move along the z-axis.

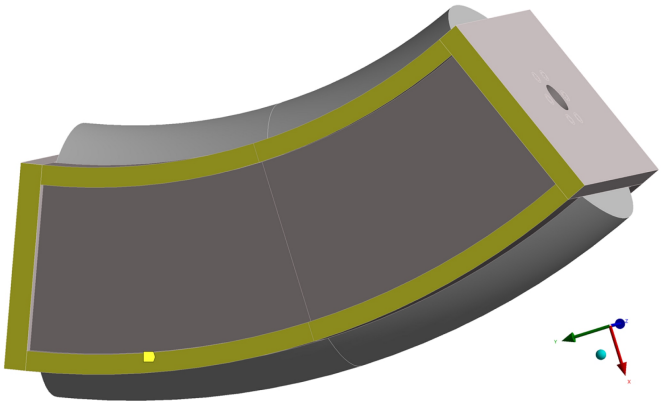

Figure 4.5: Faces (yellow) constraint not to move along the z-axis (blue arrow).

2. The edges generated by the interception of the XZ plane (which passes by the centre of the structure) with iron, aluminium clamps and CCT were constrained not to move along the y-axis (Fig. 4.6). This constraint is necessary because numerical errors give a resultant of Lorentz forces along the y-axis slightly different from 0. This can cause unwanted rotations of the assembly.

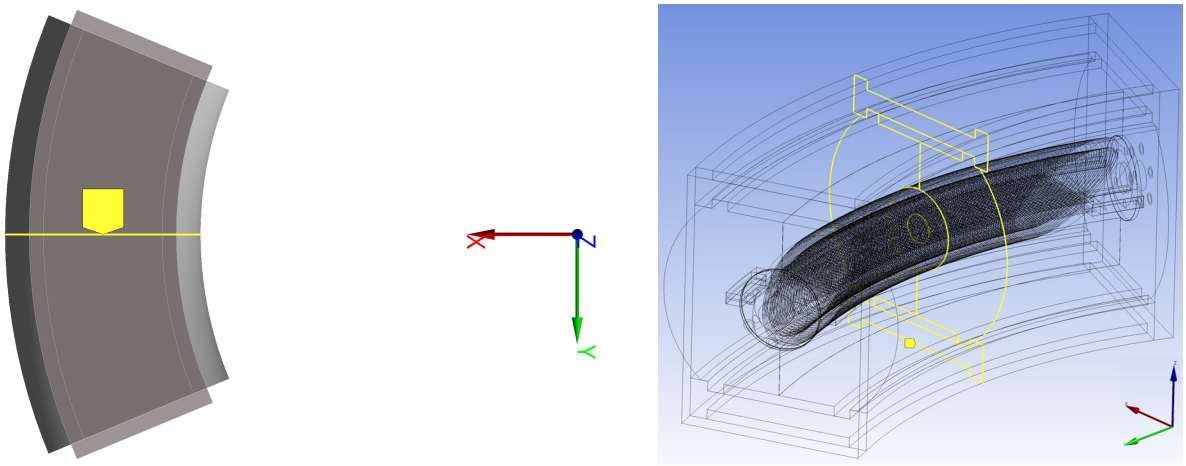

(a) (b)

Figure 4.6: Edges (yellow) constraint not to move along y-axis (green arrow).

3. One point at the mid of the assembly (Fig. 4.7) was constrained not to move along the x-axis, since iron's magnetisation causes electromagnetic force not null along the x-axis.

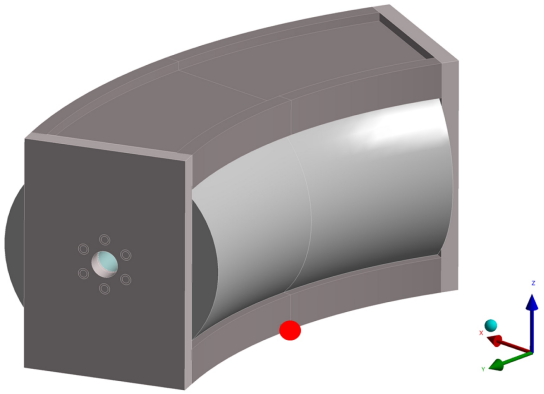

Figure 4.7: Point (red dot) constraint not to move along the x-axis (red arrow).

The simulation is composed of three subsequent steps where the following loads are applied:

1. Pretension of screws.
2. Cool down from 293 K to 4.2 K (needed to achieve the superconducting state of Nb-Ti).
3. Energization.

4.4. Submodelling

The submodelling technique (explained in Section 3.2.3) was applied to see the results of the simulations more in detail. Lorentz force densities tend to make the CCT straight. Despite this, the magnet's structure is very rigid and maintains the curved shape of the CCT and its circular periodicity. The applied loads are periodic too, so it is interesting to evaluate the results in the keystone periodic slice at the magnet's centre using the submodelling method (Fig. 4.8) [5].

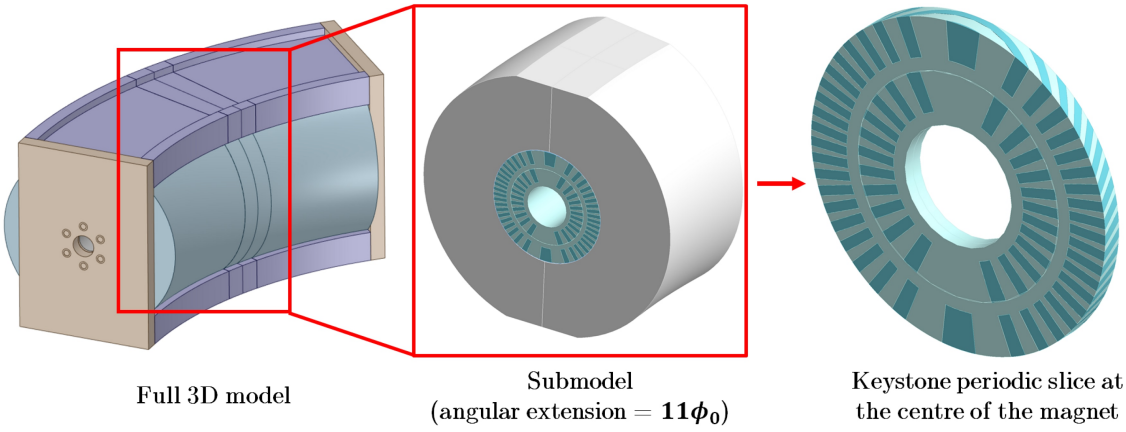

Figure 4.8: Submodelling applied to the curved CCT. The optimal extension of the submodel was found to be 11 times the angular pitch of the CCT's winding path ϕ_0 (see Fig. 2.8).

4.5. Stresses

First of all, a mesh sensitivity (Table 4.3 and Table 4.4) study was carried out in the case of formers made of PEEK GF 30 (the main candidate material).

Sum of the nodes in the two formers	Ratio between the number of nodes of the current row and the previous row [-]	Average Von Mises stress of the two formers [MPa]	Difference of average Von Mises stress of the two formers respect previous row [%]
6136	-	20.58	-
8869	1.45	23.33	+13.4
14953	1.69	26.48	+13.5

Table 4.3: Mesh sensitivity analysis for the two formers.

Sum of the nodes in the conductors	Ratio between the number of nodes of the current row and the previous row [-]	Average Von Mises stress in the conductors [MPa]	Difference of average Von Mises stress in the conductors respect previous row [%]
3124	-	23.74	-
4964	1.59	24.25	+2.2
10828	2.18	27.15	+12.0

Table 4.4: Mesh sensitivity study for the conductors.

Table 4.3 and Table 4.4 show that the average Von Mises stress changes of 13.5% in the formers and 12.0% in the conductors by increasing the number of nodes. These quantities are considered acceptable for the precisions of the results.
The same assumptions as Section 3.2.5 were used to evaluate the safety factor:

- The behaviour of the materials is symmetric with respect to traction and compression.
- The stress compared with yield is the highest in magnitude among Von Mises, maximum principal and minimum principal stresses. The minimum required safety factor is 2.

The stresses of the former (Table 4.5) are mainly due to compression and the safety factors are close to 3 or higher. It is important to observe that the Von Mises stress decreased by 58% in the case of aluminium bronze 954 and 65% in the case of aluminium 6082-T6 with respect to the design of Chapter 3. This is due to the presence of iron yoke that does not simply reduce the current and the magnitude of Lorentz forces. The iron yoke also gives other relevant contributions:

- In the initial design the work of Lorentz forces was distributed on the CCT and an external shell. The iron yoke is much bigger than the shell, so the work is distributed in a wider volume, thus reducing the energy absorbed by the CCT.

- In the design of Chapter 3, the iron yoke is distant from CCT due to the presence of the shell and a small gap. In the new design, the iron yoke is attached to CCT. So, adding the iron yoke, the decrease of current (and magnitude of Lorentz forces) is higher with respect to the one that can be obtained with the initial design.
- If the gap between the halves of the iron yoke is closed, the CCT, iron yoke and aluminium clamps can be considered, approximately, as a system of parallel springs (Fig. 4.9). The iron yoke is much stiffer than CCT. For this reason, the iron yoke reduces the displacement of CCT, the force and the stress acting on CCT.

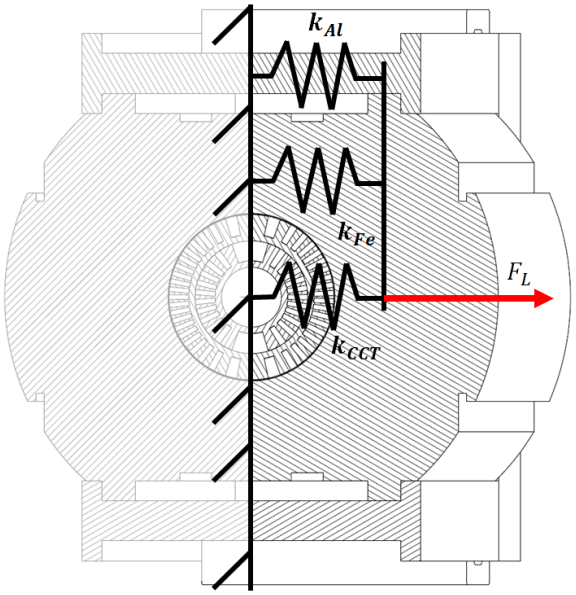

$$F_{CCT} = \frac{F_L}{1 + \frac{k_{Fe} + k_{Al}}{k_{CCT}}}$$

Figure 4.9: Mechanical structure modelled as a system of parallel springs. Each cross-section of the mechanical structure is symmetric. This allows modelling the symmetry axis of the cross-section as an infinitely rigid line. At the same time, the other components are parallel springs subjected to the resultant Lorentz forces on magnet midplane F_L. k indicates the spring stiffness of the CCT, iron yoke and aluminium clamps. Solving the parallel springs system makes it possible to obtain the force F_{CCT}, which acts on the magnet. The expression of F_{CCT} shows that if the CCT is alone (k_{Fe} and k_{Al} are null), the whole force F_L acts on the magnet. Instead, if k_{Fe} and k_{Al} are much bigger than k_{CCT}, the force that acts on the CCT significantly reduces. So, the deformation and stress of the CCT decrease too. It is important to remember that this is a simplified model. The Lorentz forces are distributed inside the CCT, so, in the real structure, even in the case of an infinitely rigid iron yoke surrounding the magnet, part of Lorentz forces act on the CCT.

The stresses in the conductors (Table 4.6) are mainly due to traction and all safety factors respect the limit of 2. Respect the initial design, the maximum stress in the conductors decreased by 14% and 37.5% in the case of formers made of aluminium 6082-T6 and aluminium bronze 954 respectively. It is necessary to remember that stresses in the conductors are an indication, because the coils are modelled as an homogenized orthotropic material.
It is possible to conclude that the new design significantly decreased the stresses in the CCT magnet.

Formers' Material	Highest Von Mises Stress [MPa]	Highest Maximum Principal Stress [MPa]	Lowest Minimum Principal Stress [MPa]	Safety Factor [-]
PEEK GF 30	68	40	-65	2.94
NEMA G11	86	41	-82	6.43
Aluminium 6082-T6	97	98	-87	4.59
Aluminium Bronze 954	196	90	-172	3.26

Table 4.5: Maximum stresses of the formers and safety factors for the different formers' materials.

Formers' Material	Highest Von Mises Stress [MPa]	Highest Maximum Principal Stress [MPa]	Lowest Minimum Principal Stress [MPa]	Safety Factor [-]
PEEK GF 30	102	123	-52	2.43
NEMA G11	114	140	-41	2.14
Aluminium 6082-T6	75	96	-47	3.13
Aluminium Bronze 954	100	70	-84	3

Table 4.6: Maximum stresses of the conductors and safety factors for the different formers' materials.

Fig. 4.10 and Fig. 4.11 shows some relevant pictures of the stresses of the formers and the conductors.

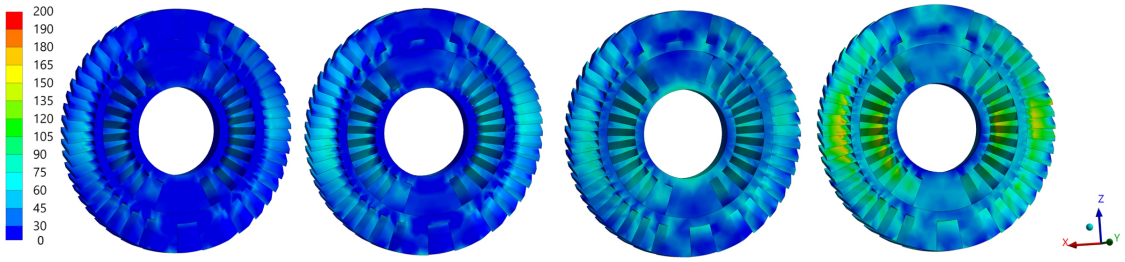

Figure 4.10: Von Mises stresses of the two formers after cool down and energization of the CCT, expressed in MPa, in case of PEEK GF 30 (a), NEMA G11, aluminium 6082-T6 (c) and aluminium bronze 954 (d). The highest stresses are where there is electromagnetic forces accumulation.

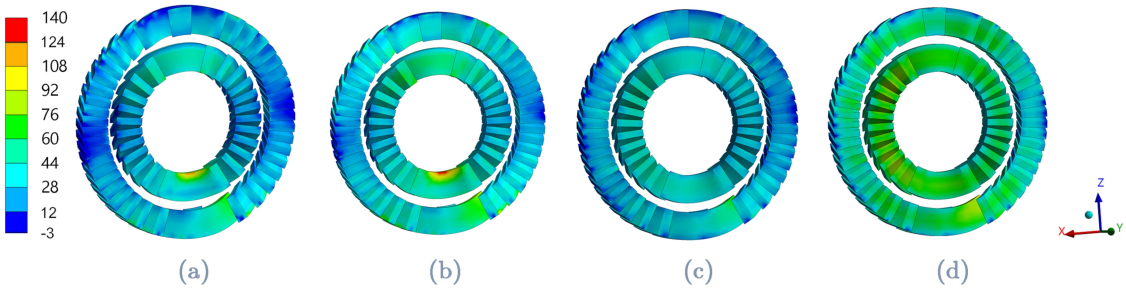

Figure 4.11: Maximum principal stresses of the conductors after cool down and energization of the CCT, expressed in MPa, in case of formers made of PEEK GF 30 (a), NEMA G11 (b), aluminium 6082-T6 (c) and aluminium bronze 954 (d).

4.6. Former's Displacements

As explained in Section 3.2.4, it is essential to evaluate radial and azimuthal (circumferential) displacements due to Lorentz forces only (Fig. 4.12) with respect to the magnet's axis, because they affect the magnet's shape and the magnetic field quality. The same quantities as Section 3.2.4 are analysed (Table 4.7, Table 4.8, Table 4.9 and Table 4.10) to assess the change of shape of the CCT. All the quantities of interest must be lower than 0.1 mm as in Section 3.2.4.

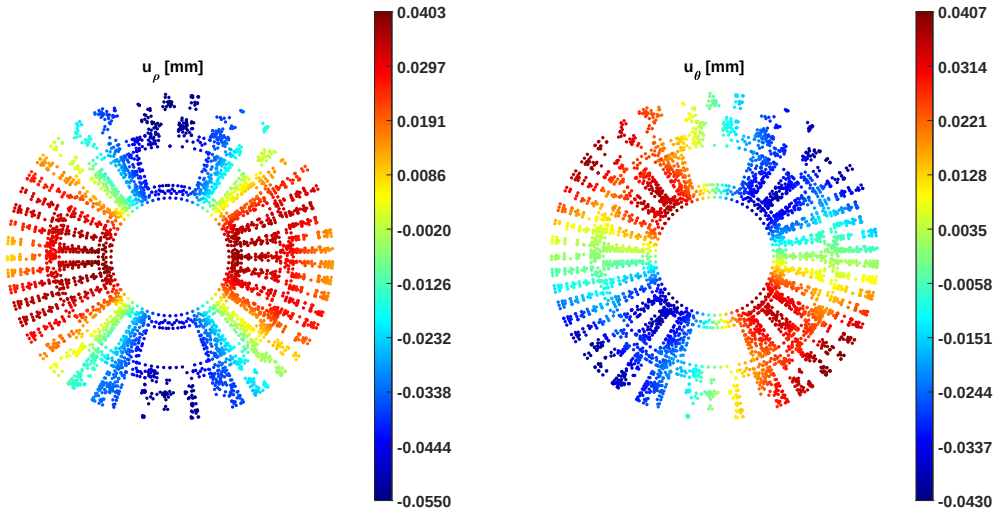

Figure 4.12: Radial (u_ρ) and azimuthal (u_θ) displacements, expressed in mm, of the formers made of PEEK GF 30.

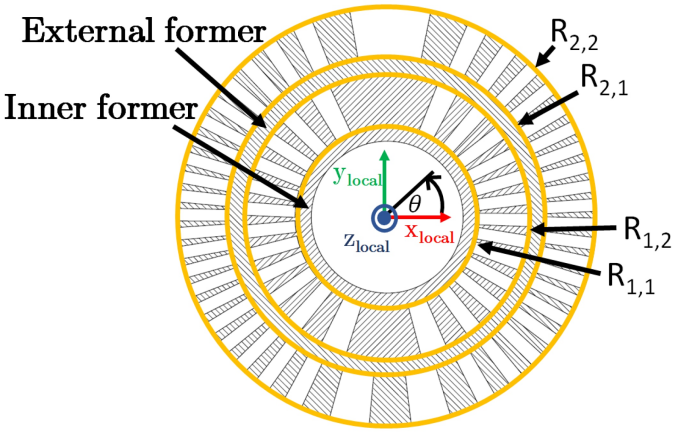

Figure 4.13: Radii where the difference of radial displacement u_ρ was evaluated. At the centre, there is the local reference system whose origin coincides with the magnet's axis.

Formers' material	$\Delta u_\rho^{R1,1}$ [mm]	$\Delta u_\rho^{R1,2}$ [mm]	$\Delta u_\rho^{R2,1}$ [mm]	$\Delta u_\rho^{R2,2}$ [mm]
PEEK GF 30	0.089	0.086	0.085	0.098
NEMA G11	0.080	0.081	0.075	0.084
Aluminium 6082-T6	0.057	0.055	0.055	0.054
Aluminium Bronze 954L	0.032	0.030	0.030	0.036

Table 4.7: Maximum difference of radial displacement Δu_ρ for the points which lay on the same radius $R_{i,j}$ of Fig. 4.13.

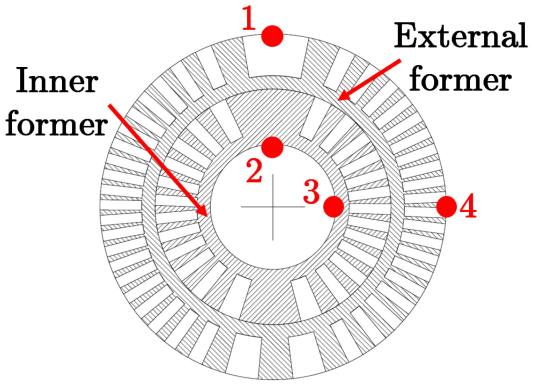

Figure 4.14: Significant points of the formers to assess the circularity and thickness of the CCT. The displacements distribution (Fig. 4.12) exhibits symmetries that allow considering the significant points in just one quarter of the analyzed cross-section.

Formers' material	$u_{\rho,1}$ [mm]	$u_{\rho,2}$ [mm]	$u_{\rho,3}$ [mm]	$u_{\rho,4}$ [mm]
PEEK GF 30	-0.055	-0.045	0.038	0.002
NEMA G11	-0.047	-0.041	0.037	0.004
Aluminium 6082-T6	-0.027	-0.024	0.031	0.006
Aluminium Bronze 954	-0.017	-0.014	0.017	0.006

Table 4.8: Radial displacements $u_{\rho,i}$ of the significant points of Fig. 4.14.

Formers' material	$u_{\rho,2} - u_{\rho,3}$ [mm]	$u_{\rho,1} - u_{\rho,2}$ [mm]	$u_{\rho,3} - u_{\rho,4}$ [mm]
PEEK GF 30	-0.083	-0.010	0.018
NEMA G11	-0.078	-0.060	0.033
Aluminium 6082-T6	-0.055	-0.030	0.025
Aluminium Bronze 954L	-0.031	-0.030	0.011

Table 4.9: Other quantities needed to check the circularity and thickness of the magnet using the data in Table 4.8. $u_{\rho,2} - u_{\rho,3}$ must be low, otherwise the CCT is elliptical and not circular. $(u_{\rho,1} - u_{\rho,2})$ and $(u_{\rho,3} - u_{\rho,4})$ must be similar otherwise the thickness of CCT changes too much.

Formers' material	Maximum magnitude of azimuthal displacements u_θ [mm]
PEEK GF 30	0.043
NEMA G11	0.039
Aluminium 6082-T6	0.024
Aluminium Bronze 954	0.015

Table 4.10: Maximum magnitude of azimuthal displacement in case of different formers materials.

All the quantities of interest remain below the limit of 0.1 mm, but PEEK GF 30 is close to the limit in some cases because of its low Young's modulus. Moreover, in the case of aluminium 6082-T6 and aluminium bronze 954, the displacements are lower than the initial design (Section 3.2.4). It was noticed that $u_{\rho,4}$ does not respect the expected trend with Young's modulus of the formers' materials (the stiffer the material, the lower the displacements), but it is worth noticing that:

- All the values of $u_{\rho,4}$ consist of few microns and the used mesh has a size of millimetres. So, a small mismatch at the level of microns is possible.
- The values of $u_{\rho,4}$ depend on the distance between the CCT and iron yoke at the end of the cool down. This distance is different for each formers' material, so the displacements in point 4 (Fig. 4.14) may have a small mismatch with the expected trend with the material's stiffness.

4.7. Take Home Message

This chapter introduced a new mechanical design for the CCT magnet's structure. The simulations demonstrated that the new design decreased stresses significantly and reduced displacements with respect to the initial design shown in Chapter 3.

5 | FEM Simulations of Straight CCT Magnet with Iron Yoke

This chapter applies the design explained in Section 4.1 to the straight CCT and confirms it is better than the initial one proposed in Chapter 3.

The last simulations of this thesis focused on the straight CCT with iron yoke, considering the mechanical design explained in Section 4.1 and the new geometrical parameters required by the IFAST project. The parameters changed to compare the performance of the CCT with the Cos-Theta magnet investigated in the SIG program [29]. This chapter recalls the mechanical structure surrounding the CCT and describes the simulations carried out and their results.

5.1. Mechanical Structure

The mechanical structure surrounding the CCT (Fig. 5.1, 5.2 and Fig. 5.3) is the same shown in Fig. 4.1, 4.2 and Fig. 4.3. The components that appear in Fig. 5.1, 5.2 and Fig. 5.3 are not the final components for the demonstrators which will be built. So, some construction details, such as rounds and chamfers, are not present. The initial design for straight CCT (shown in Chapter 3) was abandoned since it causes too high stresses and requires a shell that needs presses and welding to be assembled. Moreover, the screws adopted in the new design allow contrasting the elongation of the magnet given by Lorentz forces. In Table 5.1 the optimal values of the gap (Fig. 5.4) between the halves of the iron yoke are reported for different formers material.

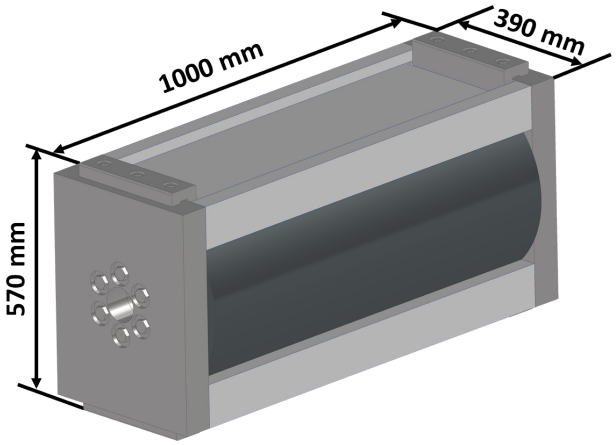

Figure 5.1: Mechanical structure that surrounds the straight CCT magnet.

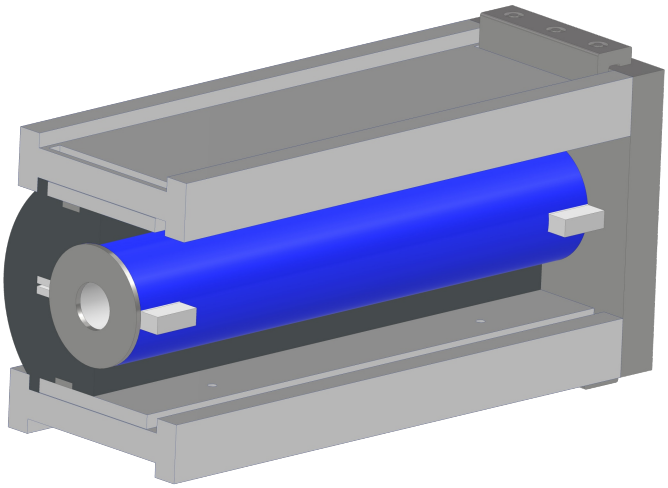

Figure 5.2: Internal view of the the mechanical structure.

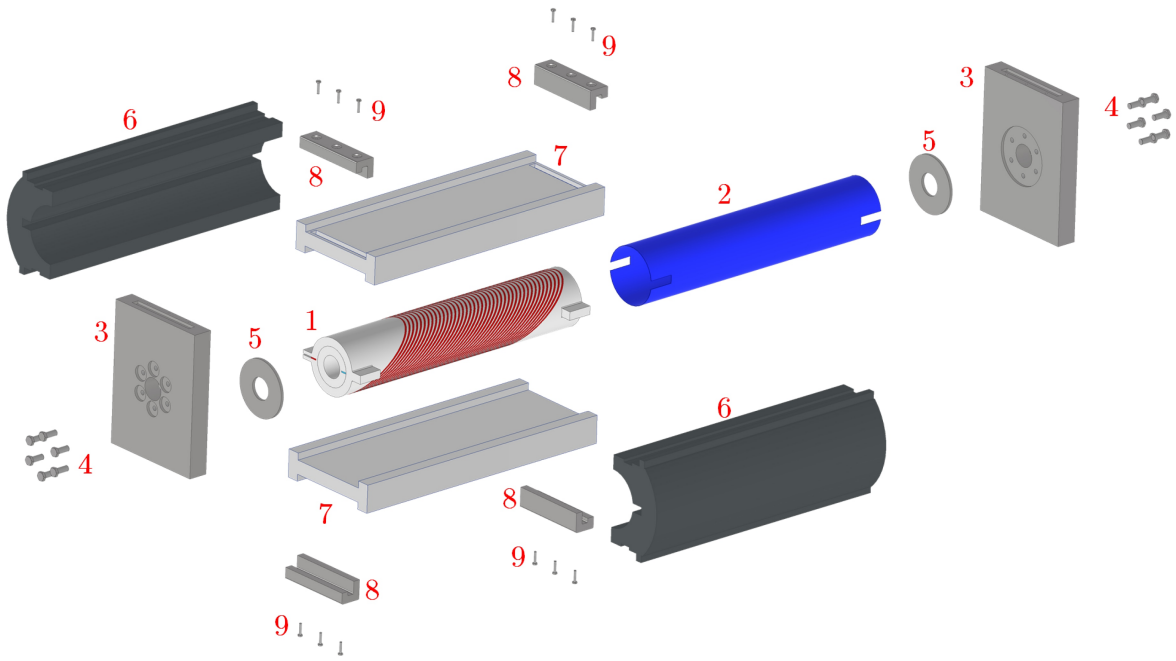

Figure 5.3: Main of components of the mechanical structure which surrounds the straight CCT.

The main components of the mechanical structure (Fig. 5.3) are:

1. CCT magnet.
2. Protection material made of NEMA G10.
3. End plates made of AISI 316L.
4. Screws.
5. Small plates made of AISI 316L.
6. Iron yoke divided into two halves for the same reasons as the curved CCT.

7. Clamps made of aluminium 6082-T6.
8. Joints with 'c' shape made of AISI 316L.
9. Screws which fix the 'c' shape joints to the end plates.

Formers' material	Gap Top [mm]	Gap Bottom [mm]
PEEK GF 30	0.40	0.38
NEMA G11	0.38	0.36
Aluminium 6082-T6	0.44	0.41
Aluminium Bronze 954	0.42	0.40

Table 5.1: Gap between the halves of iron yoke in case of the different formers' materials. The gap is not constant. It is bigger at the top than at the bottom (Fig. 5.4).

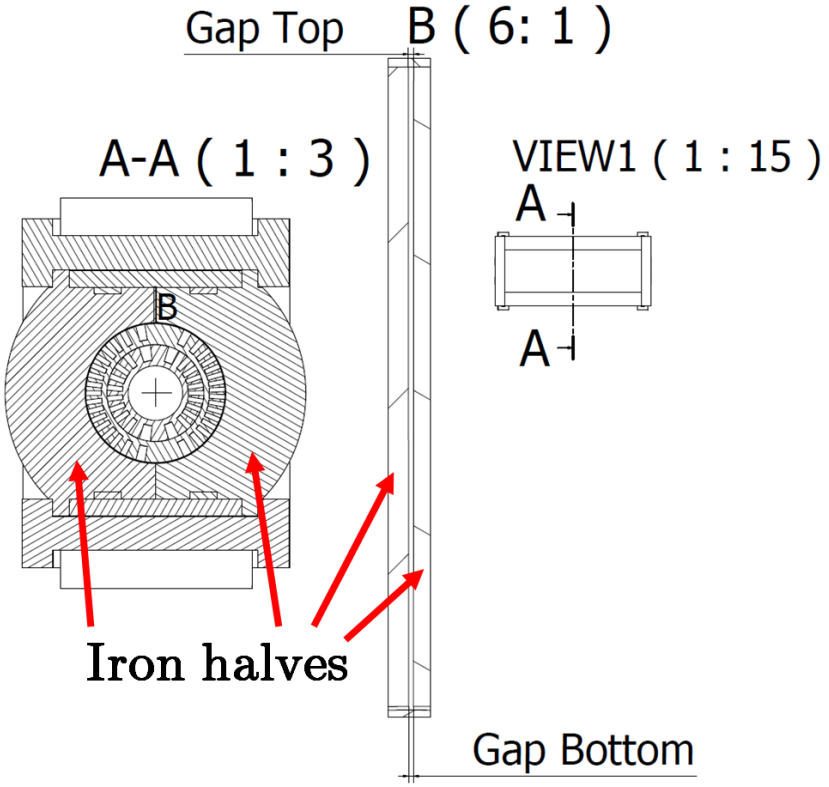

Figure 5.4: Gap between the halves of the iron yoke

Table 5.2 shows the new geometrical parameters of the CCT:

Parameter	Ropes configuration
Bore diameter inner former	80 mm
Spar	8 mm
Groove height	22.8 mm
Groove width	5.7 mm
Outer diameter external layer	203.2 mm
Minimun ribs thickness	0.8 mm
Axial pitch	16.61 mm
Number of turns	42
Central magnetic field	4 T
Gradient for quadrupolar field	5 T/m
Current per cable	1.380 kA
Groove current	22,080 A

Table 5.2: Main CCT design parameters.

5.2. Mechanical Simulations Constraints, Materials and Loads

The CCT was divided into four quadrants (Fig. 5.5) along the longitudinal direction to evaluate the Lorentz forces' symmetries with respect to the XZ and YZ planes (Table 5.3).

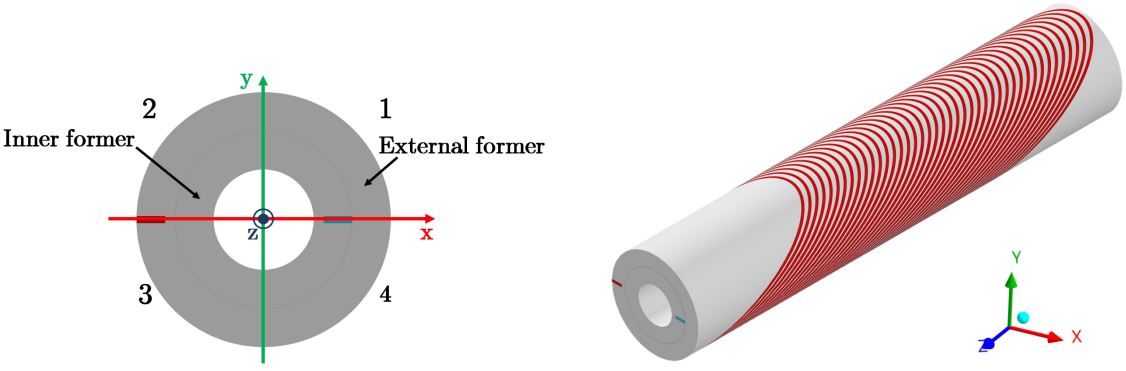

(a) (b)

Figure 5.5: CCT quadrant division.

Forces	Quadrant 1	Quadrant 2	Quadrant 3	Quadrant 4
F_x [N]	4.69e5	-4.45e5	-4.45e5	4.69e5
F_y [N]	-1.25e5	-75,639	75,637	1.25e5
F_z [N]	-40,763	-31,331	31,328	40,762

Table 5.3: Lorentz forces in the four quadrants of Fig. 5.5.

The forces are well symmetric with respect to the XZ plane. Forces are symmetric compared to the YZ plane except for F_x, however the difference is small, just about 5%. So, the model was considered symmetric compared to YZ plane too. The discrepancy of F_x with respect to the YZ plane is caused by the different magnetization of iron compared to the YZ plane. The magnetization generates a different interaction with the coil with respect to the YZ plane and a resultant of Lorentz forces not null. The symmetry of electromagnetic forces allows simulating just one quarter of the magnet (Fig. 5.6) as as in Chapter 3, imposing two boundary conditions on the XZ and YZ planes: the displacement along x-axis of the faces on the YZ plane is null (Fig. 5.7), while the faces on XZ plane cannot move along y-axis (Fig. 5.8).

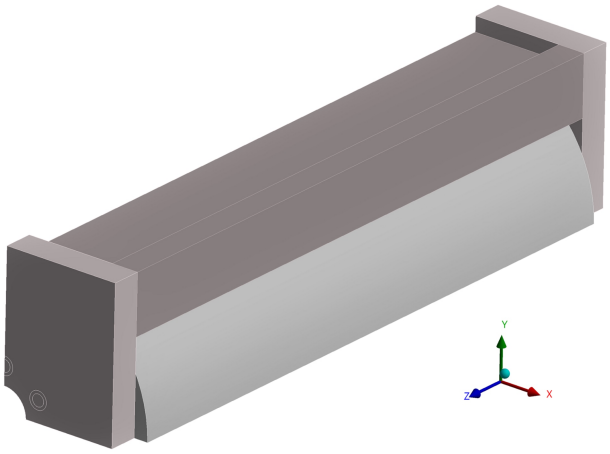

Figure 5.6: ANSYS model of one quarter of the mechanical structure surrounding the CCT magnet.

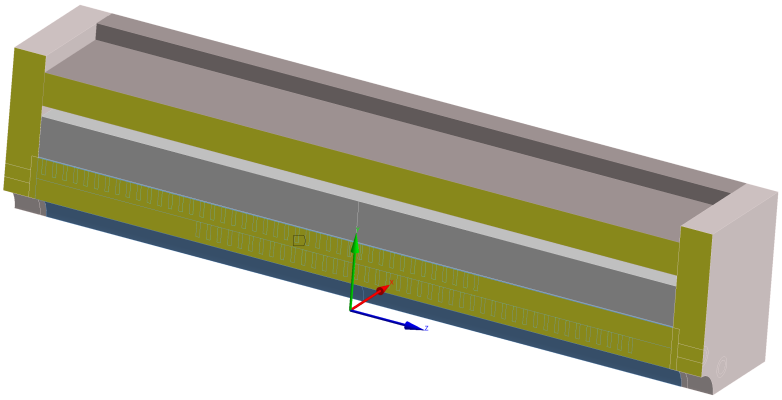

Figure 5.7: The yellow faces lay on the YZ plane and cannot move along x-axis (red arrow).

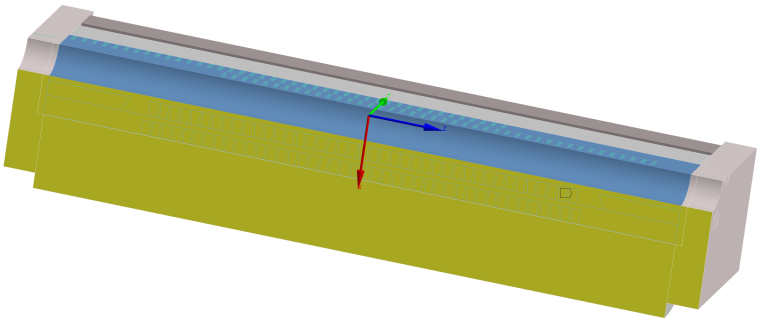

Figure 5.8: The yellow faces lay on the XZ plane and cannot move along y-axis (green arrow).

One last constraint was applied to block the movement along the longitudinal direction (Fig. 5.9).

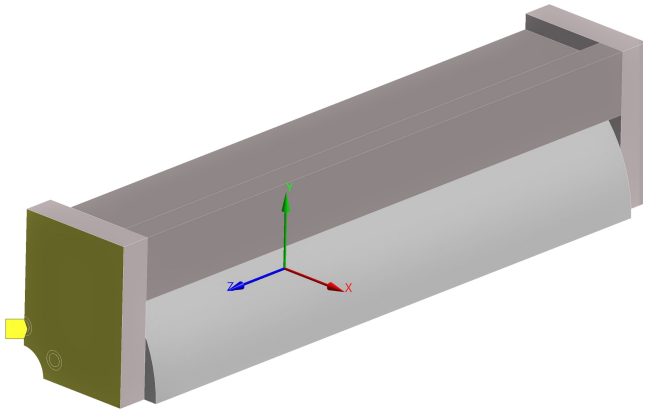

Figure 5.9: The yellow faces at one extremity of the magnet cannot move along z-axis (blue arrow).

A fixed thin bar (Fig. 5.10) was added to simulate the second half of the iron yoke which gets in touch with the first one.

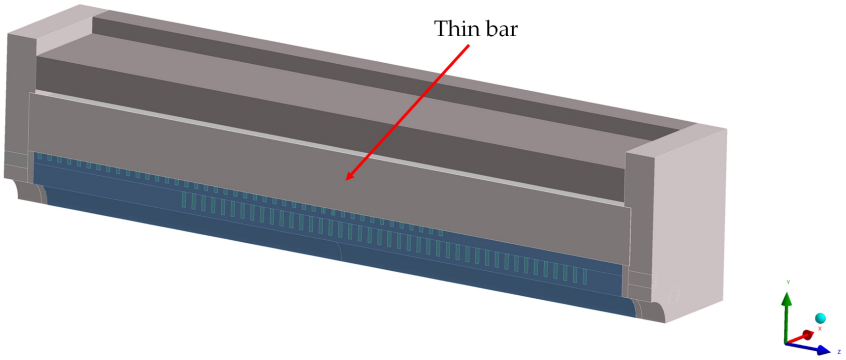

Figure 5.10: Thin bar to simulate the contact between the two halves of the iron yoke.

The materials simulated for the formers are the same as in Chapter 4. The properties of these materials are in Table 3.2 and Table 4.2. The conductor cable of Nb-Ti and the surrounding resin were still modelled as a single homogenized orthotropic material [24] (the mechanical properties of the homogenized orthotropic material are in Table 3.3 and Table 3.4).

The simulation is composed of three subsequent steps where the following loads are applied:

- Pretension of screws.
- Cool down from 293 K to 4.2 K (needed to achieve the superconducting state of Nb-Ti).
- Energization.

5.3. Stresses

The evaluation of the stresses started with the mesh sensitivity analysis in the case of formers made of PEEK GF 30 (the main candidate). The results of this analysis (Table 5.4 and Table 5.5) show that increasing the number of nodes, the increase of average Von Mises stress is just around 1% in the formers and 3% in the conductors. For this reason, the sudmodelling method was not applied. Moreover, as in Section 3.2.5, there are some numerical singularities on the XZ plane where the mesh's nodes are constrained not to move along the y-axis.

Sum of the nodes in the two formers	**Ratio between the number of nodes of the current row and the previous row [-]**	**Average Von Mises stress of the two formers [MPa]**	**Difference of average Von Mises stress of the two formers respect previous row [%]**
2171	-	25.84	-
2802	1.29	26.17	+1.28
4490	1.60	26.46	+1.11

Table 5.4: Mesh sensitivity analysis for the two formers made of PEEK GF 30.

Sum of the nodes in the conductors	**Ratio between the number of nodes of the current row and the previous row [-]**	**Average Von Mises stress in the conductors [MPa]**	**Difference of average Von Mises stress in the conductors respect previous row [%]**
1288	-	23.01	-
1991	1.55	23.81	+3.48
2401	1.20	24.02	+0.88

Table 5.5: Mesh sensitivity study for the conductors in case of formers made of PEEK GF 30.

For the evaluation of the safety factor (Table 5.6 and Table 5.7) the same assumptions as Section 3.2.5 and Section 4.5 were considered:

- Behaviour of the materials symmetric with respect to traction and compression.
- The stress compared with yield is the highest in magnitude among Von Mises, maximum principal and minimum principal stresses. The minimum required safety factor is 2.

The numerical singularities are still neglected to give a more realistic evaluation of the safety factor.

Formers' Material	Highest Von Mises Stress [MPa]	Highest Maximum Principal Stress [MPa]	Lowest Minimum Principal Stress [MPa]	Safety Factor [-]
PEEK GF 30	69	40	-65	2.90
NEMA G11	88	40	-85	6.28
Aluminium 6082-T6	155	136	-123	2.90
Aluminium Bronze 954	212	71	-217	2.94

Table 5.6: Maximum stresses of the formers and safety factors for the different formers' materials.

Formers' Material	Highest Von Mises Stress [MPa]	Highest Maximum Principal Stress [MPa]	Lowest Minimum Principal Stress [MPa]	Safety Factor [-]
PEEK GF 30	104	122	-51	2.45
NEMA G11	119	140	-49	2.14
Aluminium 6082-T6	92	76	-72	3.26
Aluminium Bronze 954	72	78	-39	3.84

Table 5.7: Maximum stresses of the conductors and safety factors for the different formers' materials.

The stress results (Table 5.6 and Table 5.7) show that the situation has improved with respect to the first straight CCT design explained in Chapter 3. All the safety factors are above 2 and most of them are around 3. So, stresses are below the required limit and not critical. Moreover, the maximum Von Mises stress in the formers decreased by 55% for aluminium bronze 954 and 45% for aluminium 6082-T6. The high reduction of stresses is due to the iron yoke, which gives the same contributions described in Section 4.5. The results confirm that the new design evaluated in this chapter and Chapter 4 is more effective than the initial one.

Fig. 5.11 and Fig. 5.12 show some significant pictures of the stresses of the formers and conductors.

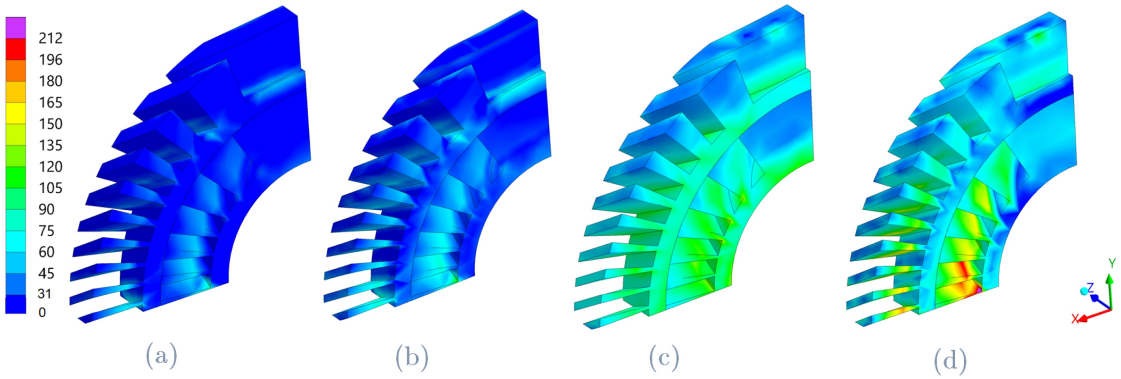

Figure 5.11: Von Mises stresses of the two formers, after the cool down and the energization of the CCT, expressed in MPa for PEEK GF 30 (a), NEMA G11 (b), aluminium 6082-T6 (c) and aluminium bronze 954 (d). Numerical singularities were removed from the stress scale. The highest stresses are where there is electromagnetic forces accumulation.

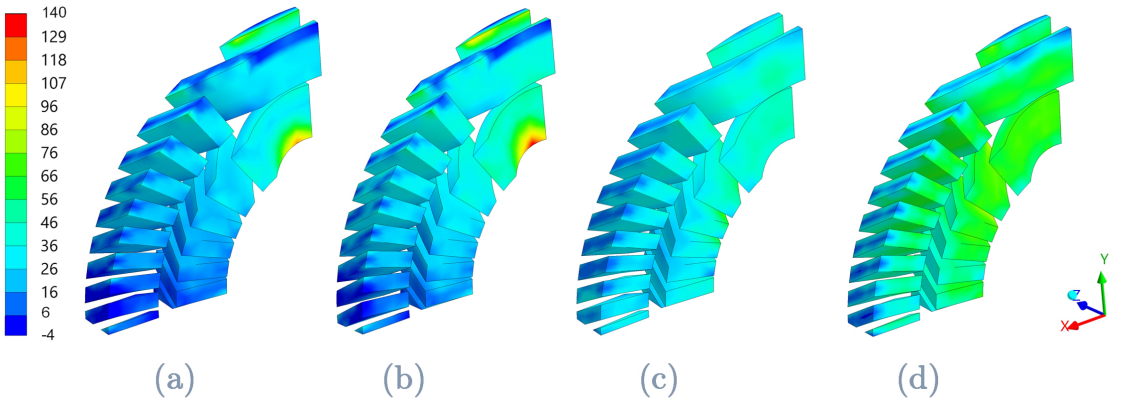

Figure 5.12: Maximum principal stresses of the conductors, after the cool down and the energization of the CCT, expressed in MPa in case of formers made of PEEK GF 30 (a), NEMA G11 (b), aluminium 6082-T6 (c) and aluminium bronze 954 (d).

5.4. Formers' Displacements

As in Chapter 3 and Chapter 4, it is fundamental to evaluate the radial and azimuthal (circumferential) displacements of the formers due to Lorentz forces only (Fig. 5.13), since they affect the magnet's shape and field quality. The same quantities as Section 3.2.4 are analysed (Table 5.8, Table 5.9, Table 5.10 and Table 5.11) to assess the change of shape of the CCT. All the quantities of interest must be lower than 0.1 mm as in Section 3.2.4.

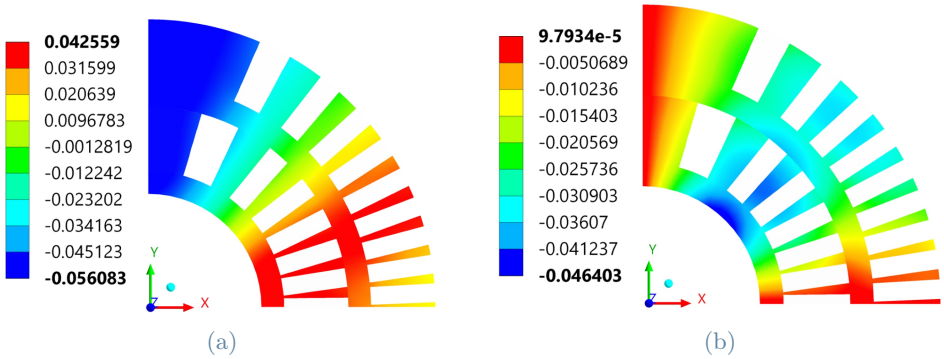

Figure 5.13: Radial (a) and azimuthal (b) displacements of the formers, expressed in mm, in case of formers made of PEEK GF 30.

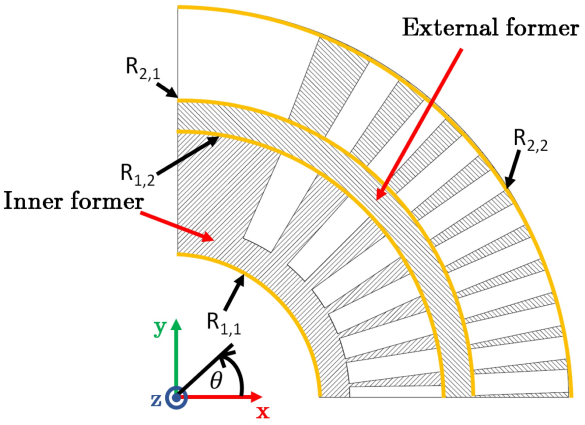

Figure 5.14: Radii where the difference of radial displacement u_ρ is calculated.

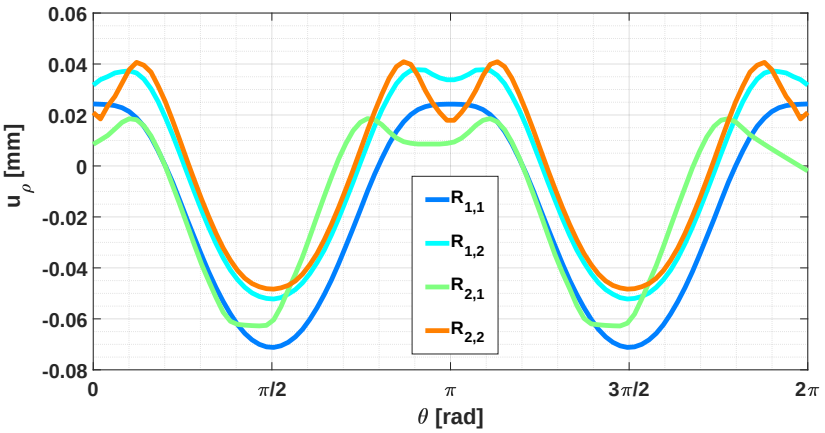

Figure 5.15: Radial displacements u_ρ at the radii of Fig. 5.14 in case formers made of PEEK GF 30.

Formers' material	$\Delta u_\rho^{R1,1}$ [mm]	$\Delta u_\rho^{R1,2}$ [mm]	$\Delta u_\rho^{R2,1}$ [mm]	$\Delta u_\rho^{R2,2}$ [mm]
PEEK GF 30	0.096	0.094	0.082	0.094
NEMA G11	0.084	0.079	0.068	0.078
Aluminium 6082-T6	0.054	0.051	0.045	0.051
Aluminium Bronze 954L	0.044	0.041	0.036	0.049

Table 5.8: Maximum difference of radial displacement Δu_ρ for the points which lay on the same radius $R_{i,j}$ of Fig. 5.14.

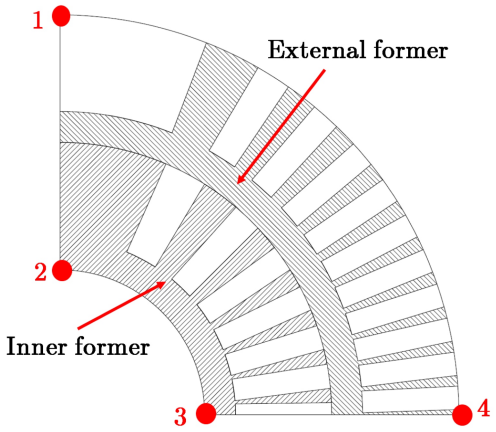

Figure 5.16: Significant points of the formers to assess the circularity and thickness of the CCT.

Formers' material	$u_{\rho,1}$ [mm]	$u_{\rho,2}$ [mm]	$u_{\rho,3}$ [mm]	$u_{\rho,4}$ [mm]
PEEK GF 30	-0.056	-0.050	0.041	0.013
NEMA G11	-0.047	-0.044	0.037	0.012
Aluminium 6082-T6	-0.024	-0.023	0.029	0.009
Aluminium Bronze 954	-0.021	-0.020	0.023	0.004

Table 5.9: Radial displacements $u_{\rho,i}$ of the significant points of Fig. 5.16.

Formers' material	$u_{\rho,2} - u_{\rho,3}$ [mm]	$u_{\rho,1} - u_{\rho,2}$ [mm]	$u_{\rho,3} - u_{\rho,4}$ [mm]
PEEK GF 30	-0.091	-0.006	0.028
NEMA G11	-0.081	-0.003	0.025
Aluminium 6082-T6	-0.052	-0.001	0.020
Aluminium Bronze 954L	-0.043	-0.001	0.019

Table 5.10: Other quantities needed to check the circularity and thickness of the magnet using the data in Table 5.9. $u_{\rho,2} - u_{\rho,3}$ must be low, otherwise the CCT is elliptical and not circular. $(u_{\rho,1} - u_{\rho,2})$ and $(u_{\rho,3} - u_{\rho,4})$ must be similar otherwise the thickness of CCT changes too much.

Formers' material	Maximum magnitude of azimuthal displacements u_θ [mm]
PEEK GF 30	0.046
NEMA G11	0.041
Aluminium 6082-T6	0.023
Aluminium Bronze 954	0.018

Table 5.11: Maximum magnitude of azimuthal displacement in case of different formers materials.

All the quantities of interest remain below the limit of 0.1 mm, but PEEK GF 30 is close to the limit since it has the lowest Young's modulus. Furthermore, in the case of aluminium 6082-T6 and aluminium bronze 954, the displacements are lower than the initial design (Section 3.2.4). Finally, all the displacements respect the expected trend with the Young's modulus of the material: the stiffer the material, the lower the displacements.

5.5. Take Home Message

This chapter analyzed the behaviour of the straight CCT applying the new design described in Section 4.1. In the new design, the stresses and displacements are significantly reduced with respect to the initial design of Chapter 3, resulting in a more stable magnet with better field quality. So, the new design is considerably better than the initial one.

6 | CCT Construction

This chapter describes the manufacturing and assembly processes for CCT magnets.

This chapter explains how the CCT magnet will be made, describing the manufacturing and assembly processes. The following considerations refer to the curved CCT, but also apply to the straight CCT.

6.1. Machining Processes

In the case of metals, the formers of curved CCT for HITRI*plus* will be produced by milling in the CERN workshop with the following sequence [30], [31]:

1. A specialized company bends the initial tube (needed for the generation of the former), since CERN does not have adequate equipment to bend objects of big dimensions. The process starts from a tube and not bulk material since this requires less material to buy and remove.
2. The tube is split into two parts by a saw or a milling tool of small dimensions, which provide higher precision. The division of the tube into two parts allows machining it without limits caused by the bore diameter. In fact, in the case of a tube made by one piece, the smaller the bore diameter of the former, the more difficult the access to the tube's inner area. Splitting the tube solves this problem. The machining of the inner area of the tube is needed to achieve the geometrical tolerances necessary to nest the two formers and insert the vacuum chamber where the particle beam travels.
3. Roughing and finishing by milling of the inner area of the tube (Fig. 6.1):

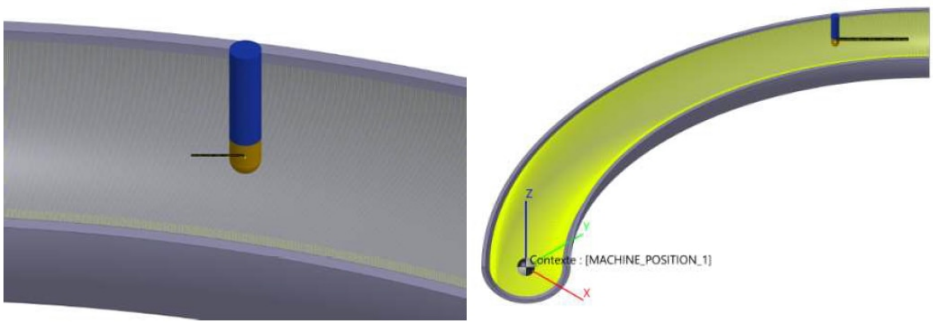

Figure 6.1: One half of the curved tube with the milling tool (blue). The yellow indicates the machined area (Fig. from [30]).

4. Brazing of the two halves of the single tubes.

5. Manufacture of the parts necessary to block the tube during the machining of the groove (Fig. 6.2):

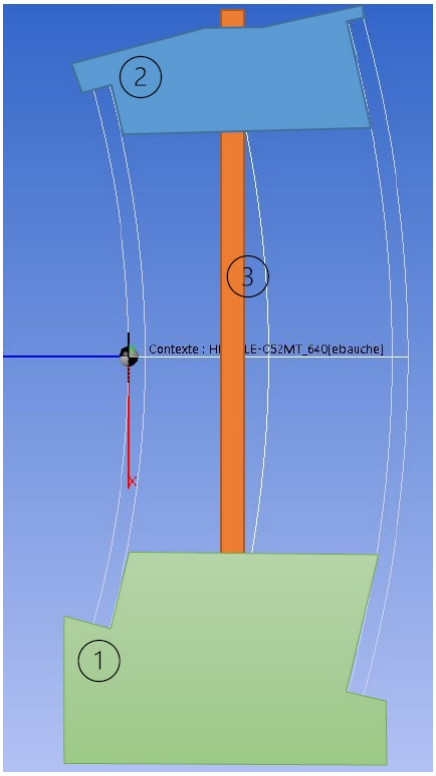

Figure 6.2: Fixing system for the machining of the external part of the tube. The system is composed by the base (1), the adjusted plug (2) and a threaded rod (3) which regulates the distance between the base and the adjusted plug. The white lines indicate the curved tube compressed between the two supports (Fig. from [31]).

6. External diameter roughing/finishing.

7. Milling (roughing and finishing) of the external part of the tube to generate the groove (Fig. 6.3) and the final former. Since the groove is cut after brazing, it is perfectly continuous which is fundamental. If the former is made by more sectors that are machined individually and then assembled, it is possible to have a magnet with a higher bending angle since the limit of the space available inside the machine is solved. Despite this advantage, the many grooves must coincide within a few μm to avoid that assembly sharp discontinuities generate shear stress on the conductor and insulating material. The discontinuity in one of the sectors, almost certainly, caused the breakdown of the first curved CCT manufactured and assembled at LBNL (Lawrence Berkeley National Laboratory) in 2019.

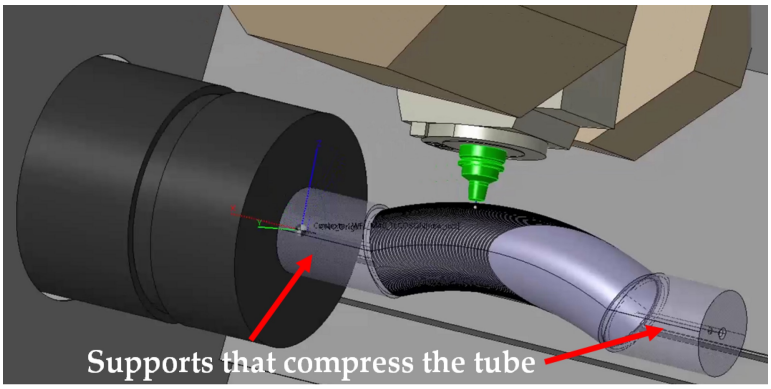

(a)

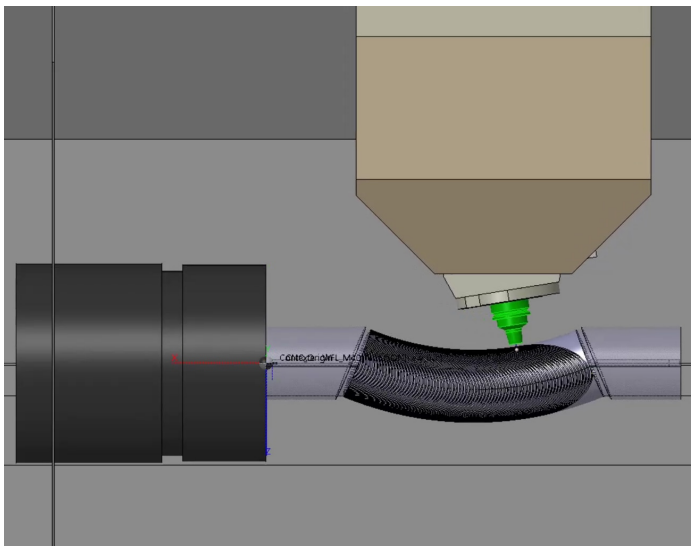

(b)

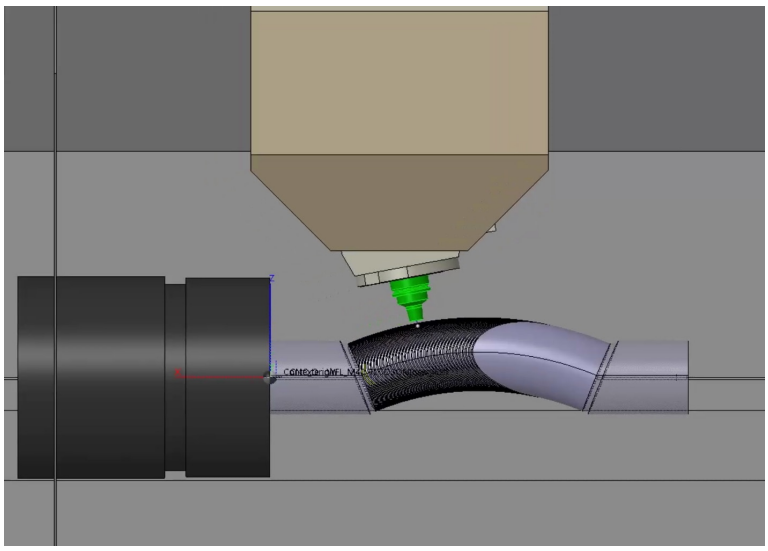

(c)

Figure 6.3: Machining of the groove of the former. The supports of Fig. 6.2 compress the tube and rotate around the x-axis (red arrow). Fig. from [31].

Plastic materials require special machines for machining due to glass fibres. During machining, glass fibres go into bearings that wear quickly, so machines must be equipped with pressurized air so that fibres are blown down and not absorbed. CERN does not have this kind of machines, so in the case of plastic materials, an external company will manufacture the CCT's formers using the following sequence proposed by CERN [25]:

1. In the case of plastic materials, the sequence changes due to the availability of PEEK GF 30, which can be found in plates only. The plates will be assembled to make the whole former, and each plate will be machined to generate the aperture of the former and give the external shape needed for the following step (Fig. 6.4):

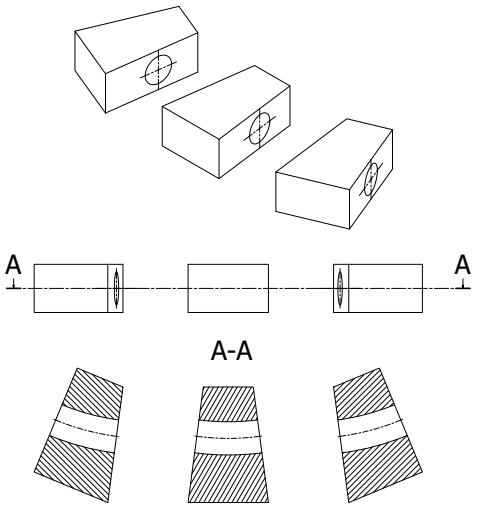

Figure 6.4: Starting plates after the machining. There are three plates in this picture, but this is just an example since the number of plates depends on the plates' dimensions found on the market.

If the thickness of the available plates is not sufficient to cover the outer diameter of the former, each single sector will be made by more plates stacked (Fig. 6.5):

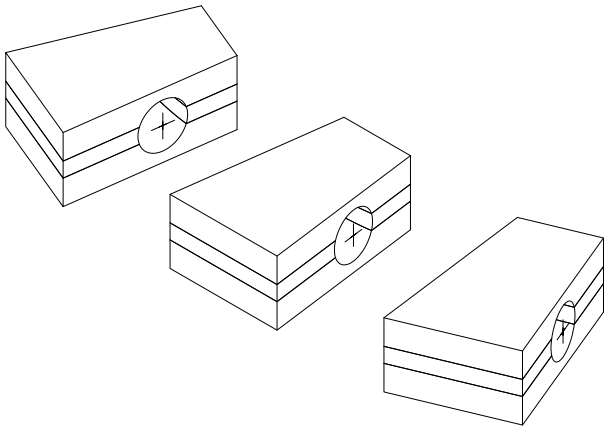

Figure 6.5: Single sectors made by more plates stacked.

2. Gluing of the single parts (Fig. 6.6):

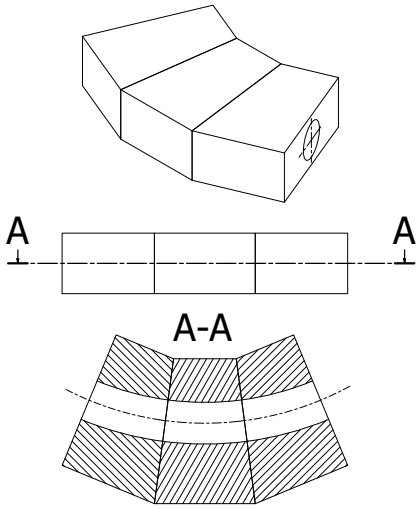

Figure 6.6: Single sectors glued.

3. The glued parts are machined to generate the groove and the final shape of the former (Fig. 6.7). The generation of the groove must be done after gluing the single parts to avoid discontinuities among the grooves.

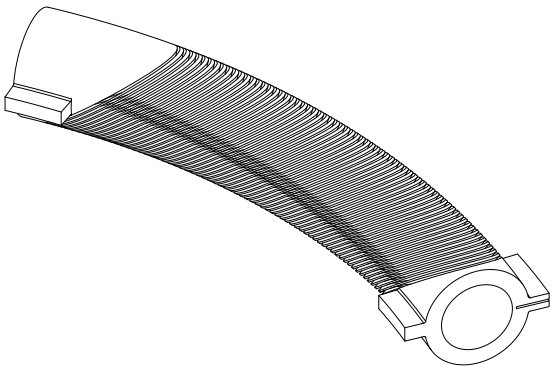

Figure 6.7: Final former.

6.2. Additive Manufacturing

The application of additive manufacturing (AM) to the formers of CCT magnets has been evaluated [1] because of the flexibility of the technology, allowing shapes that might be difficult or impossible to machine.
The following considerations refer to the straight CCT, since the curvature is not a problem because the mandrel is made layer by layer.
In the case of metals, The main candidate for applying AM to CCT is Selective Laser Melting (SLM) technology since it was developed specifically for printing metal alloys, has high resolution (minimal feature size that can be manufactured such as wall thickness or minimum hole size), is widely diffused and available at CERN.

The fastest way to produce CCT would be to place the mandrel horizontally, but in this case, large areas are exposed by the laser, leading to localized heating of the component and deformation. Moreover, the dimensions of the SLM plate (current machines can achieve 500 mm) do not allow to make the component horizontally since the CCT is about one meter long. So, the only way to produce the former is to place it vertically because the bending problem is reduced, allowing better precision and the issue of dimensions is less critical. The current biggest available machines have an excursion of 700/800 mm and are special machines. In particular, the dimensions of the SLM machine available at CERN (Fig. 6.8) are 280 mm x 280 mm x 360 mm (Fig. 6.9). So, the only way to overcome the dimensions problem completely is to split the component into sectors that are welded later, but this would give the problems mentioned in step 7 in Section 6.1.

Figure 6.8: Additive manufacturing machine (SLM 280) at CERN (Courtesy of Romain Gerard).

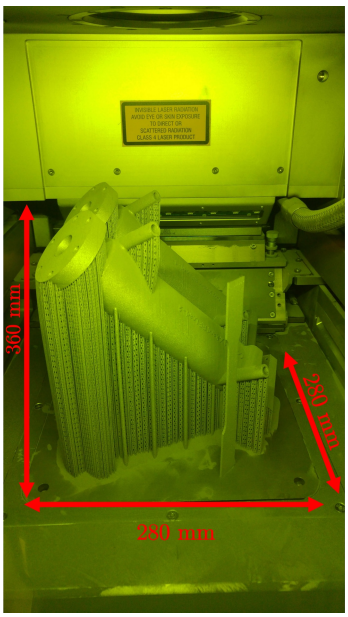

Figure 6.9: Inner area of SLM 280 (Courtesy of Romain Gerard).

Moreover, the tolerances on linear dimensions may range from ± 0.1 mm to ± 0.5 mm or even more if large deformations occur. The CCT requires tolerances of ± 50 μm at maximum. So,

tolerances of the additive manufacturing technology, at present, are far by a factor 2 to 10 from what is required for manufacturing the CCT magnets for beam lines and accelerators.
Furthermore, the best roughness is 5/20 μm which is insufficient to avoid the conductor's abrasion and higher than typical values achievable by traditional milling.
Moreover, raw material cost is a relevant problem because the cost per unit volume is 10/40 Swiss Francs (CHF) per cm^3. The total volume of the two straight mandrels is 17,598.71 cm^3. This indicates a minimum cost of 180kCHF, which is extremely large compared to machining, whose cost is foreseen around 15kCHF.
AM manufacturing is not applicable also in the case of PEEK GF 30 and NEMA G11 since glass fibres cannot be inserted in plastic materials at the moment, but glass fibres are essential to reduce the thermal contraction and have good mechanical properties. AM allows to use filler material in small powder instead of glass fibres to improve mechanical and radiation resistance. Despite this, the material's mechanical properties still remain lower than using glass fibres.

6.3. Assembly Process

This section explains the assembly process. The procedure uses simple tools: a marble, some pushing elements, some stoppers and does not need heavy presses or complex curved elements. This is big advantage with respect to the traditional Cos-Theta magnet design which requires large presses of about 600-800 tonnes per meter of magnet length. The main steps [25] of the process are the following ones:

1. Assembly starts on marble on a horizontal plane where the laminations (Fig. 6.10) of the single iron yoke halves are placed vertically. In this way, gravity helps to place iron laminations while some stoppers keep laminations in the correct position (Fig. 6.11).

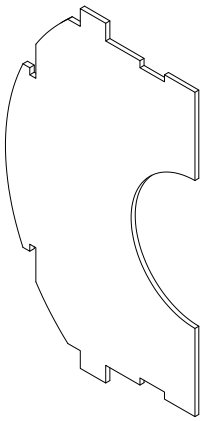

Figure 6.10: Single keystone lamination of one iron yoke half.

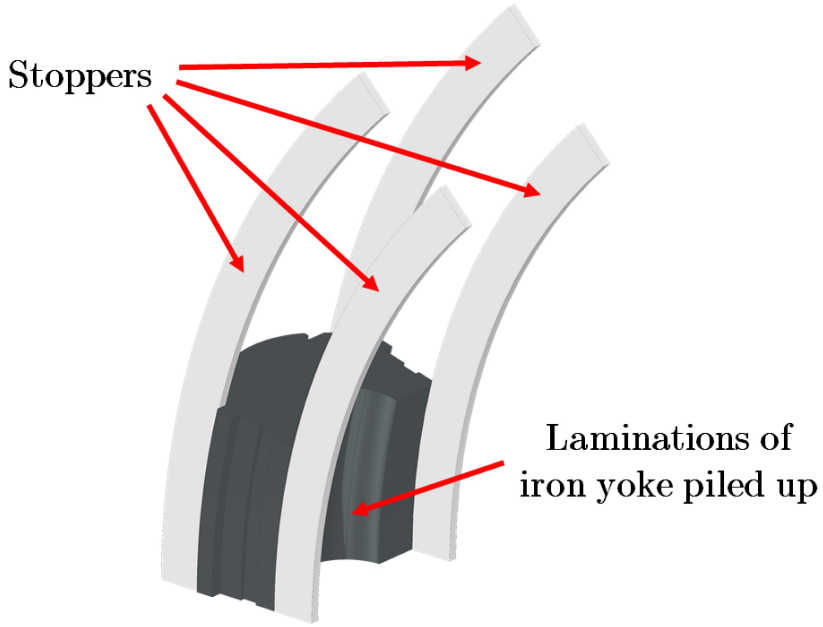

Figure 6.11: Single laminations of iron yoke piled up and stoppers, which keep laminations in the correct position.

2. Some keys are added and spot-welded to the laminations (Fig. 6.12). This passage is necessary to keep laminations attached to make a single iron yoke half when the stoppers are removed.

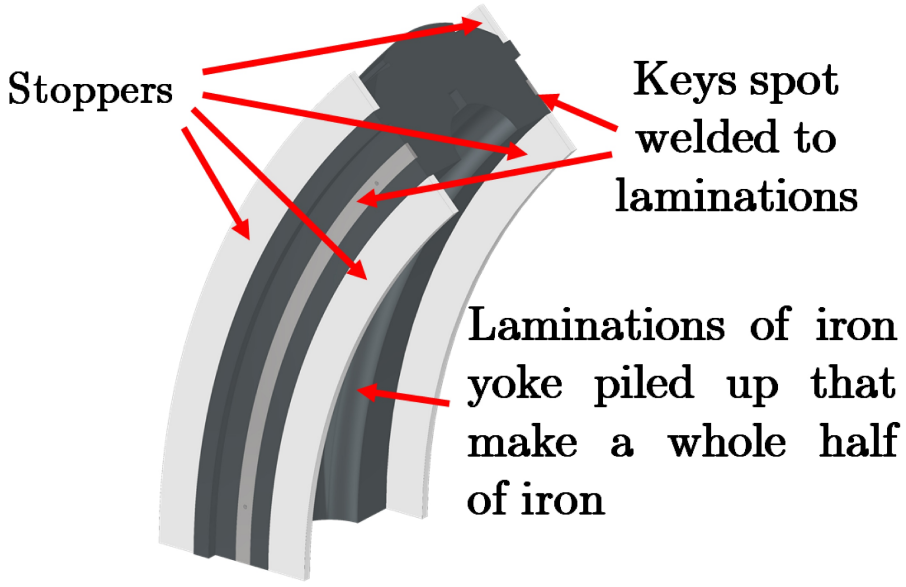

Figure 6.12: Addition of the keys.

3. After spot welding the keys with the laminations, stoppers are removed and the half of iron yoke is placed horizontally on the plane. Proper equipment to rotate the structure is required. Some tools (schematized in Fig. 6.13) will be used to clamp the half of iron yoke to the ground and leave access to the lower part of the structure to insert the clamps and other mechanical stoppers (Fig. 6.14).

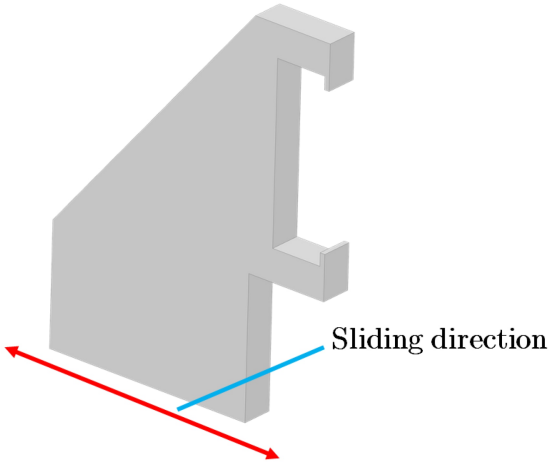

Figure 6.13: Scheme of the tool the clamps and sustains the iron yoke halves. The tool can slide on the horizontal plane, as indicated by the red arrow in the figure.

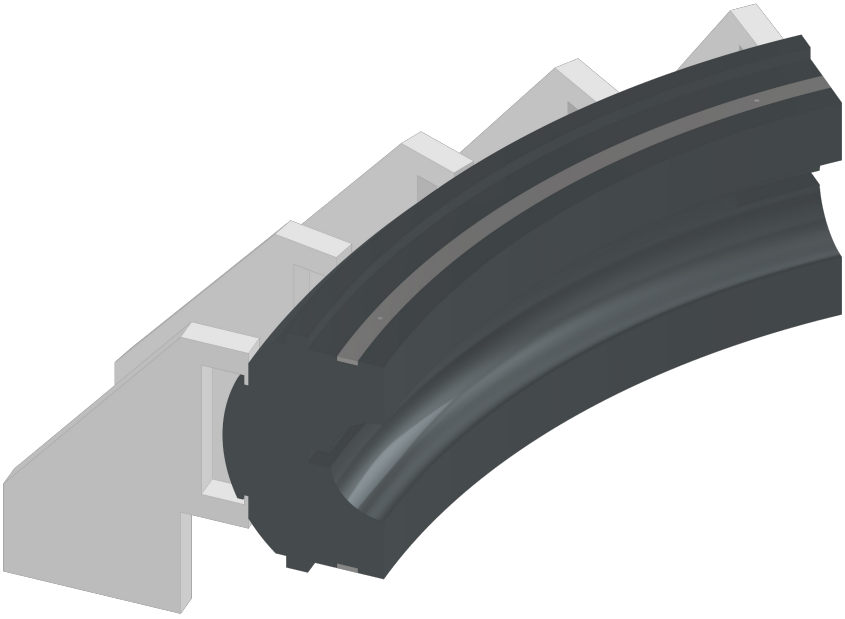

Figure 6.14: First iron yoke half placed horizontally and clamped to the ground by some tools.

4. Once the iron yoke half is clamped, the CCT is inserted and attached to iron yoke with temporary support on both extremities of the magnet (Fig. 6.15 and Fig. 6.16).

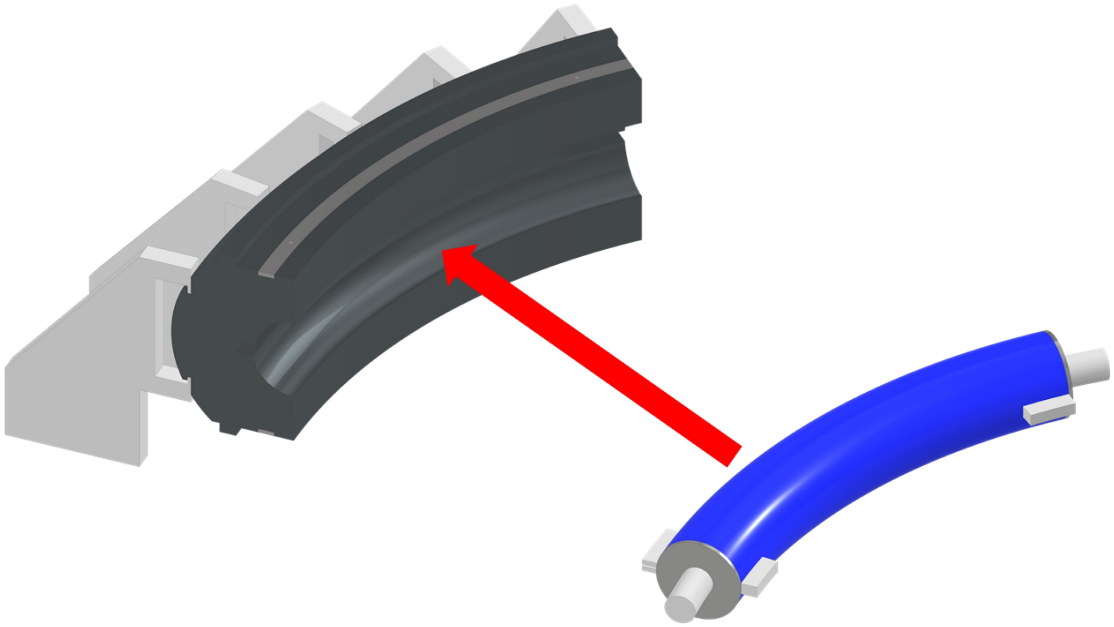

Figure 6.15: A curved bar is inserted in the aperture of the CCT to move the magnet inside the iron yoke.

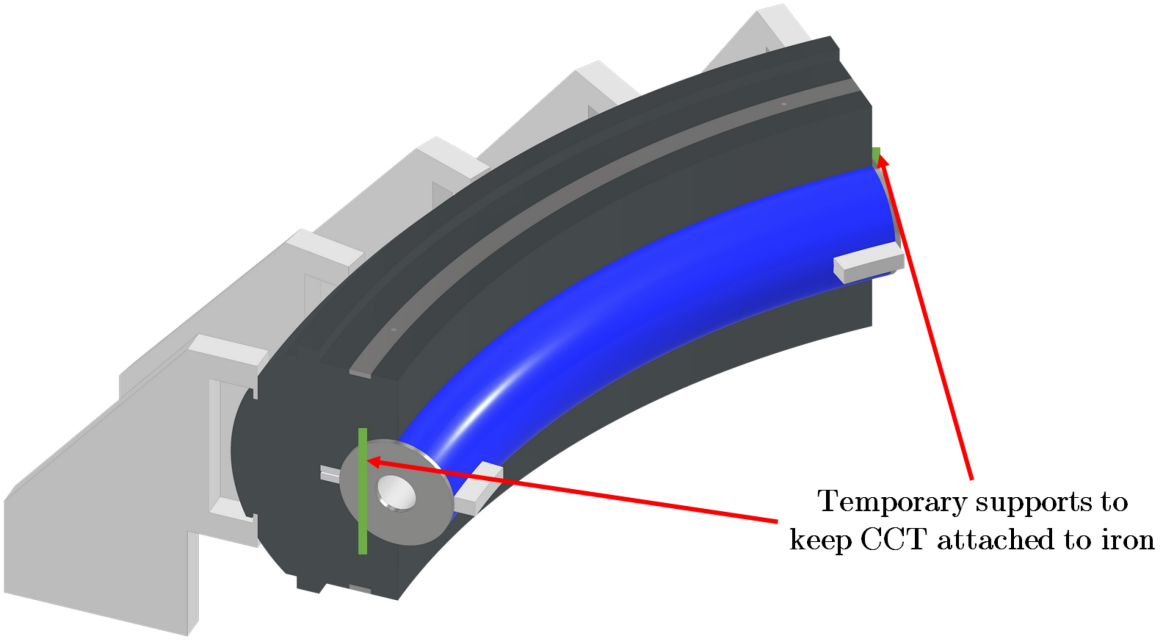

Figure 6.16: The curved bar in the aperture of the CCT is removed, and the magnet is kept attached to the iron yoke with two temporary supports (green area).

5. Two mechanical stoppers are fixed to the half of the iron yoke. These stoppers are needed to place the other half of the iron yoke in the correct position (Fig. 6.17). The mechanical stoppers must have high thermal contraction to not interfere with the rest of the structure during the operational phase.

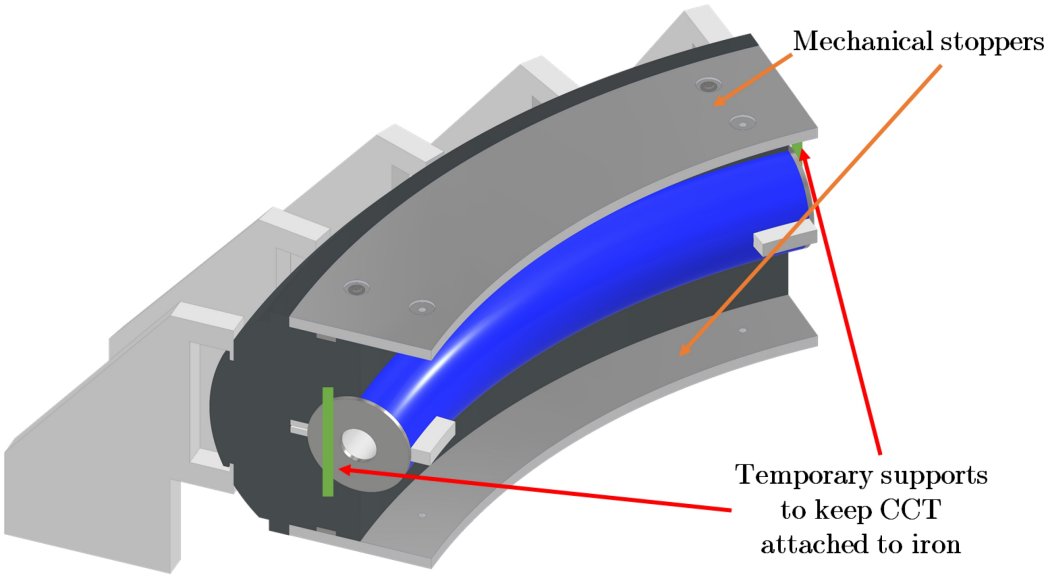

Figure 6.17: Addition of new mechanical stoppers to the mechanical structure.

6. Steps from 1 to 3 are repeated for the other half of the iron yoke which is pushed against the mechanical stoppers (Fig. 6.18 and Fig. 6.19). After this operation, the temporary supports which keep the CCT attached to the iron yoke are removed.

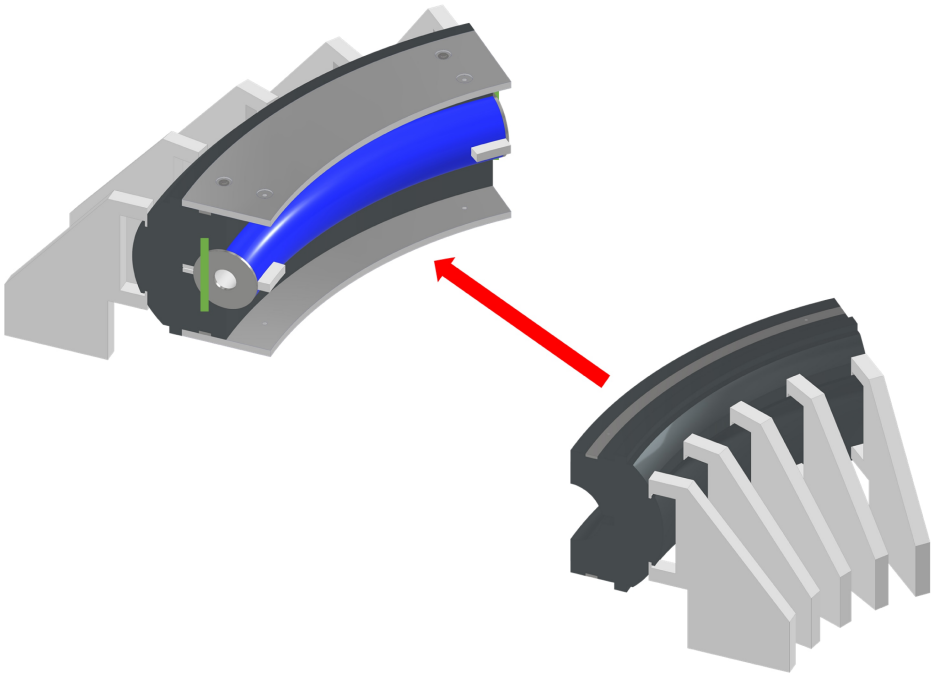

Figure 6.18: The two halves of iron yoke before being attached.

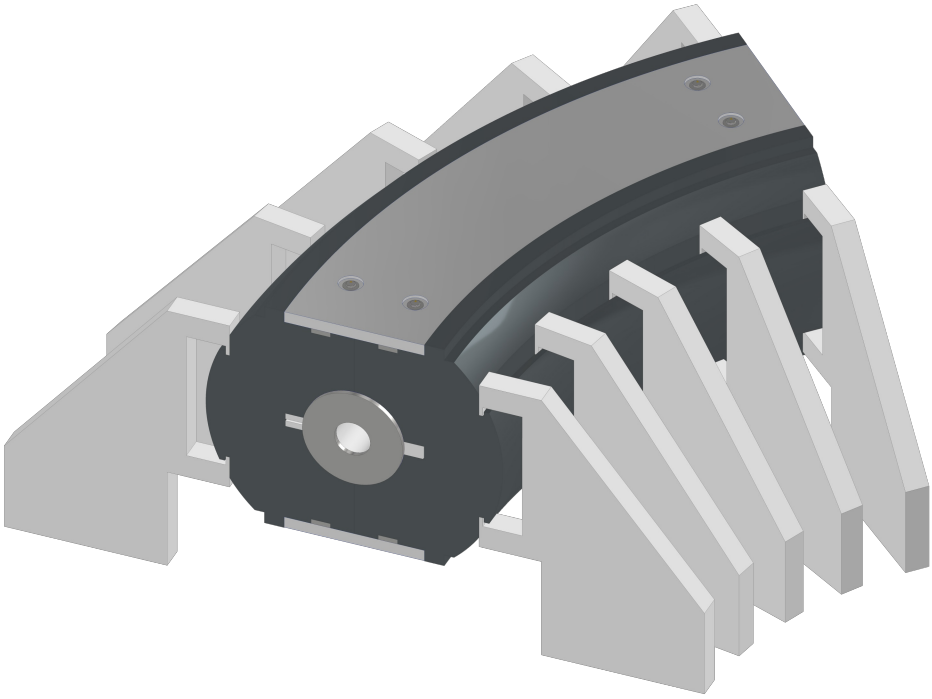

Figure 6.19: The tools that sustain the two halves of iron yoke slide horizontally and push one half towards the other until there is contact with the mechanical stoppers. After this procedure, the temporary supports of CCT are removed.

7. Then the aluminium clamps are heated and placed to shrink fit with iron yoke (Fig. 6.20).

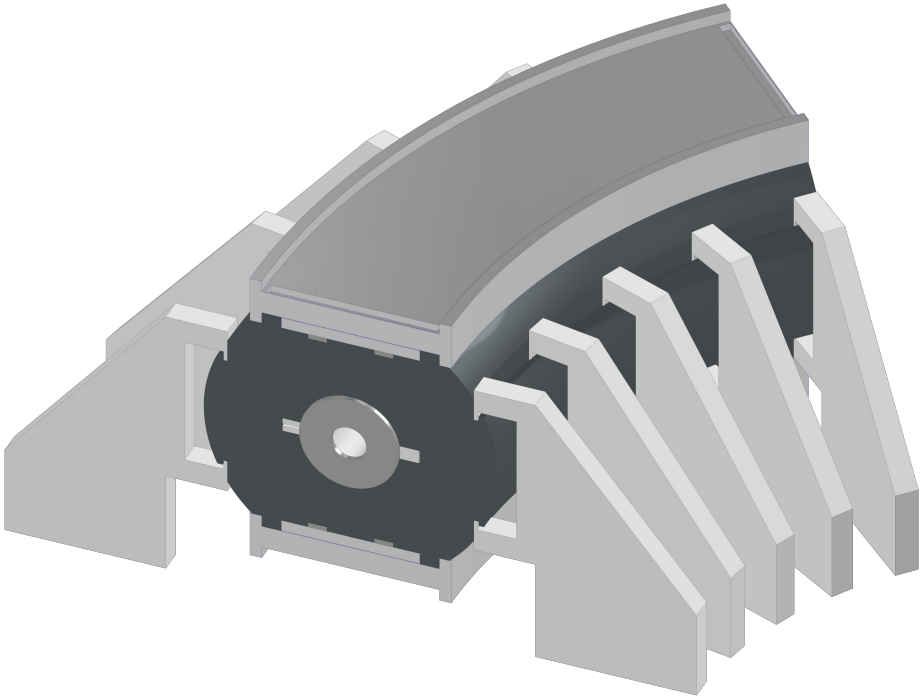

Figure 6.20: Addition of the two aluminium clamps.

8. When aluminium clamps cool down the end plates, 'c' shape joints and screws are added to obtain the final structure (Fig. 6.21).

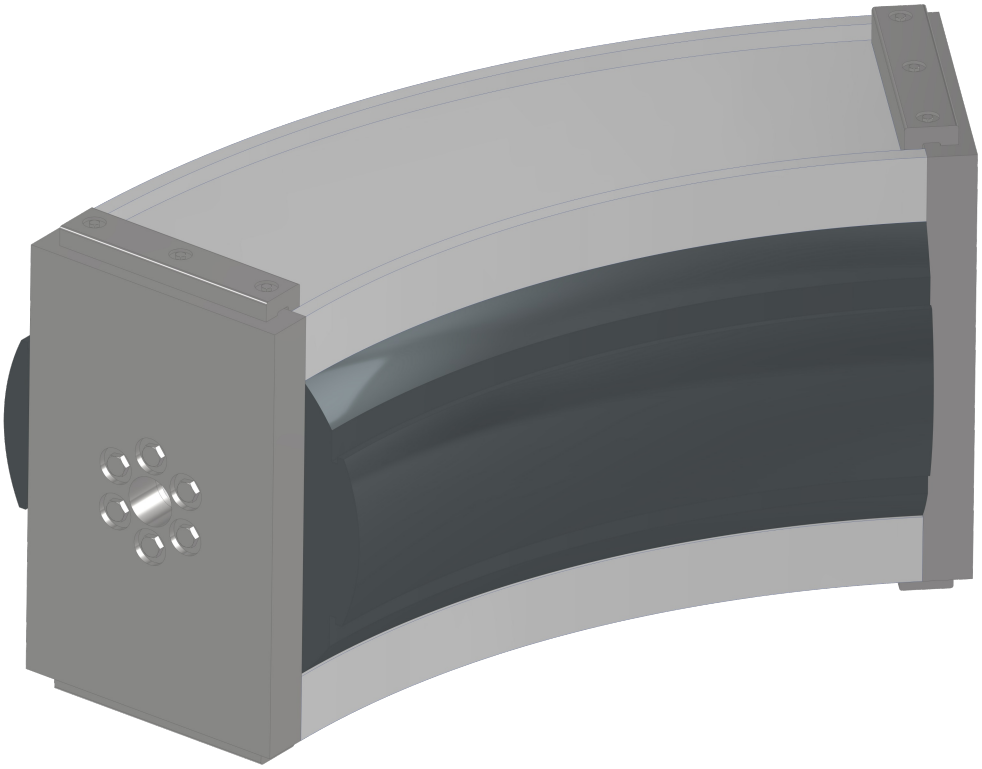

Figure 6.21: Final mechanical structure of CCT magnet.

6.4. Take Home Message

This chapter gave an overview of the processes and methods needed to manufacture and assemble the CCT magnets.

7 | Conclusions and Future Developments

The thesis performed a complete preliminary mechanical design of curved and straight CCT magnets. The results of this study are:

- The methods that permit generating the geometry required to obtain the desired magnetic field harmonics by CAD software. Specifically, the generated CAD model is fully parametric, able to update automatically and can represent many field harmonics combinations.
- An initial mechanical design was evaluated to have a first assessment of the behaviour of the CCT without iron yoke (the most severe case for mechanics). The FEM simulations showed stresses above the limit while displacements remained below the threshold of 0.1 mm.
- A new mechanical design was studied for curved and straight CCT to reduce stresses and keep displacements low. The design demonstrated to be effective in reducing displacements and keeping stresses well below the limit. The new desing was applied for the curved CCT (HITRI*plus*) and for the straight one with combined functions (IFAST).
- The methods needed to machine and assembly the magnets were described.

Now, with the basic design well established, the project will continue with the following tasks:

- Tests to evaluate the dimensions of the groove's cross-section which can be machined in the case of formers made of PEEK GF 30. The first test with PEEK without glass fibres has already been done (Fig. 7.1) and showed that ribs of 1 mm thickness could be machined also in case of deep grooves. The test will be repeated with PEEK GF 30 and then a first former of straight CCT 0.5 m long will be machined.

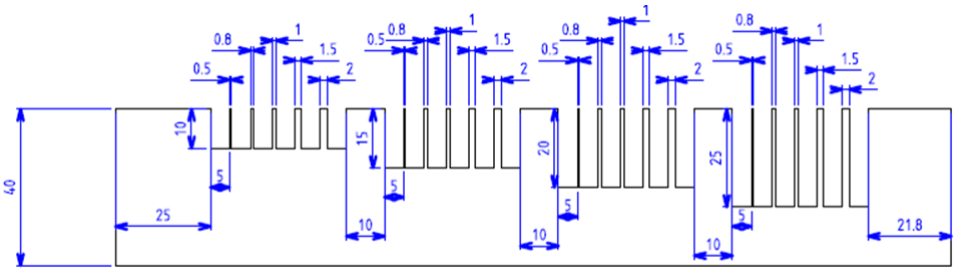

(a)

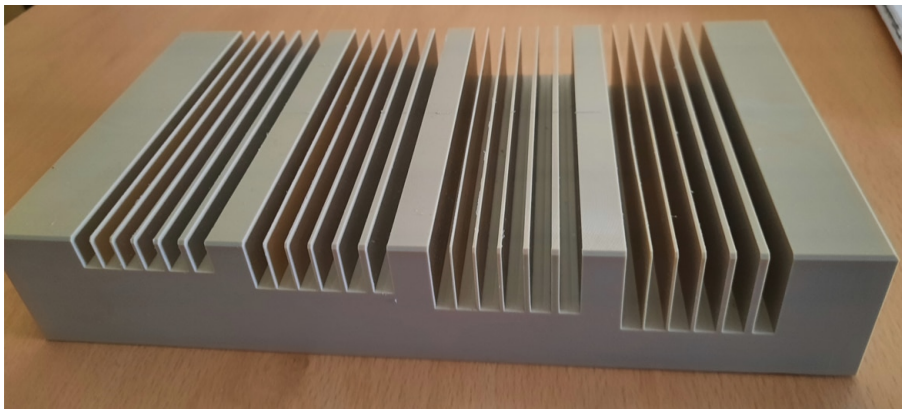

(b)

Figure 7.1: Sample of the first machining test with PEEK (Photo credits: Tosti s.r.l., Località Marinella 17/a - 58033 Casteldelpiano, Grosseto, Italy).

- Winding tests.
- Mechanical simulations of the curved CCT with the new parameters required by the HITRI*plus* collaboration. The main changes are the magnetic field of 4 T and bore diameter of 80 mm. Simulations will be more detailed considering no more a homogenised orthotropic material for the conductor, but the single ropes of the cable and the epoxy resin.
- Impregnation tests.
- Definition of the construction drawings for the final demonstrators.
- The assembly of the magnet demonstrators is foreseen for March 2024 for HITRI*plus*, June 2024 (Nb-Ti conductor) and October 2024 (HTS conductor) for IFAST.

This thesis work has been an important step in assessing the feasibility of the HITRI*plus* and IFAST innovative CCT magnets. The two collaborations believe that all the main design issues have been tackled. What remains is essentially finding and setting up suitable technologies for coupling the two curved tubes, one inside the other and for winding the conductor without complex winding machines.

Bibliography

[1] Private discussion with Romain Jerard (Forming and Welding Section in EN-MME at CERN) and Sébastien Clement (Polymer Laboratory at CERN). 2021.

[2] Private discussion with Jeroen van Nugteren. 2021.

[3] U. Amaldi and G. Kraft. Radiotherapy with beams of carbon ions. *Reports on progress in physics*, 68(8):1861, 2005.

[4] U. Amaldi, N. Alharbi, P. Riboni, M. Karppinen, D. Perini, G. Le Godec, D. Aguglia, D. Tommasini, E. Ravaioli, V. Ferrentino, et al. Sigrum-a superconducting ion gantry with riboni's unconventional mechanics. Technical report, 2021.

[5] ANSYS. Performing Submodeling in Ansys Mechanical. `https://www.youtube.com/watch?v=WC9bN2B9w2M`, 2020.

[6] F. Aymerich. *Travi a Forte Curvatura – Esercizi Svolti.* Resources for the course Meccanica dei Materiali at Università degli Studi di Cagliari, 2021.

[7] F. Aymerich. *Travi a Forte Curvatura - Integrali per Sezioni Tipiche.* Resources for the course Meccanica dei Materiali at Università degli Studi di Cagliari, 2021.

[8] F. Aymerich. *Sforzi di Flessione in Travi a Forte Curvatura.* Resources for the course Meccanica dei Materiali at Università degli Studi di Cagliari, 2021.

[9] L. N. Brouwer. *Canted-cosine-theta superconducting accelerator magnets for high energy physics and ion beam cancer therapy.* University of California, Berkeley, 2015.

[10] O. Capatina and C. Hauviller. High mechanical strength/low thermal conduction cryogenic materials. *EDMS CERN Portal. Document ID 357783 v.2*, 2002.

[11] CERN. CERN against COVID-19. `https://www.youtube.com/watch?v=L11ty-yQ05Y`, 2020.

[12] CERN. CERN CDS Video. `https://videos.cern.ch/`, 2022.

[13] CERN. CERN Document Server. `http://cdsweb.cern.ch/`, 2022.

[14] CERN. CERN Knowledge Transfer. `https://kt.cern/`, 2022.

[15] CERN. CERN Website. `https://home.cern/`, 2022.

[16] X. Chu, Z. Wu, R. Huang, Y. Zhou, and L. Li. Mechanical and thermal expansion properties of glass fibers reinforced peek composites at cryogenic temperatures. *Cryogenics*, 50(2):84–88, 2010.

[17] G. de Rijk. arxiv: Warm magnets. Technical report, 2021.

[18] A. Degiovanni and U. Amaldi. History of hadron therapy accelerators. *Physica medica*, 31 (4):322–332, 2015.

[19] E. Felcini. Analysis of a novel toroidal configuration for hadron therapy gantries. Technical report, EPFL, 2021.

[20] C. L. Goodzeit. Superconducting accelerator magnets. *USPAS, January*, 2001.

[21] J. Guardia Valenzuela. *Development and Characterization of a Novel Graphite-matrix Composite Material for Thermal Management Applications*. PhD thesis, Zaragoza U., 2015.

[22] C. Kokkinos. Material properties used in FE models. *EDMS CERN Portal. Document ID 2002489 v.1.*

[23] D. Meyer and R. Flasck. A new configuration for a dipole magnet for use in high energy physics applications. *Nuclear Instruments and Methods*, 80(2):339–341, 1970.

[24] R. Ortwein, J. Blocki, P. Wachal, G. Kirby, and J. van Nugteren. Fem modeling of multilayer canted cosine theta (cct) magnets with orthotropic material properties. *Cryogenics*, 107: 103041, 2020.

[25] D. Perini. New Technologies for the Construction of Curved CCTs. `https://indico.cern.ch/event/1112909/contributions/4677670/attachments/2370612/4049072/Hitri-7.pdf`, 2022.

[26] L. Rossi. State-of-the-art superconducting accelerator magnets. *IEEE transactions on applied superconductivity*, 12(1):219–227, 2002.

[27] L. Rossi and L. Bottura. Superconducting magnets for particle accelerators. *Reviews of accelerator science and technology*, 5:51–89, 2012.

[28] L. Rossi, A. Ballarino, D. Barna, E. Benedetto, C. Calzolaio, G. Ceruti, E. De Matteis, A. Echeandia, T. Ekelof, S. Farinon, E. Felcini, M. Gehring, G. Kirby, T. Lecrevisse, J. Lucas, S. Mariotto, J. Munilla, R. Musenich, A. Pampaloni, K. Pepitone, D. Perini, D. Popovic, M. Prioli, M. Pullia, L. Quettier, S. Sanfilippo, C. Senatore, E. Shabagin, M. Sorbi, M. Statera, D. Tommasini, F. Toral, R. Valente, D. Veres, and M. Vieweg. A european collaboration to investigate superconducting magnets for next generation heavy ion therapy. *IEEE Transactions on Applied Superconductivity*, 32(4):1–7, 2022. doi: 10.1109/TASC.2022.3147433.

[29] L. Rossi, E. Benedetto, E. De Matteis, S. Farinon, E. Felcini, M. Karppinen, S. Mariotto, R. Musenich, D. Perini, M. Prioli, et al. Preliminary study of 4 T superconducting dipoles for a light rotating gantry for ion-therapy. *IEEE Transactions on Applied Superconductivity*, 2022.

[30] K. Sciborn. Manufacturing concept: Curved CCT magnet. *CERN internal document*, 2021.

[31] K. Sciborn and A. Saillet. Bulk curved CCT magnet. *CERN internal document*, 2021.

[32] A. M. Sessler. Introduction to ion beam cancer therapy. *Lawrence Berkeley National Laboratory, Berkeley, CA*, 2010.

[33] Solvay. KetaSpire® PEEK Design and Processing Guide.

[34] E. Todesco. Masterclass - Design of Superconducting Magnets for Particle Accelerators, Unit 3. 2020.

[35] M. N. Wilson. Superconducting magnets. 1983.

[36] R. R. Wilson. Radiological use of fast protons. *Radiology*, 47(5):487–491, 1946.

A | Magnetic Field Harmonics

Fig. A.1 shows the classical reference system used for superconducting magnets. The z-axis direction defines the trajectory of the particle while the x-axis and y-axis directions define the magnet's cross-section plane:

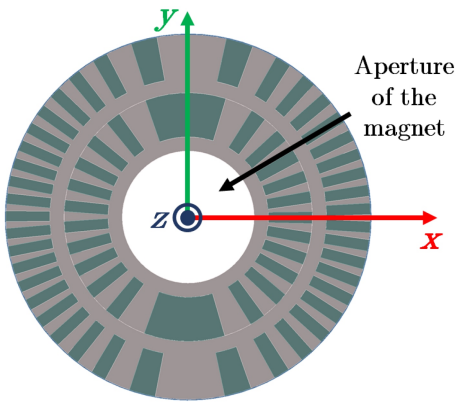

Figure A.1: Reference system for superconducting magnets in case of CCT. The XZ plane is the magnet's midplane.

Inside the aperture of the magnet, where the particle beam travels, there is no charge and magnetized material, so the Maxwell equations for the magnetic field [34] are:

$$\nabla \cdot \vec{B} = \frac{\partial B_x}{\partial x} + \frac{\partial B_y}{\partial y} + \frac{\partial B_z}{\partial z} = 0 \tag{A.1}$$

$$\nabla \times \vec{B} = \left(\frac{\partial B_y}{\partial z} - \frac{\partial B_z}{\partial y}, \frac{\partial B_z}{\partial x} - \frac{\partial B_x}{\partial z}, \frac{\partial B_x}{\partial y} - \frac{\partial B_y}{\partial x} \right) = 0 \tag{A.2}$$

If the field is constant along the longitudinal direction ($\frac{\partial B_z}{\partial z} = 0$), then Eq. A.1 and Eq. A.2 correspond to:

$$\frac{\partial B_x}{\partial x} + \frac{\partial B_y}{\partial y} = 0 \tag{A.3}$$

$$\frac{\partial B_x}{\partial y} - \frac{\partial B_y}{\partial x} = 0 \tag{A.4}$$

Eq. A.3 and Eq. A.4 are the necessary and sufficient conditions (Cauchy-Riemann conditions) for the complex function $B_y + iB_x$to be analytic. A complex function of complex variables is

analytic if it coincides with its power series, so $B_y + iB_x$ can be written as:

$$B_y(x,y) + iB_x(x,y) = \sum_{n=1}^{\infty} C_n (x+iy)^{n-1}, \ (x,y) \in D \tag{A.5}$$

$$B_y(x,y) + iB_x(x,y) = C_1 + C_2(x+iy) + C_3(x+iy)^2 + \ldots, \ (x,y) \in D \tag{A.6}$$

Where C_n are complex coefficients and D is the region of the aperture of the magnet.
Each term represents a pure magnetic field harmonic (Fig. A.2 and Fig. A.3): C_1 represents a dipolar field ($n = 1$), $C_2(x+iy)$ represents quadrupolar field ($n = 2$), $C_3(x+iy)^2$ is a sextupolar field ($n = 3$) and so on. The magnetic field produced in particle accelerator magnets is generally optimized to make a single harmonic, but also combined function magnets (which contain more harmonics) are used to modify the beam along the trajectory and optimize the accelerator layout. For example, the CCT straight magnet, developed during this thesis, contains a dominant dipolar harmonic to bend the particle beam and a smaller quadrupolar harmonic to focus it. In addition to the main harmonic, all the other harmonic coefficients, with decreasing amplitude with their order, are present due to the mechanical tolerances of the coils layout.

Figure A.2: Dipolar (left), quadrupolar (center) and sextupolar (right) superconducting magnets (Courtesy of Lucio Rossi).

Eq. A.5 can be rewritten as:

$$B_y(x,y) + iB_x(x,y) = \sum_{n=1}^{\infty} (B_n + iA_n)(x+iy)^{n-1}, \ (x,y) \in D \tag{A.7}$$

Where B_n and A_n are called normal and skew components respectively (Fig. A.3). A pure magnetic field (composed of one single harmonic) has just one non zero coefficient (B_n or A_n) called the main order of the field [27].

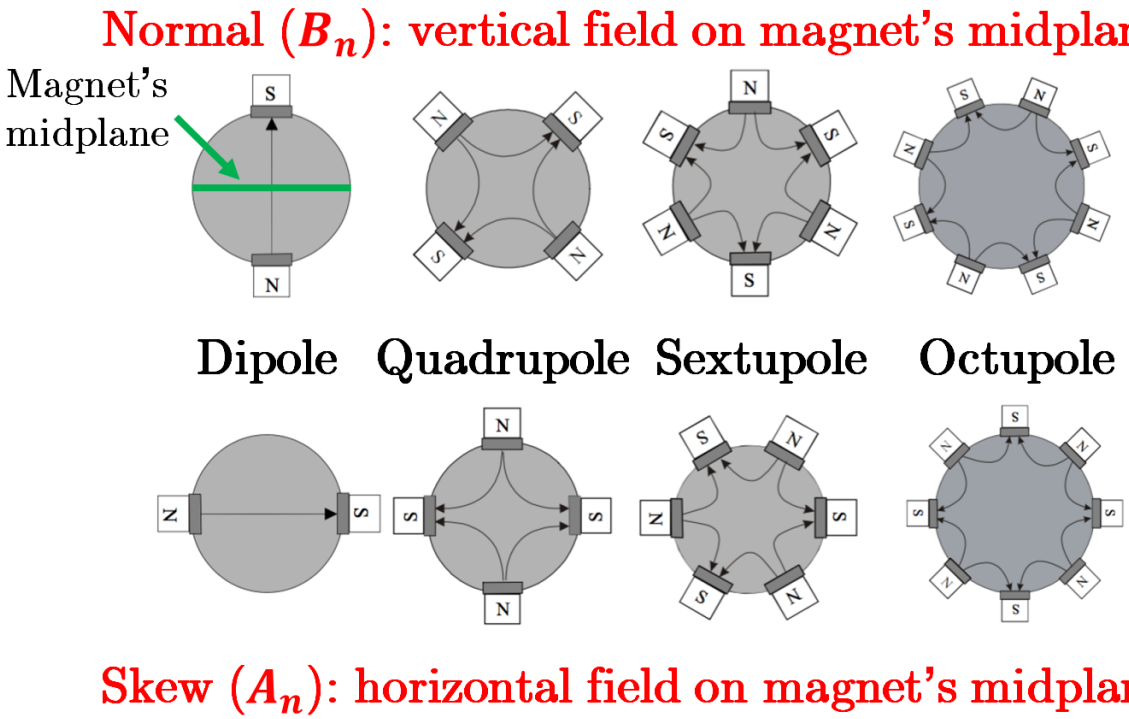

Figure A.3: Magnetic field harmonics generated by normal and skew components. It is possible to see that the harmonics generated by B_n and A_n (Eq. A.7) are the same, but one is rotated by $\pi/(2n)$ radians with respect to the other (Fig. adapted from [17]).

In Eq. A.7 it is possible to factorize the main component (e.g. B_1 for dipoles, B_2 for quadrupoles) and 10^{-4} to obtain Eq. A.8. R_{ref} is the reference radius (usually equal to 2/3 of the aperture radius) introduced to have dimensionless coefficients.

$$B_y(x,y) + iB_x(x,y) = 10^{-4} B_{main} \sum_{n=1}^{\infty} (b_n + ia_n) \left(\frac{x+iy}{R_{ref}} \right)^{n-1}, \ (x,y) \in D \tag{A.8}$$

The ideal geometrical shape of the magnet changes due to mechanical tolerances and deformations caused by the applied loads. This causes the coefficients B_n and A_n, which appear in Eq. A.7, to be different from the ideal ones. This difference (field quality) is required to be about 0.01% in superconducting magnets for particle physics, and the term 10^{-4} is factorized in Eq. A.8 to measure field quality in 'units' ($b_n = B_n/(B_{main}10^{-4})$ and $a_n = A_n/(B_{main}10^{-4})$). So, the constraints on the required field can be translated into constraints on the position of the current lines in the magnet's cross-section.

B | CERN Knowledge Transfer

The design of LHC and CERN's facilities presents scientists with many challenges at the forefront of technology. For this reason engineers, technicians and physicists develop new technologies and knowledge that can also be applied to fields different from physics research and shared with society. The CERN's convention states [13]: "The Organization shall have no concern with work for military requirements and the results of its experimental and theoretical work shall be published or otherwise made generally available." Moreover, the mission of CERN is [15]:

- Provide a unique range of particle accelerator facilities that enable research at the forefront of human knowledge.
- Perform world-class research in fundamental physics.
- Unite people from all over the world to push the frontiers of science and technology, for the benefit of all.

HITRI*plus* and IFAST are just two examples of knowledge shared with society. The research done at CERN can be applied to many different fields: medical technologies, aerospace, safety, environment, industry 4.0, cultural heritage, safety and emerging technologies [14]. It is important to notice that this knowledge transfer has significantly impacted people's lives over the years, therefore some significant examples of this are described concisely:

- The accelerator complex built at CNAO (National Centre for Oncological Hadron Therapy in Pavia, Italy) is based on the Proton Ion Medical Machine Study (PIMMS), a design study done at CERN from 1995 to 2000. CERN took part in the CNAO accelerator complex project and construction, especially with magnets, radiofrequency cavity, dipole measurements and beam diagnostics [15].
- The MACHINA collaboration between CERN and INFN aims at helping to recognize false artworks. The project's goal is to build a 'miniaturized' particle accelerator that will decrease the cost of the PIXE elemental analysis. PIXE is the current technique used to evaluate artworks' authenticity, but it requires large and expensive facilities. The MACHINA device will be much smaller, allowing it to be used by museums that cannot access larger facilities. Moreover, the small size permits transporting the device to fixed artworks or those too delicate to be moved [14].
- The pressure regulation done in the lab routinely for CERN experiments is very similar to what is necessary to build and control the elements of a ventilator. So, a group of institutes from the LHCb (one of CERN's experiments) collaboration designed High Energy Ventilator (HEV) in response to Covid-19 pandemic [11] (Fig. B.1). The design was

guided by local hospitals, an international team medical experts, and specialists such as the World Health Organisation. The goal was to design and prototype a versatile, high quality, low-cost medical ventilator that aims to provide long-term alveolar ventilation support to patients, in or out of intensive care, for intubated and non-invasive cases [14]. Moreover, the design priorities safety, patient comfort and performance are comparable to other commercial devices which are typically expensive to purchase, preserve and need huge training to be used. Many commercial devices also depend on the supply of high-flow oxygen and medically pure compressed air, which are not easily available in several countries in the world [12].

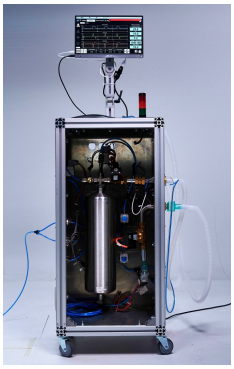

Figure B.1: The High Energy Ventilator (Photo credits: CERN)

In 2020, funding was made available for the redesign of HEV for use in low- and middle-income countries. The redesign is based on the HEV prototype and is called High Performance Low Cost Ventilator (HPLV). HPLV depends less on compressed gases and mains electricity supply. So, it is more adequate for a wide range of challenging situations in regions where ideal conditions may not be available. The mechanical design of both the HPLV and HEV can give a robust ventilator quick and simple to build with low cost and easily available components. Functionality is aimed at treating most COVID-19 cases to make very high-end machines available for the most intensive cases. Moreover, the pneumatic concept (i.e. ventilation provided via a low-pressure buffer) allows precise and safe pressure control and accurate supervision of flow rates. The described features make the HEV and HPLV proper for the treatment of COVID-19 cases and for general-purpose ventilators beyond COVID-19. Moreover, the ventilators may be useful also for developing new ideas about ventilation inside academic research.

- The first PET (Positron-Emission Tomography) picture was taken at CERN in 1977 (Fig. B.2). PET was not invented at CERN, but the work done by two CERN physicists (David Townsend and Alan Jeavons) made a key contribution to PET development, thanks to the type of detector and computer programme developed for image-taking analysis. Some years later, Townsend and other colleagues in the US suggested combining PET-CT (computed tomography) to see both metabolic and anatomic information. This was a key development for cancer diagnosis and treatment monitoring. After 44 years, PET technology is even more advanced thanks to work carried out at CERN and other research laboratories worldwide. Additionally, the CERN group of the Crystal-Clear Collaboration is developing new quick detector prototypes for both high-energy physics experiments and

medical imaging, with particular attention to PET technology [14].

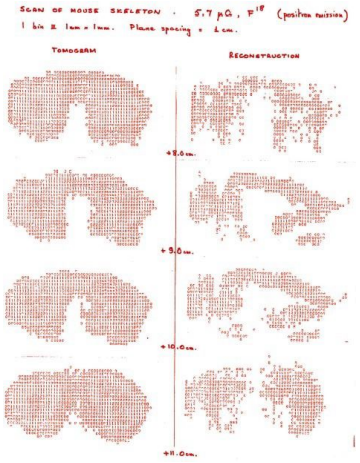

Figure B.2: The first PET picture showing the skeleton of a mouse. (Photo credits: CERN).

- The World Wide Web (WWW) was invented at CERN by Tim Berners-Lee in 1989. The purpose of WWW was to meet the demand for automated information-sharing among scientists in universities and institutes worldwide. CERN made the WWW software public on 30th April 1993 and made a successive release available with an open licence to maximize the diffusion of WWW, allowing the web to flourish [14].
- VESPER (Very energetic Electron facility for Space Planetary Exploration missions in harsh Radiative environments), which is part of CLEAR (CERN Linear Electron Accelerator for Research), is the only facility on Earth which can reproduce the most extreme phenomena of Jupiter's severe radiative environment. Jupiter has a very high magnetic field which can trap electrons of energies up to several hundred mega electron volts (MeV). The European Space Agency (ESA) came to VESPER in 2018 to prepare the JUICE (JUpiter ICy moons Explorer) spacecraft for its exploration mission around Jupiter's icy moons. ESA successfully tested the capacity of the JUICE critical electronic components to resist high energy electron fluxes for such long durations [14].
- CERN uses its technologies and creativity to fulfil another goal: a healthier and more sustainable planet. The CERN's role in this area varies from more energy efficient cooling systems to new biochemical sensors for water safety through innovative irrigation techniques for the most difficult agricultural environments [14].
- CERN also develops technologies for safety. CERN's environment combines different kinds of radiation, very low temperatures, extremely high magnetic fields and exceptionally high voltages. These characteristics require new solutions for detecting threats and preventing risks [14].

It is worth noticing that research done at CERN does not allow us just to explore our world at the infinitely small, which is extraordinary itself, but also permits improving people's lives sharing knowledge and favouring cooperation among people worldwide.

C | Analytical Estimation of Curved CCT Deflection

Analytical calculations were carried out to estimate the deflection due to the resultant of the Lorentz forces (in case of the presence of iron yoke) in the magnet extremities which tend to make the curved CCT straight (Fig. C.1).

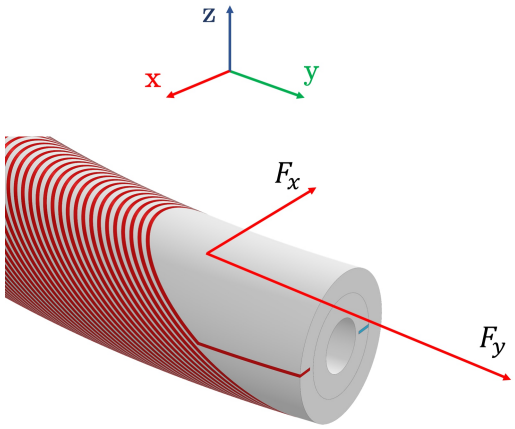

Figure C.1: Resultant of Lorentz forces ($F_x = -23,856$ N, $F_y = 1.3158e5$ N) on CCT extremity.

The CCT was modelled as a homogeneous circular beam with a circular hollow section made by the formers' material. Due to the symmetry of the forces, it is possible to study just half of the magnet imposing a fixed constraint in the middle of the CCT (Fig. C.2) [6].

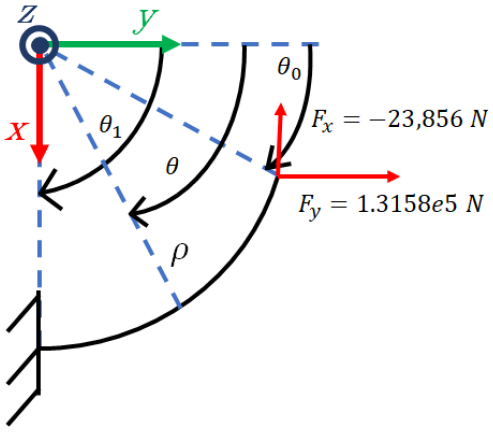

Figure C.2: Model for analytical calculations.

Where ρ is the bending radius, θ is the angular coordinate, $\theta_1 = \pi/2$, $\theta_0 = \pi/2 - \beta/2$ where β is the bending angle. The displacements along the x-axis and y-axis were calculated using the the Principle of Virtual Work (PVW) with the following sign convention for the bending moment (Fig. C.3):

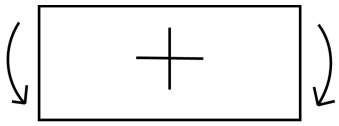

Figure C.3: Sign convention for the bending moment.

Applying the equations of equilibrium, the bending moment along the beam has the following expression:

$$M = F_x \rho \left(\cos\theta_0 - \cos\theta\right) + F_y \rho \left(\sin\theta - \sin\theta_0\right) \tag{C.1}$$

C.1. Calculations with the Principle of Virtual Work

Considering just the contribution of the bending moment, it is possible to apply the PVW and write the equality between the work of internal forces and the work of the external forces:

$$1 \cdot \delta = \int_0^L M' d\varphi = \int_0^L M' \frac{M}{EAy_g} d\theta \tag{C.2}$$

Where δ is the displacement of the real structure, 1 is the unitary load applied to the auxiliary structure, M' is the bending moment of the auxiliary structure, $d\varphi$ is the rotation of the real structure due to M, A is the area of the cross-section of the beam and $y_g = \rho_g - \rho_o$. ρ_g is the bending radius of the centroid of the cross-section (which corresponds to ρ) and ρ_0 is the bending radius of the neutral axis of the cross-section. In case of circular hollow cross-section ρ_0 is [7], [8]:

$$\rho_0 = \frac{A}{\int_A \frac{dA}{r}} = \frac{\frac{\pi}{4}\left(D^2 - d^2\right)}{2\pi\left(\sqrt{\rho^2 - \frac{d^2}{4}} - \sqrt{\rho^2 - \frac{D^2}{4}}\right)} \tag{C.3}$$

Where D and d are the external and internal diameters of the beam respectively. D corresponds to the outer diameter of the external former and d is the bore diameter of the inner former.

The auxiliary structure is equal to the real structure except for the loads. In the auxiliary structure, a unitary load is applied in the point where the displacement δ is calculated and along the direction of the displacement. So, the auxiliary structures to calculate δ_x and δ_y are (Fig. C.4):

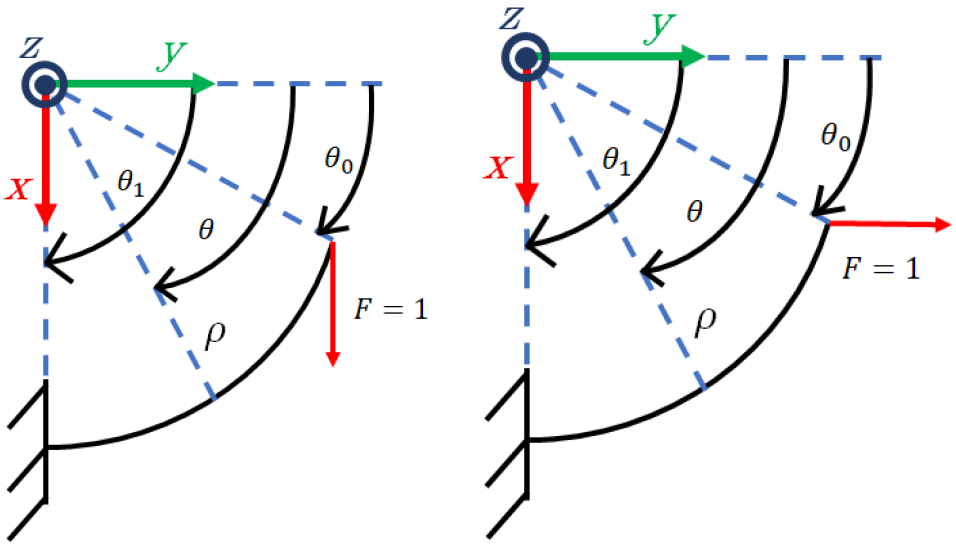

Figure C.4: Auxiliary structures for the calculation of δ_x (a) and δ_y (b).

The bending moments of the two auxiliary structures (Fig. C.4) are respectively:

$$M' = 1 \cdot \rho \left(\cos\theta_0 - \cos\theta\right) \tag{C.4}$$

$$M' = 1 \cdot \rho \left(\sin\theta - \sin\theta_0\right) \tag{C.5}$$

Combining all the previous equations it is possible to obtain:

$$\delta_x = \int_{\theta_0}^{\theta_1} \rho \left(\cos\theta_0 - \cos\theta\right) \frac{F_x \rho \left(\cos\theta_0 - \cos\theta\right) + F_y \rho \left(\sin\theta - \sin\theta_0\right)}{EA\left(\rho - \rho_0\right)} d\theta \tag{C.6}$$

$$\delta_y = \int_{\theta_0}^{\theta_1} \rho \left(\sin\theta - \sin\theta_0\right) \frac{F_x \rho \left(\cos\theta_0 - \cos\theta\right) + F_y \rho \left(\sin\theta - \sin\theta_0\right)}{EA\left(\rho - \rho_o\right)} d\theta \tag{C.7}$$

C.2. Results

FEM simulations of the homogenous circular hollow beam (made by the former's material) and real CCT (made by the former and the coil modelled as a homogenized orthotropic material) were carried out to evaluate the precision of the analytical calculations (Fig. C.5):

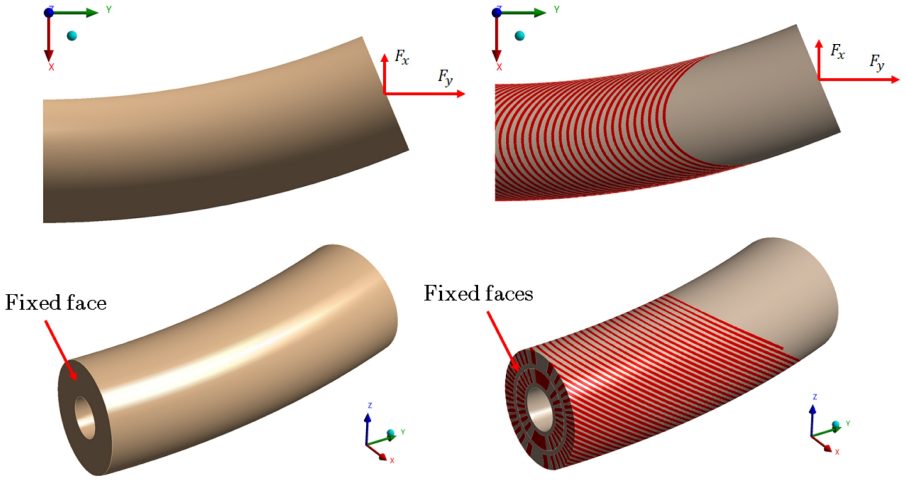

Figure C.5: FEM models of the hollow beam (which used beam elements) and the real CCT.

The results of the analytical calculations and the FEM models for the different formers' materials are reported in the following tables (Table C.1, Table C.2, Table C.3, Table C.4, Table C.5 and Table C.6):

PEEK GF 30	δ_x **[mm]**	δ_y **[mm]**
PVW	0.36	0.10
FEM Beam	0.34	0.25
FEM CCT	0.26	0.21
(FEM Beam – PVW) / FEM Beam	-6.96	60.88
(FEM CCT – PVW) / FEM CCT	-39.09	53.30

Table C.1: Results in case of formers made of PEEK GF 30.

NEMA G11	δ_x **[mm]**	δ_y **[mm]**
PVW	0.30	0.08
FEM Beam	0.28	0.21
FEM CCT	0.23	0.19
(FEM Beam – PVW) / FEM Beam	-6.84	60.82
(FEM CCT – PVW) / FEM CCT	-25.66	56.78

Table C.2: Results in case of formers made of NEMA G11.

Aluminium 6082-T6	δ_x **[mm]**	δ_y **[mm]**
PVW	0.08	0.02
FEM Beam	0.08	0.06
FEM CCT	0.13	0.09
(FEM Beam – PVW) / FEM Beam	-5.91	60.99
(FEM CCT – PVW) / FEM CCT	36.33	74.47

Table C.3: Results in case of formers made of aluminium 6082-T6.

Aluminium Bronze 954	δ_x **[mm]**	δ_y **[mm]**
PVW	0.06	0.02
FEM Beam	0.05	0.04
FEM CCT	0.11	0.07
(FEM Beam – PVW) / FEM Beam	-5.88	60.87
(FEM CCT – PVW) / FEM CCT	47.07	77.94

Table C.4: Results in case of formers made of aluminium bronze 954.

Titanium Alloy	δ_x **[mm]**	δ_y **[mm]**
PVW	0.05	0.01
FEM Beam	0.05	0.04
FEM CCT	0.10	0.07
(FEM Beam – PVW) / FEM Beam	-5.92	61.07
(FEM CCT – PVW) / FEM CCT	49.05	78.74

Table C.5: Results in case of formers made of titanium alloy.

AISI 316L	δ_x **[mm]**	δ_y **[mm]**
PVW	0.03	0.01
FEM Beam	0.03	0.02
FEM CCT	0.07	0.05
(FEM Beam – PVW) / FEM Beam	-5.72	60.87
(FEM CCT – PVW) / FEM CCT	59.03	82.15

Table C.6: Results in case of formers made of AISI 316L.

For all the materials, differences between the analytical model results and the beam's FEM model remain within few percents for δ_x. Instead, the difference is about 60% for δ_y. The y-axis is close to the axial direction of the beam. So, probably, this huge difference is due to the absence of the axial load in the analytical model.

Instead, the minimum difference between the analytical model and the FEM of the CCT is around 40% for δ_x and 50% for δ_y. This huge difference is due to the presence of the coil in the FEM model of the CCT, which is a homogenised orthotropic material. The difference between the analytical and FEM models increases with the stiffness of the formers' material: increasing the stiffness of the formers, the difference of Young's modulus between the formers and the coil increases too. So, the higher the stiffness of the formers, the more CCT is different from a homogeneous and isotropic material as in the analytical model.

List of Figures

List of Tables

List of Symbols

Variable	Description	SI unit
$\boldsymbol{u}_\rho$	radial displacement	mm
$\boldsymbol{u}_\theta$	azimuthal displacement	mm
$\boldsymbol{w}$	axial pitch for straight CCT	mm
$\boldsymbol{\phi}_0$	angular pitch for curved CCT	rad